Geophysical Characterization of the Elk Creek Carbonatite Based on 3D Joint Inversion and Geology Differentiation

by

Kenneth Han Li

A thesis submitted to the Department of Earth and Atmospheric Sciences,
College of Natural Science and Mathematics
in partial fulfillment of the requirements for the degree of

MASTER OF SCIENCE
in Geophysics

Chair of Committee: Jiajia Sun
Committee Member: Mason Andrew Kass
Committee Member: William Sager

University of Houston
May 2021

Dedication

This study is dedicated to my family and friends who kept me sane in the midst of a global pandemic.

Acknowledgements

I am extremely grateful to my advisor, Dr. Jiajia Sun, for being an excellent mentor and his enthusiasm for research. This thesis would not have been possible without his guidance. I would also like to thank my committee members, Dr. M. Andy Kass and Dr. William Sager, for their patience and support. I am indebted to all of my fellow research group members under Dr. Sun, but I wanted to specifically thank Xiaolong Wei and Jae Deok Kim for their help with the extensive amount of coding that was required in this thesis. I would like to thank Scott Honan, President of Elk Creek Resources Corp. for his permission to use survey data from the Elk Creek region and Anne McCafferty of the USGS for providing the data. I would also like to thank Benjamin Drenth of the USGS as his prior work analyzing the Elk Creek Carbonatite was instrumental to this study. This work would not have been possible without the python packages developed by the SimPEG and PyVista teams which were used extensively in this study.

Abstract

The Elk Creek Carbonatite located in southeastern Nebraska hosts the largest known niobium deposit in the United States. Most of the known niobium is hosted within magnetite-dolomite carbonatite, a dense and highly magnetized unit within the carbonatite. The shallower lithology of the carbonatite has been well explored by boreholes, but the deeper lithology remains poorly understood. Three-dimensional joint inversion of airborne gravity gradiometry and magnetic measurements was performed, producing a structurally coupled density and susceptibility model. Geology differentiation, a process of classifying the recovered subsurface models into distinct units, was then carried out to develop a 3D quasi-geology model. Physical property measurements based on drill core samples and analysis of inverted physical property values in the spatial domain were used for geology differentiation. The resulting quasi-geology model, an approximation of the subsurface geology, shows the spatial distribution of various geological units in 3D, and includes units at greater depths than previous studies on the region. I identified 11 geological units with each characterized by a distinct combination of density and susceptibility values. These units include the country rock surrounding Elk Creek, various carbonatites, mafic rocks, the niobium target zone, and additional distinct geological units which have not been previously classified. Geology differentiation also identifies the known niobium ore zone and indicates the existence of a significant volume of dense and strongly magnetized rocks below the deepest boreholes. These rocks are likely to be associated with unexplored niobium mineralization. This thesis work is the first attempt at constructing a 3D quasi-geology model in the study area based on airborne geophysical measurements, and demonstrates the added value of 3D geophysical inversions and geology differentiation when it comes to mineral exploration under thick sedimentary overburden.

Table of Contents

List of Tables

List of Figures

Introduction

In December 2017, the President of the United States issued Executive Order 13817: A Federal Strategy to Ensure Secure and Reliable Supplies of Critical Minerals. This Executive Order called for the federal government to identify imported minerals essential to the country's economic and military security, and to form a strategy to reduce the risk of supply disruption. These critical minerals must also serve an essential function in the manufacturing of important economic or security products. As a result, the Department of the Interior in 2018 finalized a list of 35 critical minerals, including niobium (83 FR 23295, 2018).

The subsurface Elk Creek carbonatite complex (ECCC) is an elliptical magmatic body that was formed around 0.550 Ga in the early Paleozoic (Xu, 1996). It is the only niobium deposit in the United States planned for resource extraction and also contains significant levels of rare earth element (REE) mineralization (USGS, 2020). Niobium is a vital resource for modern development as 75% of globally produced niobium is used to manufacture steel alloys with improved corrosion resistance, strength, and other beneficial properties (Papp, 2013). Additionally, niobium alloys are also used to manufacture superconducting magnets used in magnetic resonance imaging (MRI) as well as in particle accelerators such as the Large Hadron Collider in Europe (Schulz et al., 2017). The United States has not produced niobium after 1959 as most domestic sources are not commercially recoverable due to poor grade or mineralogical complexity (USGS, 2020). This has led to a great interest in determining the quantity of niobium within the ECCC.

Niobium mineralization at Elk Creek is contained within pyrochlore with most mineralization occurring within magnetite-dolomite dolomite (Blessington, 2014). The magnetite-dolomite carbonatite composes a relatively minor component of the ECCC, but contains the majority of the niobium mineralization (Drenth, 2014; Blessington, 2014). A target zone was identified by Molycorp in 1978 upon intercepting magnetite-dolomite carbonatite during exploratory drilling (Blessington, 2014; SRK Consulting, 2015). After this discovery, additional exploratory drilling along with airborne geophysical surveys were conducted over the region, with the most recent geophysics survey data collected in 2011 by Fugro Airborne for NioCorp Developments, Ltd (SRK Consulting, 2015). Mineral resource estimation studies by consulting firms such as SRK Consulting (2015) have also mapped the known niobium ore zone based on borehole data. However, while exploratory drilling has been able to classify many of the shallow lithologic units at Elk Creek, much of the complex remains unexplored as the deepest boreholes currently extend only about 1000 m in depth (SRK Consulting, 2015).

Previously, data from a 2011 airborne geophysical survey and measurements from core samples were combined to create a quantitative interpretation of the Elk Creek lithology (Drenth, 2014). This included 2.5D profile forward modeling along two cross-sections of the ECCC, with results indicating the presence of additional magnetite-dolomite carbonatite at depths deeper than the deepest boreholes (Drenth, 2014). The same data were used in Kass et al. (2015) to produce the first 3D inversion results of the airborne datasets. These initial investigations into lithologic differentiation of the ECCC created a crossplot comparing the inverted physical properties of magnetic susceptibility and density which showed distinct clusters of lithologies (Kass et al., 2015).

In this thesis research, I use the same airborne geophysics data as in Drenth (2014) and Kass et al. (2015). The goal of my research was to characterize the lithology at Elk Creek through geology differentiation and to identify possible sources of niobium within the carbonatite. I accomplished this goal through the creation of a 3D quasi-geology model of the Elk Creek region with differentiated lithologic units. The creation of this model first started with the analysis of airborne gravity gradiometry and magnetic data which were inverted using both separate and joint inversion which produced 3D physical property models of the carbonatite and the surrounding geology. Geological observations from previous studies on the carbonatite including Blessington (2014) and Drenth (2014) were incorporated with the inverted models during geology differentiation to classify the lithology at Elk Creek.

Geological Background

Discovery and Exploration History

The Elk Creek carbonatite is located in southeastern Nebraska close to the small town of Elk Creek in Johnson county. Discovery of the Elk Creek carbonatite occurred in 1970 when separate surveys from the University of Nebraska-Lincoln identified positive gravity and magnetic anomalies over the deposit (Carlson and Treves, 2005). These initial surveys were ground based geophysical surveys which recorded a gravity relief of about 8 mGal and a magnetic anomaly of about 800 nT across the elliptical deposit (Carlson and Treves, 2005). The Nebraska Geological Survey followed this discovery by drilling a test borehole which identified carbonatite at a depth of about 200 m. (Carlson and Treves, 2005).

By 1973, Molycorp Inc. had acquired the mineral rights to the deposit and started an extensive resource exploration program. The first detailed aeromagnetic survey was flown in the same year by Olympus Aerial Surveys Inc with the aim of locating drill sites (SRK Consulting, 2015). Molycorp's drilling program would complete 106 boreholes by 1986 with the deepest hole reaching a depth of 1,038 m before bottoming in carbonatite (Carlson and Treves, 2005). In 1980, an extensive regional geophysical program of southeastern Nebraska including Elk Creek was conducted involving aeromagnetic measurements and gravity station readings (SRK Consulting, 2015). The aeromagnetic survey was conducted by Olympus Aerial Surveys and the gravity readings were a joint effort between Molycorp and the Conservation and Survey Division of the University of Nebraska.

The mineral rights for the Elk Creek carbonatite were acquired in 2010 by Quantum Rare Earth Developments, now known as NioCorp Developments Ltd (NioCorp). NioCorp contracted Fugro Airborne in 2011 for an airborne geophysical survey over the region collecting aeromagnetic and airborne gravity gradient data (Kass et al., 2015). The survey data closely matched the results of the geophysics surveys conducted in the early 1970's, with borehole data from Molycorp and NioCorp used to characterize the lithology (SRK Consulting, 2015; Drenth, 2014). The magnetite-dolomite carbonatite hosts most of the niobium mineralization, and estimates from borehole data suggested that it composes less than 2% of the estimated volume of the carbonatite. However, the estimated volume was inadequate at explaining the strong magnetic and gravity gradient anomalies measured over the center of the carbonatite (Drenth, 2014). This suggests the possible presence of additional magnetite-dolomite carbonatite and therefore niobium mineralization below the deepest recorded borehole samples.

Geologic Setting

The Elk Creek carbonatite is located in southeastern Nebraska along the eastern margin of the Midcontinental Rift System (MRS). The rift system dates to 1.1 Ga, with the western portion of the rift extending about 1300 km from the Lake Superior region to northeastern Kansas (Ojakangas et al., 2001). The rift system was active for over 25 million years, with volcanic activity and tectonic activity resulting in the formation of basalt and gabbro intrusions (Carlson and Treves, 2005).

The Elk Creek carbonatite formed later than the MRS and is dated to about 0.5 Ga (Carlson and Treves, 2005). It was formed as part of a series of carbonatites across North America that may be related to continent-wide stress from continental plate margin interactions (Carlson and Treves, 2005). The Elk Creek carbonatite was also uplifted around 0.3 Ga as part of the Late Paleozoic Nemaha uplift which subjected the carbonatite to major erosion (Carlson and Treves, 2005). It was later reburied under Pennsylvanian marine sedimentary material and now lies about 200 m below the surface with no surface outcrops (Drenth, 2014).

Lithology

The lithology of the Elk Creek Carbonatite mostly consists of silicate and carbonatite rocks. It is important to note that two different nomenclatures for studies into the lithology at Elk Creek have been used (**Table 1**). Drill logs from Molycorp and research relying on them as in Drenth (2014) use historic nomenclature preferring the term *beforsite*, referring to carbonatite lithology with dolomite as a primary material. The present nomenclature preferring the term *dolomite carbonatite* to refer to the same lithology is used in drill logs from NioCorp and in most studies on Elk Creek such as Xu (1996), Blessington

(2014), and Campbell (2017). In addition to nomenclature changes, a significant classification change was made to Molycorp's mapping of apatite beforsite (I & II). Apatite-dolomite carbonatite (apatite beforsite) is a variant of dolomite carbonatite with significant apatite mineralization. NioCorp reclassified the majority of Molycorp's mapping of apatite-dolomite carbonatite as dolomite carbonatite with locally abundant apatite mineralization (Campbell, 2017). This difference also affects studies such as Drenth (2014), which classified the majority of the dolomite carbonatite at Elk Creek as apatite-dolomite carbonatite. An important note is that the apatite beforsite breccia mentioned in Drenth (2014) was estimated to compose only 1% of the relative volume of the lithology, and is not a lithologic unit defined in Blessington (2014) as it was likely combined with the dolomite carbonatite breccia.

Table 1: Updated nomenclature of the Elk Creek lithology, adapted from Campbell, 2017

Updated Nomenclature

Historic	Present
Dolomite Beforsite	Dolomite Carbonatite
Magnetite Beforsite	Magnetite-Dolomite Carbonatite
Beforsite Breccia	Dolomite Carbonatite Breccia
Younger Mafic	Lamprophyre
Older Mafic	Mafic
Apatite Beforsite (I & II)	Apatite-Dolomite Carbonatite
Apatite Beforsite Breccia	*
Barite Beforsite	Barite-Dolomite Carbonatite
Syenite	Syenite

The Elk Creek Carbonatite was originally discovered as a gravity and magnetic anomaly, so it stands to reason the various lithologies comprising it and the surrounding basement have different density and magnetic susceptibility values. **Figure 1** shows the distribution of lithology within the ECCC and was constructed from about 100 public-domain legacy boreholes from Molycorp (Drenth, 2014). Physical property logs from the drill core samples were used in Drenth (2014) to construct **Figure 2**. Drenth (2014) used these physical properties to group the lithologies within the ECCC into 3 groups. This grouping was expanded in Kass et al. (2015) to include the country rock. The groupings in Kass et al. (2015) were (1) country rock, (2) undifferentiated carbonatite and syenite, (3) mafic rocks, and (4) magnetite-dolomite carbonatite. The country rocks (1) are less dense than the other groupings at Elk Creek, but is more magnetized than the undifferentiated carbonatites (2). The undifferentiated carbonatites include dolomite carbonatite, dolomite carbonatite breccia, apatite-dolomite carbonatite, barite-dolomite carbonatite, and syenite. Syenite is not a carbonatite and is instead a silicate rock which shares similar physical properties with the carbonatite (Xu, 1996; Drenth, 2014). The mafic rocks (3) include lamprophyre and undifferentiated mafic rocks and on average are denser than the country rocks and strongly magnetized. The final grouping is the magnetite-dolomite carbonatite (4) which is extremely dense and strongly magnetized.

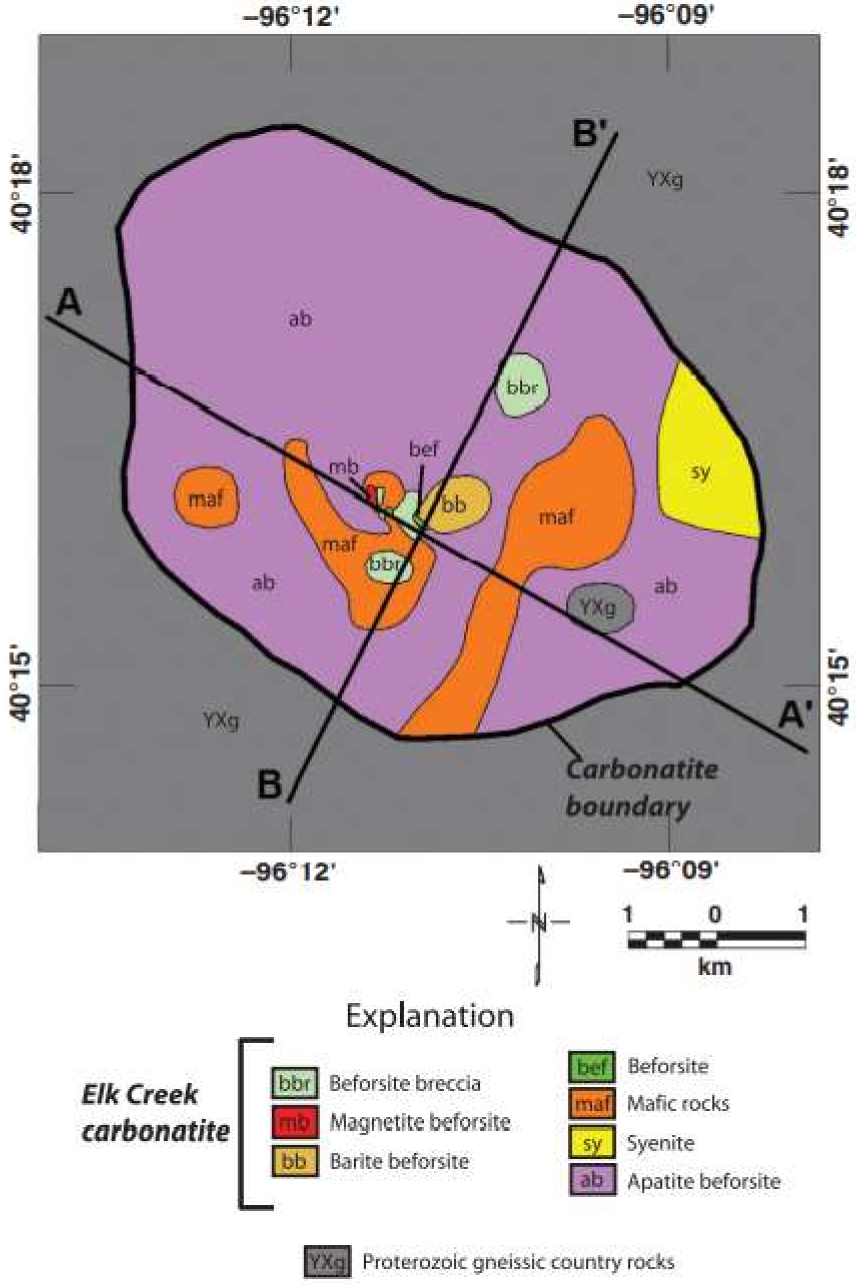

Figure 1: Geology of the Elk Creek Carbonatite at a depth of about 230m. From Drenth (2014)

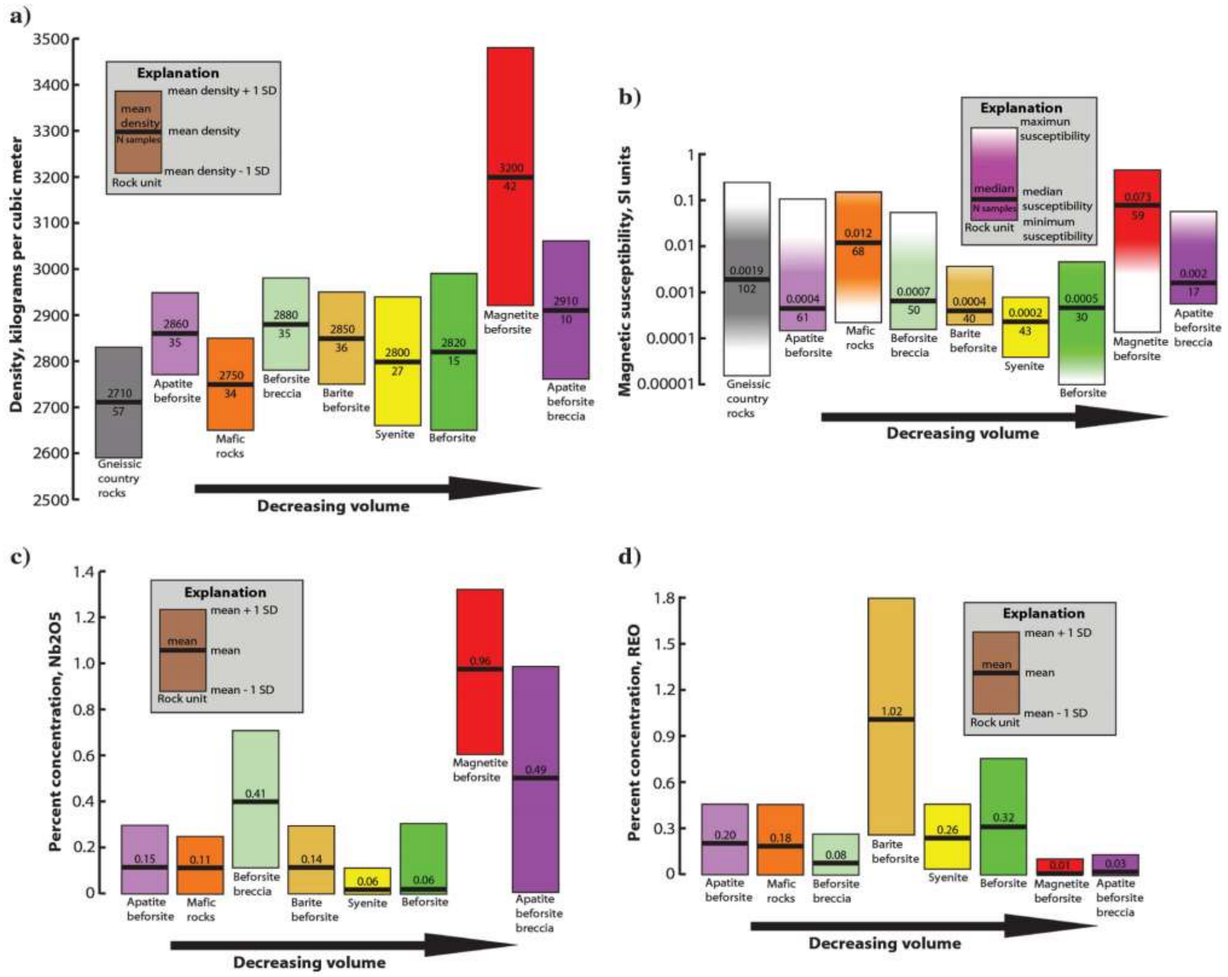

Figure 2: Physical property data for the Elk Creek lithology sorted by relative volume. (a) density, (b) magnetic susceptibility, (c) Nb_2O_5 (Niobium Pentoxide) concentration, (d) rare earth oxides. From Drenth (2014)

Basement/Country Rock

The country rock surrounding the Elk Creek carbonatite is composed of a heterogeneous mix of Precambrian igneous and metamorphic rocks, including gneiss, granites, diorites, gabbros, and schists (Xu, 1996). However, other parts of the Precambrian basement in Nebraska includes flood basalts (Carlson and Treves, 2005). The Elk Creek carbonatite was discovered as a positive gravity and magnetic anomaly from geophysics surveys, which is reflected in the physical properties recorded in Drenth, 2014. From core samples of the basement rock near the carbonatite, the gneissic country rocks are on average less dense than the other lithologies. However, the magnetic susceptibility of the country rocks covers a wide range although the mean magnetic susceptibility is lower than the mafic rocks and magnetite-dolomite carbonatite. This wide range of values is likely due to the heterogeneous nature of the Precambrian country rocks.

Dolomite Carbonatite

The prevalent lithology of the Elk Creek carbonatite is dolomite carbonatite. The mineral composition of the unit is primarily dolomite with fluorite, pyrite, pyrochlore, hematite, ilmenite, magnetite, and barite as accessory minerals (Blessington, 2014). In terms of physical properties, the unit is difficult to distinguish from other carbonatites except for the niobium hosting magnetite-dolomite carbonatite. The mean density of the dolomite carbonatite is well within the range of 2800 to 2910 kg/m^3 of the other undifferentiated carbonatites (Drenth, 2014). Additionally, the median magnetic susceptibility is within an order of the other undifferentiated carbonatites (Drenth, 2014). Overall, the unit is not a significant source of niobium mineralization although resource-grade niobium mineralization may be found in localized areas on a meter-scale (Blessington, 2014).

Apatite-Dolomite Carbonatite

A variant of the dolomite carbonatite with significant apatite mineralization. Apatite-Dolomite carbonatite is often found in localized regions at Elk Creek, around altered regions of dolomite carbonatite (Blessington, 2014). The physical properties of this unit are similar to the other undifferentiated carbonatites (Kass et al., 2015). This unit is not a source of significant niobium mineralization.

Magnetite-Dolomite Carbonatite

The magnetite-dolomite carbonatite is the primary exploration target for niobium. Backscattered electron imaging and energy dispersive spectrometry identified the primary rock-forming minerals as magnetite, ilmenite, dolomite, barite with minor apatite, rutile, biotite, quartz, and pyrochlore (Blessington, 2014). It has distinct physical properties from the surrounding lithology as a relatively dense and strongly magnetic rock. The median density of the magnetite-dolomite carbonatite is 3200 kg/m^3 while the rest of the lithologic units have mean densities ranging from 2710 to 2910 kg/m^3 (Drenth, 2014). Additionally, the mean magnetic susceptibility of the magnetite-dolomite carbonatite is orders of magnitude larger than the other carbonatites (Drenth, 2014). It is located near the center of the Elk Creek carbonatite, and comprises only an estimated 2% relative volume (Drenth, 2014).

Dolomite Carbonatite Breccia

This lithologic unit is comprised of clasts of dolomite carbonatite, magnetite-dolomite carbonatite, and mafic rock contained within a dolomite carbonatite matrix. The lithologic unit is found in significant deposits in the complex with an estimated relative volume of 15% (Drenth, 2014). Depending on the occurrence of magnetite-dolomite clasts within the rock, there may be significant levels of niobium mineralization (Blessington, 2014). Overall, the breccia shares similar physical properties to the other undifferentiated carbonates although the range of sampled density and susceptibility values is larger (Drenth, 2014). This means identifying the dolomite carbonatite breccia using gravity gradiometry and magnetic data for niobium exploration is unfeasible.

Barite-Dolomite Carbonatite

The majority of the Rare Earth Element (REE) mineralization at Elk Creek occurs in barite-dolomite carbonatite. From core samples, barite-dolomite carbonatite was not intercepted in the niobium ore zone outside of centimeter scale veinlets (Blessington, 2014). Instead, massive barite-dolomite carbonatite was found occurring outside of the niobium ore zone with rich REE mineralization (Blessington, 2014). This mineralization includes monazite, xenotime, bastnaesite, and parasite (Blessington, 2014). Unfortunately, the rock shares physical properties with the other undifferentiated carbonatites, preventing REE mapping using geophysics data.

Mafic Dikes

The Elk Creek complex is cut by many intrusive mafic dikes, including ones containing lamprophyre. The lamprophyre dikes can be distinguished from the other undifferentiated mafic dikes due to the presence of biotite grains and from observations of low magnetization (Blessington, 2014). In comparison, the undifferentiated mafic dikes have high magnetic susceptibility when unaltered (Blessington, 2014). From core sample measurements, the mafic rocks have a lower mean density than the carbonatites at Elk Creek and are closer in density to the country rock (Drenth, 2014). The mafic rocks also cut through nearly all other lithologic units (Blessington, 2014). These rocks are not a significant source of niobium, and are likely the second most common lithology at Elk Creek comprising an estimated 15% volume of the complex (Drenth, 2014).

Methodology

Geophysics

Gravity Gradiometry

Gravity gradiometry is defined as the second derivative of gravitational potential, or the spatial rate of change of gravitational acceleration. Considering that gravitational acceleration is a vector with three components (G_x, G_y, and G_z) and each can change in three spatial directions (x, y, and z), this means that a full measurement of a gravity gradient field can be summarized as a tensor consisting of nine components. This tensor is defined below (Heiland, 1968):

$$\Delta \boldsymbol{G} = \begin{bmatrix} G_{xx} & G_{xy} & G_{xz} \\ G_{yx} & G_{yy} & G_{yz} \\ G_{zx} & G_{zy} & G_{zz} \end{bmatrix} \tag{1}$$

It is important to note that gravitational potential has the important properties of being well-behaved and harmonic outside the source region (Li & Krahenbuhl, 2015). This means that the tensor field has the properties of being symmetrical and having zero trace. Consequently, there that there are only five independent components within Eq. (1): G_{xx}, G_{xy}, G_{yy}, G_{xz}, and G_{zz} when noise is ignored. In practice, different components tend to have different noise characteristics. Therefore, multiple components are usually measured.

The benefit of measuring the gravity gradient over gravity is the increased amount of high-frequency information. This allows for easier delineation of shallower anomalies and structural changes such as faults. In this study, the coordinate system used defined x as northing, y as easting, and z as vertical depth. Using this convention, the Falcon® Airborne Gravity Gradiometry (AGG) instrument used to measure data at Elk Creek collects data in the G_{NE} and G_{UV} components, where $G_{NE} = G_{xy}$ and $G_{UV} = (G_{xx} - G_{yy})/2$. However, these components were also transformed to the vertical gravity gradient (G_{zz}) component through Fourier domain and equivalent source methods (Fugro Airborne Surveys, 2011). Pilkington (2012) analyzed the eigenvalue spectra of different gravity gradient components in order to determine the utility of combining them in a 3D linear problem. He concluded that G_{zz} provides the most information as a single component, while using pairs of components such as G_{xy} and G_{uv} appear to show some advantages. However, this is only in a linear case, and the choice of tensor components is highly model dependent and may not be crucial when inverting real datasets provided the signal-to-noise ratio is small enough (Pilkington, 2012; Paoletti et al., 2016).

The Fourier transform is a simple and effective method of converting gravity gradient tensor components, although it does require a few assumptions. Applying the Fourier transform to a dataset assumes that the data shares a common plane, which is not true for airborne surveys which constantly change elevation along a flight path. If we represent G_{xy} as $\frac{\partial G_x}{\partial_y}$, we can represent its Fourier transform as (Mickus & Hinojosa, 2001):

$$\mathcal{F}\left[\frac{\partial G_x}{\partial_y}\right] = \; i w_y \mathcal{F}[G_x] \tag{2}$$

where $G_x = \frac{\partial \phi}{\partial x}$ and ϕ is the gravitational potential measured at some location. This can be expanded into the following equation:

$$\mathcal{F}\left[\frac{\partial G_x}{\partial_y}\right] = \left(i w_y\right)(i w_x)\mathcal{F}[\phi] = -w_x w_y \mathcal{F}[\phi] \tag{3}$$

Following this same process, we can represent G_{zz} as $\frac{\partial G_z}{z}$ to obtain the following equation:

$$\mathcal{F}\left[\frac{\partial G_z}{\partial_z}\right] = (i w_z)(i w_z)\mathcal{F}[\phi] = -w_z^2 \mathcal{F}[\phi] \tag{4}$$

We can now find a Fourier domain operator to convert $\mathcal{F}[\frac{\partial G_x}{\partial_y}]$ to $\mathcal{F}[\frac{\partial G_z}{\partial_z}]$.

$$\mathcal{F}\left[\frac{\partial G_x}{\partial_y}\right]\left(-\frac{1}{w_x w_y}\right) = F[\phi] \tag{5}$$

$$\mathcal{F}\left[\frac{\partial G_z}{\partial_z}\right] = -w_z^2 \mathcal{F}[\phi] = \frac{w_z^2}{w_x w_y}\mathcal{F}\left[\frac{\partial G_x}{\partial_y}\right] \tag{6}$$

$$\mathcal{F}\left[\frac{\partial G_z}{\partial_z}\right] = \frac{w_z^2}{w_x w_y} F\left[\frac{\partial G_x}{\partial_y}\right] \tag{7}$$

At this point, converting $\frac{\partial G_x}{\partial_y}$ to $\frac{\partial G_z}{\partial_z}$ merely involves finding the inverse Fourier transform:

$$\frac{\partial G_z}{\partial_z} = F^{-1}\left[\frac{w_z^2}{w_x w_y} F\left[\frac{\partial G_x}{\partial_y}\right]\right] \tag{8}$$

Gravity gradient tensor components can also be converted through the equivalent source method. This method involves constructing a layer of fictitious density anomalies to replicate the response of a recorded gravitational field (Dampney, 1969). This is typically done by solving an inverse problem. This technique is often used for the upward/downward continuation of gravity data, but can also be used for component conversions of gravity gradient data. The results of Fourier domain and equivalent source methods of gravity gradient component conversions are almost equivalent when performed correctly and when the data are collected on an even plane. For measurements taken on an uneven plane, the Fourier transform method isn't suitable, making the equivalent source method the most widely used for component conversions.

Magnetics

A magnetic survey in geophysics measures the Earth's magnetic field, typically its strength, in a survey region. The magnetic anomalies, ΔT, can then be obtained by subtracting the regional background, e.g., based on the International Geomagnetic Reference Field (IGRF). By defining the background field as B_0 and the anomalous field as B_A, the magnetic anomalies can be represented with the following equation (Blakely, 1996):

$$\Delta T = |\boldsymbol{B}_0 + \boldsymbol{B}_a| - |\boldsymbol{B}_0| \tag{9}$$

The total magnetization (M_T) is the vector addition of the remanent (M_R) and induced (M_I) components of the magnetic field (Grant & West, 1965; Telford et al., 1990; Blakely, 1996; Hinze et al., 2013). The induced magnetization is dependent on the magnetic susceptibility (κ) of the source body along with the magnitude and direction of the inducing field. In magnetic surveys, the inducing field (**H**) is Earth's present magnetic field at the location of the survey. The inducing field can be expressed with the following equation (Blakely, 1996):

$$\boldsymbol{M}_I = \kappa \boldsymbol{H} \tag{10}$$

The remanent magnetization of a source body is dependent on the nature of the source body and its magnetic history. The remanent magnetization recorded in a source body is a record of the Earth's inducing field during the geologic history of the rock, and can be oriented differently from other nearby units due to tectonics and geological processes as well as polarity reversals of the Earth's magnetic field. The total magnetization is represented by the following equations, and is depicted in **Figure 3**:

$$\boldsymbol{M}_T = \boldsymbol{M}_I + \boldsymbol{M}_R \tag{11}$$

$$\boldsymbol{M}_T = \kappa \boldsymbol{H} + \boldsymbol{M}_R \tag{12}$$

Crystalline rocks typically have strong remanent and induced magnetization while heavily altered sedimentary layers are normally weakly magnetized (Butler, 1992). Mafic rocks are rich in iron and normally produce strong anomalies under induced magnetization, although fine grained mafic rocks can also exhibit strong remanence (Butler, 1992).

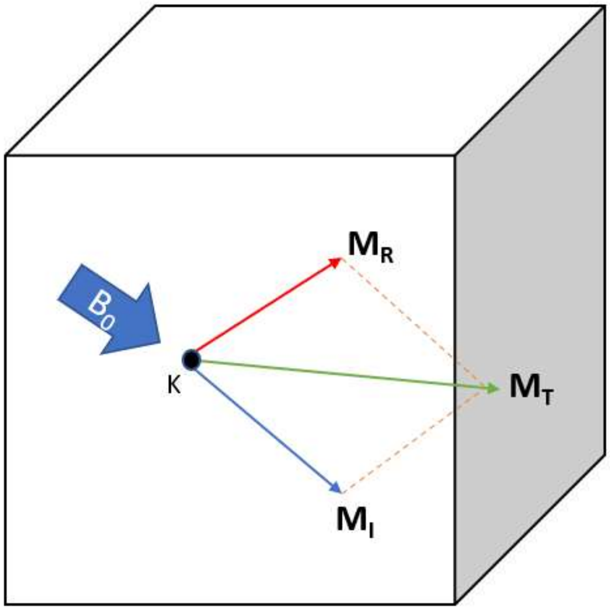

Figure 3: A visual representation of the total magnetization response of a cubic source body. B_0 *is the background field,* κ *is the magnetic susceptibility,* M_I *is the induced component,* M_R *is the remanent component, and* M_T *is the total magnetization*

The total magnetic intensity (TMI) recorded by magnetometers cannot be directly used in geophysics inversion. The TMI (B_T) is a composite of the background field (B_0) and the anomalous field (B_a). The background field is removed from the TMI in order to obtain the residual magnetic anomaly resulting from local geology. This is represented in the following equation:

$$\boldsymbol{B}_a = \boldsymbol{B}_T - \boldsymbol{B}_0 \tag{13}$$

For the Elk Creek dataset used in this study, the given magnetic data was TMI data which required processing in order to obtain the anomalous field data used for inversion.

Inversion

Separate Inversion

An inverse problem in geophysics refers to the process of taking geophysical data and using it to determine structures from the Earth's interior. Due to the complexity of geologic structures, inverse problems are represented simplistically with the forward modeling equation $\boldsymbol{Gm} = \boldsymbol{d}$ where **d** is the resulting data between the interaction of a model **m** and an operator **G** representing the physics of the problem (Menke, 1984). The goal of inversion is to solve for model **m** which is normally done through a regularized objective function

$$\min \phi(\boldsymbol{m}) = \frac{1}{2}\left|\left|\boldsymbol{W}_d\left(\boldsymbol{Gm} - \boldsymbol{d}^{obs}\right)\right|\right|^2 + \frac{1}{2}\beta\left|\left|\boldsymbol{W}_m\left(\boldsymbol{m} - \boldsymbol{m}^{ref}\right)\right|\right|^2 \tag{14}$$

where φ is the objective function, $\mathbf{W}_\mathrm{d}$ and $\mathbf{W}_\mathrm{m}$ are weight parameters, β is a regularization parameter, $\mathbf{d}^{\mathrm{obs}}$ represents observed data, and $\mathbf{m}^{\mathrm{ref}}$ is a reference model. The first term in **Equation 14** is referred to as the data misfit term and measures how well the observed data are reproduced by an inverted model. The second term is a form of Tikhonov regularization, which stabilizes the inverse solution (Tikhonov & Arsenin, 1977; Zhdanov, 2002). A minimized objective function is used in geophysical inversion due to two main problems with inverse problems: non-uniqueness and instability. Non-uniqueness refers to the existence of infinite solutions for inverse problems while instability refers to the impact that noise has upon the resulting inverted models. A minimized objective function attempts to stabilize the inverse problem and minimize misfits within the problem in order to obtain an approximated solution.

Joint Inversion

Simultaneous joint inversion is an expansion of standard geophysical inversion to incorporate multiple datasets for better modeling of geological structure. The implementation of joint inversion contains multiple subcategories of different approaches. The simplest is single-property joint inversion, which combines data from geophysical methods that are sensitive to the same physical parameters (Li and Oldenburg, 2000). Due to the shared physical properties, a mathematical coupling term to relate the datasets is unnecessary, although care is required to ensure anisotropic effects do not distort the resulting model (Li and Oldenburg, 2000; Moorkamp et al., 2010; Moorkamp et al., 2016). In comparison, multi-property joint inversion is more complex and includes structurally or property coupled approaches to combine different physical properties. Physical property coupled joint inversion is most commonly used when borehole data or rock sample measurements are available. Different physical properties, such as velocity and conductivity, might be sensitive to the same petrophysical properties, such as porosity and saturation, and are therefore correlated (Gardner et al. 1974). However, this approach to joint inversion is relies upon the availability of well-defined relations between different physical properties. Structurally coupled approaches to joint inversion do not suffer from this drawback, as it is focused on producing coincident boundaries or gradients between different physical properties (Haber & Gazit, 2013; Moorkamp et al., 2016).

Joint Inversion Objective Function

Logically, incorporating another dataset into the objective function for joint inversion would consist of appending similar data misfit and regularization terms. However, an additional term must be added to incorporate the exchange of information between the datasets during inversion. This is referred to as the coupling term $\boldsymbol{\phi_c}$, which is also associated with a weighting parameter λ. The following equation is an expansion of **Equation 14** for joint inversion:

$$\min J(m) = \frac{1}{2}\left|\left|\boldsymbol{W}_{d1}\left(\boldsymbol{G}_1\boldsymbol{m}_1 - \boldsymbol{d}_1^{obs}\right)\right|\right|^2 + \frac{1}{2}\beta_1\left|\left|\boldsymbol{W}_{m1}\left(\boldsymbol{m}_1 - \boldsymbol{m}_1^{ref}\right)\right|\right|^2 \tag{15}$$

$$+ \frac{1}{2}\left|\left|\boldsymbol{W}_{d2}\left(\boldsymbol{G}\boldsymbol{m}_2 - \boldsymbol{d}_2^{obs}\right)\right|\right|^2 + \frac{1}{2}\beta_2\left|\left|\boldsymbol{W}_{m2}\left(\boldsymbol{m}_2 - \boldsymbol{m}_{\boldsymbol{2}}^{ref}\right)\right|\right|^2 + \lambda\boldsymbol{\phi}_c$$

where the subscripts 1 and 2 refer to separate physical properties. The coupling term is at the core of joint inversion because it determines how the two physical property models interact and influence each other. Currently, the most popular structural coupling term in published geophysics papers is the cross-gradient from Gallardo and Meju (2003, 2007, 2011) which uses the cross products of gradient fields. Another coupling term is the Gramian constraint which is based on minimizing the determinant of the Gram matrix of different models (Zhdanov et al., 2012). Haber and Gazit (2013) introduced the joint total variation coupling term which minimizes the total variation between different models. Structural coupling methods do not force coupled models to share the same structural boundaries, but instead encourage couple models to share boundaries through the minimization of the coupling terms. An important note is that for all coupling terms if $\lambda = 0$, this indicates that the coupling term does not influence the inverse results, so solving the objective function produces the same results as single inversion of the different datasets. Increasing values of λ exerts stronger influence of the coupling term on the inverse solution during joint inversion.

Joint Total Variation

The first coupling term used for my joint inversion work is Joint Total Variation (JTV) regularization as defined in Haber and Gazit (2013). JTV is the multi-parameter expansion of total variation regularization, which was originally developed in the imaging community to obtain reconstructions with sharp edges (Rudin et al., 1992). Structural coupling methods such as JTV define a mechanism for exchanging structural information between models to link them. Structure-based joint inversion aims to increase the structural similarity between inverted models through the coupling terms.

Joint total variation operates through measuring the gradient differences between two models m_1, m_2 in order to measure the structural similarity between them. A high JTV value indicates that there are large gradient and therefore structural differences between the two models, which must be minimized during joint inversion. A unique property of JTV joint inversion is that the JTV coupling term also acts as a regularization term during joint inversion, which affects the convergence of the objective function (Haber & Gazit, 2013; Crestel, 2017).

Total variation (TV) is defined as a non-smooth convex functional with the following equation (Haber & Gazit, 2013; Crestel, 2017):

$$R_{TV}(\boldsymbol{m}) = \int_{\Omega} |\nabla \boldsymbol{m}| dx \tag{16}$$

where $\nabla \boldsymbol{m}$ refers to the gradient field of a model **m**. Unfortunately, **Equation 16** is highly nonlinear and non-differentiable when $|\nabla \boldsymbol{m}| = 0$. Instead, the functional can be modified by approximating the L^1 norm to regularize it along with adding a small value ε:

$$R_{TV}(\boldsymbol{m}) = \int_{\Omega} \sqrt{|\nabla \boldsymbol{m}|^2 + \varepsilon}\, dx \tag{17}$$

Assuming there are two models $\boldsymbol{m}_1, \boldsymbol{m}_2$, the two model gradients can be coupled together with the multi-parameter expansion of the modified functional for JTV defined as the following (Haber & Gazit, 2013):

$$R_{JTV}(\boldsymbol{m}_1, \boldsymbol{m}_2) = \int_{\Omega} \sqrt{|\nabla \boldsymbol{m}_1|^2 + |\nabla \boldsymbol{m}_2|^2 + \varepsilon}\, dx \tag{18}$$

With the JTV coupling term, **Equation 15** now becomes:

$$\begin{aligned} \min \phi(\boldsymbol{m}) = \frac{1}{2}\left|\left|\boldsymbol{W}_{d1}\left(\boldsymbol{G}_1\boldsymbol{m}_1 - \boldsymbol{d}_1^{obs}\right)\right|\right|^2 + \frac{1}{2}\beta_1 \left|\left|\boldsymbol{W}_{m1}\left(\boldsymbol{m}_1 - \boldsymbol{m}_1^{ref}\right)\right|\right|^2 + \frac{1}{2}\left|\left|\boldsymbol{W}_{d2}\left(\boldsymbol{G}\boldsymbol{m}_2 - \boldsymbol{d}_2^{obs}\right)\right|\right|^2 \\ + \frac{1}{2}\beta_2 \left|\left|\boldsymbol{W}_{m2}\left(\boldsymbol{m}_2 - \boldsymbol{m}_2^{ref}\right)\right|\right|^2 + \lambda \int \sqrt{|\nabla \boldsymbol{m}_1|^2 + |\nabla \boldsymbol{m}_2|^2 + \varepsilon}\, dx \end{aligned} \tag{19}$$

Cross Gradient

The cross-gradient coupling term is commonly used in structurally based joint inversion of geophysics data. Much like JTV, the cross-gradient term exchanges structural information through structural similarity measurements based on model gradients. It was first proposed in Gallardo and Meju (2003), and has become the most popular coupling strategy for joint inversion. Cross-gradient joint inversion has been used in multiple studies including Fergoso and Gallardo (2009), Bennington et al. (2014), and Shi et al. (2017). The cross-gradient operates by trying to align the gradients of two parameter fields such as in **Figure 4** at each point within the medium (Crestel et al., 2018). The cross-gradient term incorporates the cross-product of two vectors, and will equal zero at locations where $|\nabla \boldsymbol{m}_1|$ and $|\nabla \boldsymbol{m}_2|$ align, indicating that the two models share a common boundary (Gallardo & Meju, 2003; Crestel et al., 2018). Additionally, the cross-gradient term will vanish when either $|\nabla \boldsymbol{m}_1|$ or $|\nabla \boldsymbol{m}_2|$ also vanish, allowing cross-gradient joint inversion to incorporate geological boundaries which only occur in the physical property changes of one model (Gallardo & Meju, 2003).

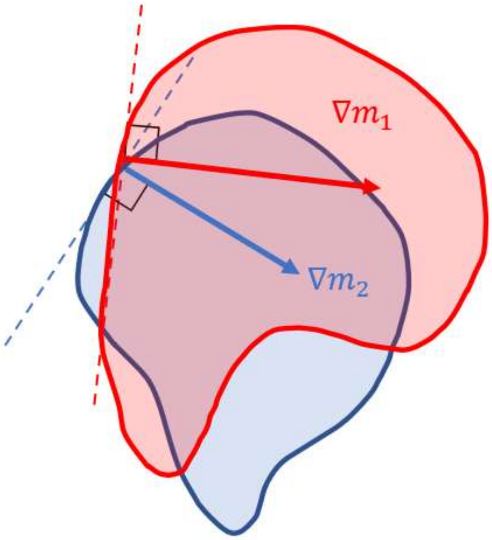

Figure 4: Sketch of two parameter fields with their respective gradients at a point. Based on Crestel et al., 2018

The cross-gradient term is defined using the following equation (Gallardo & Meju, 2003):

$$R_{CG}(\boldsymbol{m}_1, \boldsymbol{m}_2) = \frac{1}{2}\int_{\Omega} |\nabla \boldsymbol{m}_1(x) \times \nabla \boldsymbol{m}_2(x)|^2 \, dx \tag{20}$$

An easier to discretize version of the above equation can be obtained by using the dot-product and adding a small value ε:

$$R_{CG}(\boldsymbol{m}_1, \boldsymbol{m}_2) = \int_{\Omega} |\nabla \boldsymbol{m}_1(x)|^2 \, |\nabla \boldsymbol{m}_2(x)|^2 - \left(\nabla \boldsymbol{m}_1(x) \cdot \nabla \boldsymbol{m}_2(x)\right)^2 + \varepsilon \, dx \tag{21}$$

This results in the following expansion of **Equation 14**:

$$\begin{aligned} \min \phi(m) = {} & \frac{1}{2}\left\|\boldsymbol{W}_{d1}\left(\boldsymbol{G}_1 \boldsymbol{m}_1 - \boldsymbol{d}_1^{obs}\right)\right\|^2 + \frac{1}{2}\beta_1 \left\|\boldsymbol{W}_{m1}\left(\boldsymbol{m}_1 - \boldsymbol{m}_1^{ref}\right)\right\|^2 \\ & + \frac{1}{2}\left\|\boldsymbol{W}_{d2}\left(\boldsymbol{G}\boldsymbol{m}_2 - \boldsymbol{d}_2^{obs}\right)\right\|^2 + \frac{1}{2}\beta_2 \left\|\boldsymbol{W}_{m2}\left(\boldsymbol{m}_2 - \boldsymbol{m}_2^{ref}\right)\right\|^2 \\ & + \lambda \int |\nabla \boldsymbol{m}_1(x)|^2 \, |\nabla \boldsymbol{m}_2(x)|^2 - \left(\nabla \boldsymbol{m}_1(x) \cdot \nabla \boldsymbol{m}_2(x)\right)^2 + \varepsilon \, dx \end{aligned} \tag{22}$$

Inversion Algorithm

The above nonlinear inverse problem is solved iteratively through a Gauss-Newton method (GN). In each iteration, the conjugate gradient is used to solve the linearized Gauss-Newton Equation. The algorithm stops once convergence has been achieved. In this study, the inversion is considered to have converged when the relative update of inverted models from two consecutive iterations is smaller than a threshold value (τ = 1e-3) and the objective function no longer decreases (Oldenburg & Li, 2005). The added joint coupling term is also minimized by the inversion algorithm as it reaches convergence.

The linearized Gauss-Newton equation to be solved at each iteration can be summarized as follows (Habashy & Akubakar, 2004) starting with the Newton equation:

$$\boldsymbol{H}\delta\boldsymbol{m} = -g \tag{23}$$

where H represents a Hessian matrix, δm is a perturbation of the model, and g is the gradient of the cost function. Using the representations $J(m) = \frac{dG}{dm}$ for a Jacobian sensitivity matrix, the gradient can be represented as:

$$g(\boldsymbol{m}) = \boldsymbol{J}_1^T\boldsymbol{W}_{d1}^T\boldsymbol{W}_{d1}\left(\boldsymbol{G}_1\boldsymbol{m}_1 - \boldsymbol{d}_1^{obs}\right) + \boldsymbol{J}_2^T\boldsymbol{W}_{d2}^T\boldsymbol{W}_{d2}\left(\boldsymbol{G}_2\boldsymbol{m}_2 - \boldsymbol{d}_2^{obs}\right) \tag{24}$$

$$+\beta_1\boldsymbol{m}_1^T\boldsymbol{W}^T\boldsymbol{W}m_1\left(\boldsymbol{m}_1 - \boldsymbol{m}_1^{ref}\right) + \beta_2\boldsymbol{m}_2^T\boldsymbol{W}^T\boldsymbol{W}\boldsymbol{m}_2\left(\boldsymbol{m}_2 - \boldsymbol{m}_2^{ref}\right) + \frac{\partial\phi_c}{\partial m}$$

where the last term is the gradient of the coupling term. The last term is required in order to solve a joint inversion problem, so the JTV and cross-gradient terms were reformulated to simply the derivation of the gradient term. In the case of JTV, the coupling term can be discretized using a difference matrix $\boldsymbol{D} = [\frac{\boldsymbol{D}_x}{\boldsymbol{D}_y}]$, concatenated identity matrices $\boldsymbol{A} = [\boldsymbol{I}_{m1} \mid \boldsymbol{I}_{m2}]$, and a discretized volume matrix $\boldsymbol{V}$ in the 2D case. This results in the following discretized representation of the JTV coupling term:

$$R_{JTV} = \boldsymbol{V}^T\sqrt{\boldsymbol{A}(\boldsymbol{D}\boldsymbol{m}_1)^2 + \boldsymbol{A}(\boldsymbol{D}\boldsymbol{m}_2)} \tag{25}$$

The first order derivatives of **Equation 25** are shown below, with the term $diag$ referring to diagonal matrices:

$$\nabla_{m1} R_{JTV}(\boldsymbol{m}_1, \boldsymbol{m}_2) = \boldsymbol{D}^T diag\left[\boldsymbol{A}^T diag(\boldsymbol{A}(\boldsymbol{Dm}_1)^2 + \boldsymbol{A}(\boldsymbol{Dm}_2)^2)^{-\frac{1}{2}} \boldsymbol{V}\right] \boldsymbol{Dm}_1 \tag{26}$$

$$\nabla_{m2} R_{JTV}(\boldsymbol{m}_1, \boldsymbol{m}_2) = \boldsymbol{D}^T diag\left[\boldsymbol{A}^T diag(\boldsymbol{A}(\boldsymbol{Dm}_1)^2 + \boldsymbol{A}(\boldsymbol{Dm}_2)^2)^{-\frac{1}{2}} \boldsymbol{V}\right] \boldsymbol{Dm}_2 \tag{27}$$

The second order derivatives for JTV regularization are given as follows:

$$\nabla^2_{m1} R_{JTV}(\boldsymbol{m}_1, \boldsymbol{m}_2) = \boldsymbol{D}^T diag\left[\boldsymbol{A}^T diag(\boldsymbol{A}(\boldsymbol{Dm}_1)^2 + (\boldsymbol{A}(\boldsymbol{Dm}_2)^2)^{-\frac{1}{2}} \boldsymbol{V}\right] \boldsymbol{D} \tag{28}$$

$$\boldsymbol{D}^T diag(\boldsymbol{Dm}_1)\boldsymbol{A}^T diag(\boldsymbol{A}(\boldsymbol{Dm}_1)^2 + (\boldsymbol{A}(\boldsymbol{Dm}_2)^2)^{-\frac{3}{2}} diag(\boldsymbol{V})\boldsymbol{A}\, diag(\boldsymbol{Dm}_1)\boldsymbol{D}$$

$$\nabla^2_{m2} R_{JTV}(\boldsymbol{m}_1, \boldsymbol{m}_2) = \boldsymbol{D}^T diag\left[\boldsymbol{A}^T diag(\boldsymbol{A}(\boldsymbol{Dm}_1)^2 + \boldsymbol{A}(\boldsymbol{Dm}_2)^2)^{-\frac{1}{2}} \boldsymbol{V}\right] \boldsymbol{D} \tag{29}$$

$$\boldsymbol{D}^T diag(\boldsymbol{Dm}_2)\boldsymbol{A}^T diag(\boldsymbol{A}(\boldsymbol{Dm}_1)^2 + (\boldsymbol{A}(\boldsymbol{Dm}_2)^2)^{-\frac{3}{2}} diag(\boldsymbol{V})\boldsymbol{A}\, diag(\boldsymbol{Dm}_2)\boldsymbol{D}$$

For the cross-gradient coupling term, a similar process is followed to obtain the following discretized coupling term in the 2D case where $\odot$ represents the Hadamard product:

$$R_{CG} = [(\boldsymbol{Dm}_1)^2]^T[(\boldsymbol{Dm}_2)^2] - |\boldsymbol{Dm}_1 \odot \boldsymbol{Dm}_2|^2 \tag{30}$$

The first order derivatives of **Equation 30** are shown below:

$$\nabla_{m1} R_{CG} = 2\boldsymbol{D}^T diag((\boldsymbol{Dm}_2)^2)\boldsymbol{Dm}_1 - 2\big(\boldsymbol{D}^T diag(\boldsymbol{Dm}_2)\big)(\boldsymbol{Dm}_1 \odot \boldsymbol{Dm}_2) \tag{31}$$

$$\nabla_{m2} R_{CG} = 2\boldsymbol{D}^T diag((\boldsymbol{Dm}_1)^2)\boldsymbol{Dm}_2 - 2\big(\boldsymbol{D}^T diag(\boldsymbol{Dm}_1)\big)(\boldsymbol{Dm}_1 \odot \boldsymbol{Dm}_2) \tag{32}$$

The second order derivatives for conjugate gradient regularization are the following equations:

$$\nabla^2_{m1} R_{CG} = 2\boldsymbol{D}^T diag((\boldsymbol{Dm}_2)^2)\boldsymbol{Dm}_1 - 2\big(\boldsymbol{D}^T diag(\boldsymbol{Dm}_2)\big)^T\big(\boldsymbol{D}^T diag(\boldsymbol{Dm}_2)\big) \tag{33}$$

$$\nabla^2_{m2} R_{CG} = 2\boldsymbol{D}^T diag((\boldsymbol{Dm}_1)^2)\boldsymbol{Dm}_2 - 2\big(\boldsymbol{D}^T diag(\boldsymbol{D}1)\big)^T\big(\boldsymbol{D}^T diag(\boldsymbol{Dm}_1)\big) \tag{34}$$

Geology Differentiation

Geology differentiation refers to an emerging application of geophysical interpretation to quantitatively identify geologic units. Inversion modeling produces solutions which are fundamentally non-unique, but incorporating geological unit information can reduce the non-uniqueness (Li & Oldenburg, 1996). However, using geophysics to identify different geologic units is much less explored despite applications in mineral exploration that rely on geophysical and geological information to infer geologic units (Li et al., 2019). Geology differentiation maps different geologic units through the differentiation and characterization of multiple physical property models (Martinez & Li, 2015). Differentiation refers to the process of deciding whether anomalous regions in inverted models belong to the same type of unit, while characterization identifies a model region according to lithology or other form of classification. The final product of geology differentiation is not a set of physical property models, but instead a quasi-geology model built with information from the inverted results.

I followed the general workflow of geology differentiation described in Li et al. (2019) to map geologic units in the Elk Creek survey area (**Figure 5**). Geology differentiation is typically based on multiple types of geophysical data which are inverted to produce physical property models. Data associated with different physical properties are used in order to reduce ambiguity when classifying geologic units, as some rock types which may not be differentiable with one survey method may be differentiable using another. The inverted physical property values are visualized and analyzed in a crossplot. The clustering of values in the scatterplot and prior information from the survey area such as geology cross-sections, borehole measurements, and literature sources are combined to organize the inverted values into different groups. The identification of groups within the scatterplot can also be aided by machine learning methods such as in Sun and Li (2017) which applied fuzzy c-means clustering algorithms to enhance cluster differentiation. The identified groupings can be visualized in the 3D spatial domain in order to glean additional insights from the quasi-geology model.

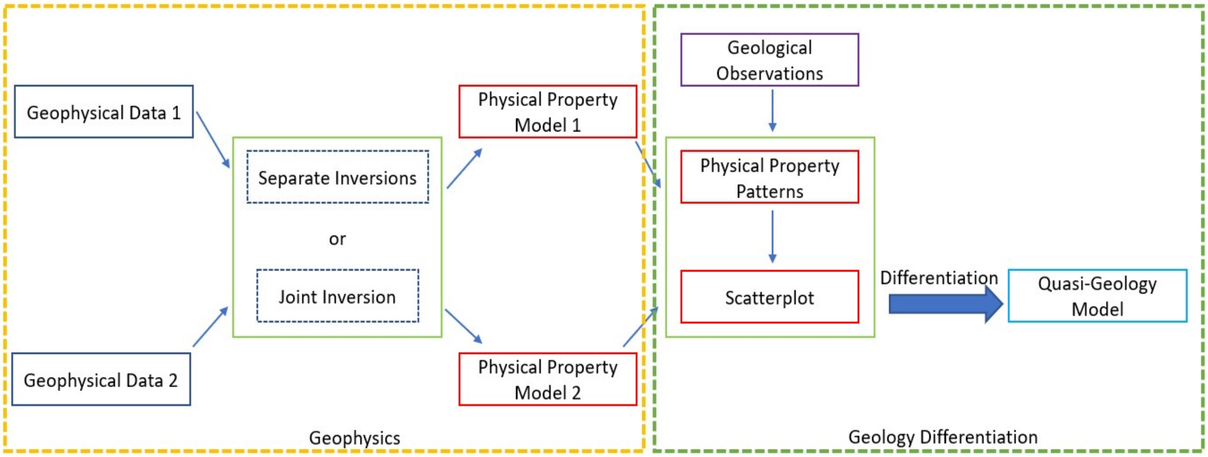

Figure 5: Diagram of geology differentiation workflow, adapted from Li et al. 2019

Computational Environment

The inversion within this study was all performed in the open-source python package SimPEG which was developed as a framework for geophysical inversion (Cockett et al., 2015). The package does not natively support joint inversion, so modifications to the package were made to accommodate structure coupled joint inversions. The implementation for the cross-gradient joint inversion in SimPEG was developed by Jae Deok Kim and Xiaolong Wei at the University of Houston. 3D visualization of the inverted models and the quasi-geology model was performed using the PyVista python package developed by Sullivan et al. (2019), together with a python gadget developed by Xiaolong Wei.

A Preliminary Investigation into Joint Total Variation

Joint total variation was first proposed as a structural coupling strategy in the context of geophysical inversions in Haber and Gazit (2013). There have only been a few synthetic studies into its applications, including Colombo and Stefano (2007) and Crestel (2017) which used 2D models. The application of JTV to the joint inversion of potential field data has not been reported in literature. To better understand its applicability to this study, I designed a synthetic study where 3D density and magnetic susceptibility models were created, and synthetic gravity gradiometry and magnetic data were inverted using joint inversion based on JTV.

Survey Design

In order to analyze the effects of joint total variation based joint inversion, the synthetic 3D survey was designed as a simplistic system of cubic density and susceptibility anomalies with shared locations in space. The anomalies were assigned with a set of higher and lower physical property values in a different pattern between the two models, in order to test the capabilities of JTV. The synthetic 3D survey was designed with a tensor mesh composed of cubic cells with a width of 20 meters. Using a right-handed Cartesian coordinate system, the survey grid extended 60 cells (1200 meters) in the northing and easting directions and 40 cells (800 meters) in depth resulting in a mesh composed of 144,000 cells. Four cubic bodies with a width of 8 cells (160 meters) were placed within the mesh, representing density and magnetic susceptibility anomalies. The density anomalies were assigned density contrast values of -0.3 and +0.3 g/cc (g/cm^3), while the magnetic anomalies were assigned susceptibility contrast values of 0.1 and 0.08 SI. **Figures 5** and **6** show a plan view of the true density and susceptibility models used in this synthetic study. An observation grid was created one meter above the surface of the survey mesh, with 20 meters spacing between the observation points.

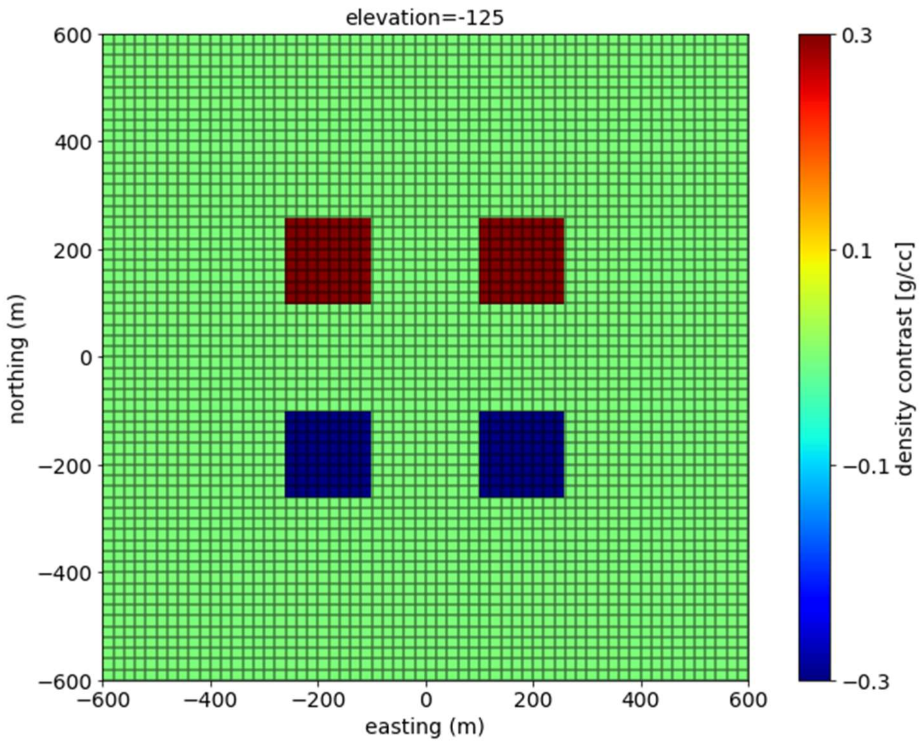

Figure 6: Plan view of the true density model at -125 m elevation

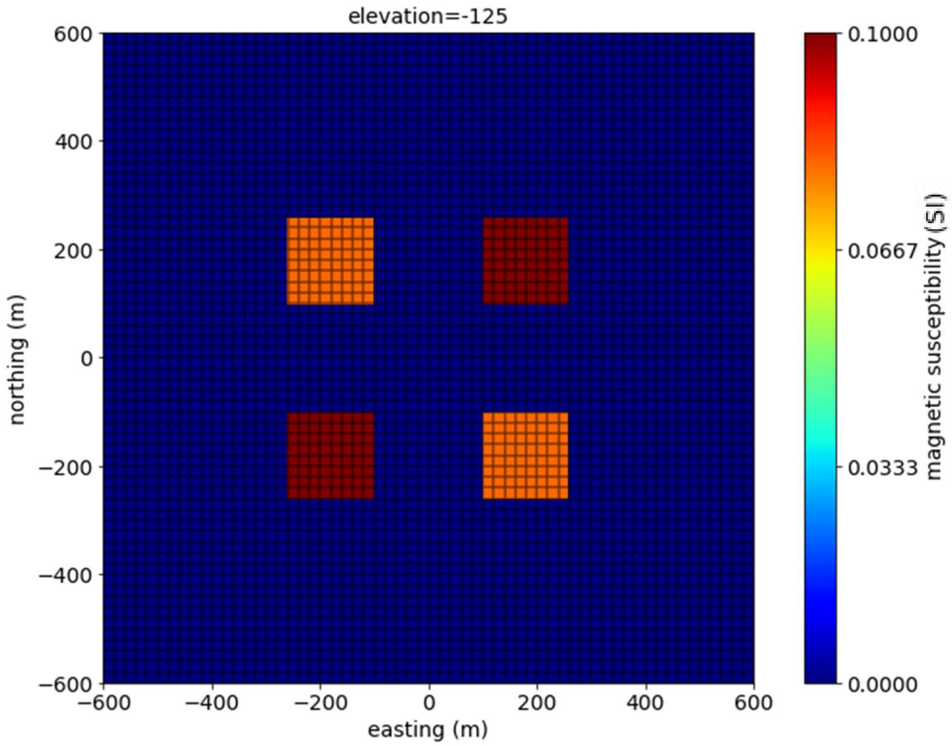

Figure 7: Plan view of the true susceptibility model at -125 m elevation

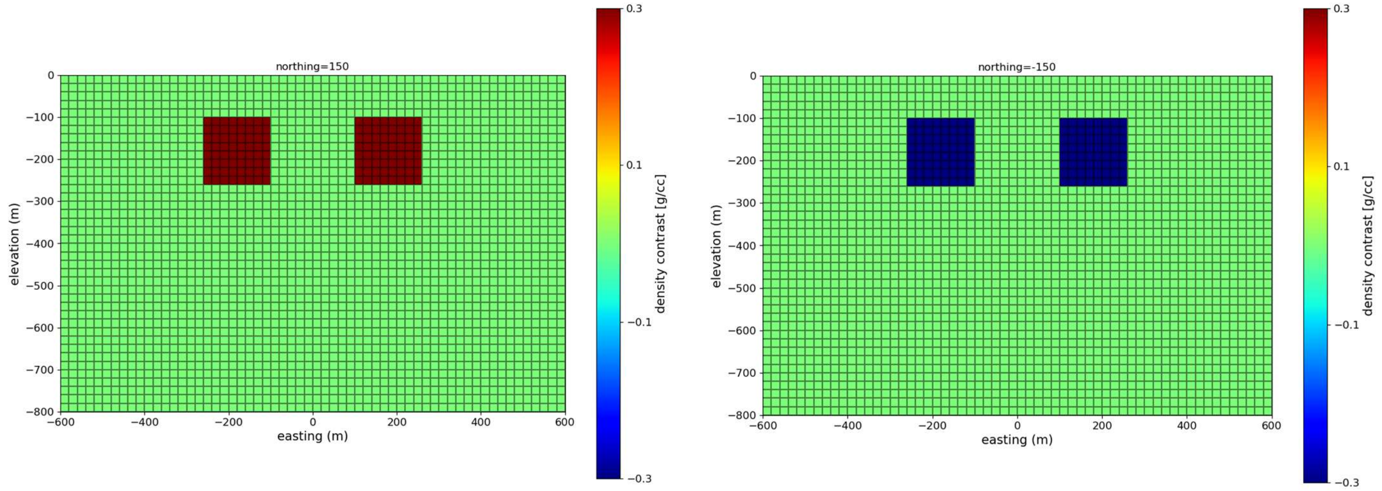

Figure 8:Vertical cross-section of the true density model at northing = -150 m and northing = 150m

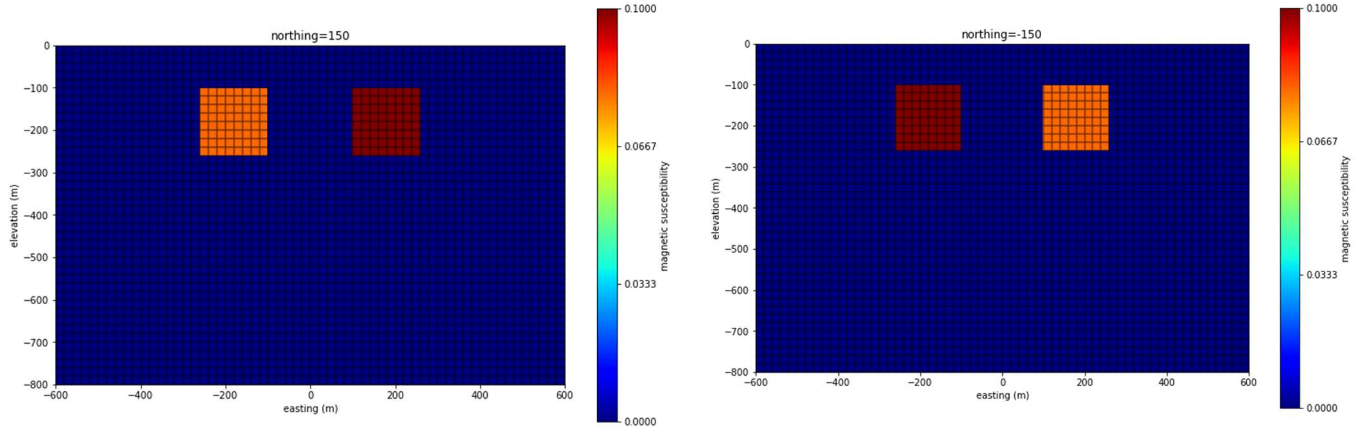

Figure 9: Vertical cross-section of the true susceptibility model at northing = -150 m and northing = 150m

Forward Modeling

The airborne data collected over Elk Creek consists of gravity gradient and magnetic data. Therefore, the same type of data was simulated in this experiment. For the gravity gradient data during synthetic testing, the G_{zz} component was calculated. Although the Falcon® AGG records data the G_{uv} and G_{ne} components, the industry standard is to convert the data to the G_{zz} component for easier interpretation. Preliminary inversion modeling of different gravity gradient components also produced similar models, with practically insignificant differences between them. The forward modeling of the G_{zz} component data and the magnetics data were performed using functions built into SimPEG. Gaussian noise with a standard deviation of 0.1 Eotvos and 30 nT was added to the gravity gradient and magnetic synthetic data respectively.

Inversion

Following the standard practice of potential field data inversion (Li and Oldenburg, 1996;1998), I implemented depth weighting in order to recover the correct depths of the anomalous bodies. I used kernel weighting described in Li and Oldenburg (2000) to counteract the geometric decay of the kernel functions for the gravity gradient and magnetics by distributing the physical property values with depth. For joint inversion involving a coupling term a regularization weight, denoted as λ in **Equation 15**, determines the influence the term has on the inversion. There is currently no established way of automatically determining an optimal value for the weight (Haber & Gazit, 2013; Crestel 2017). Understanding the effect of this weighting parameter required testing of a wide range of values through inversion and comparison of the resulting models. **Figures 10-13** show a sample of the obtained inversion models during testing when $\lambda = 0{,}0.1{,}1$ as more models were produced than shown here. An important note is that $\lambda = 0$ produces nearly the same inversion results as separate inversion as it removes the influence of the coupling term, although the objective function will still attempt to jointly minimize the resulting inverted models.

Gzz Gravity Gradient Inversion

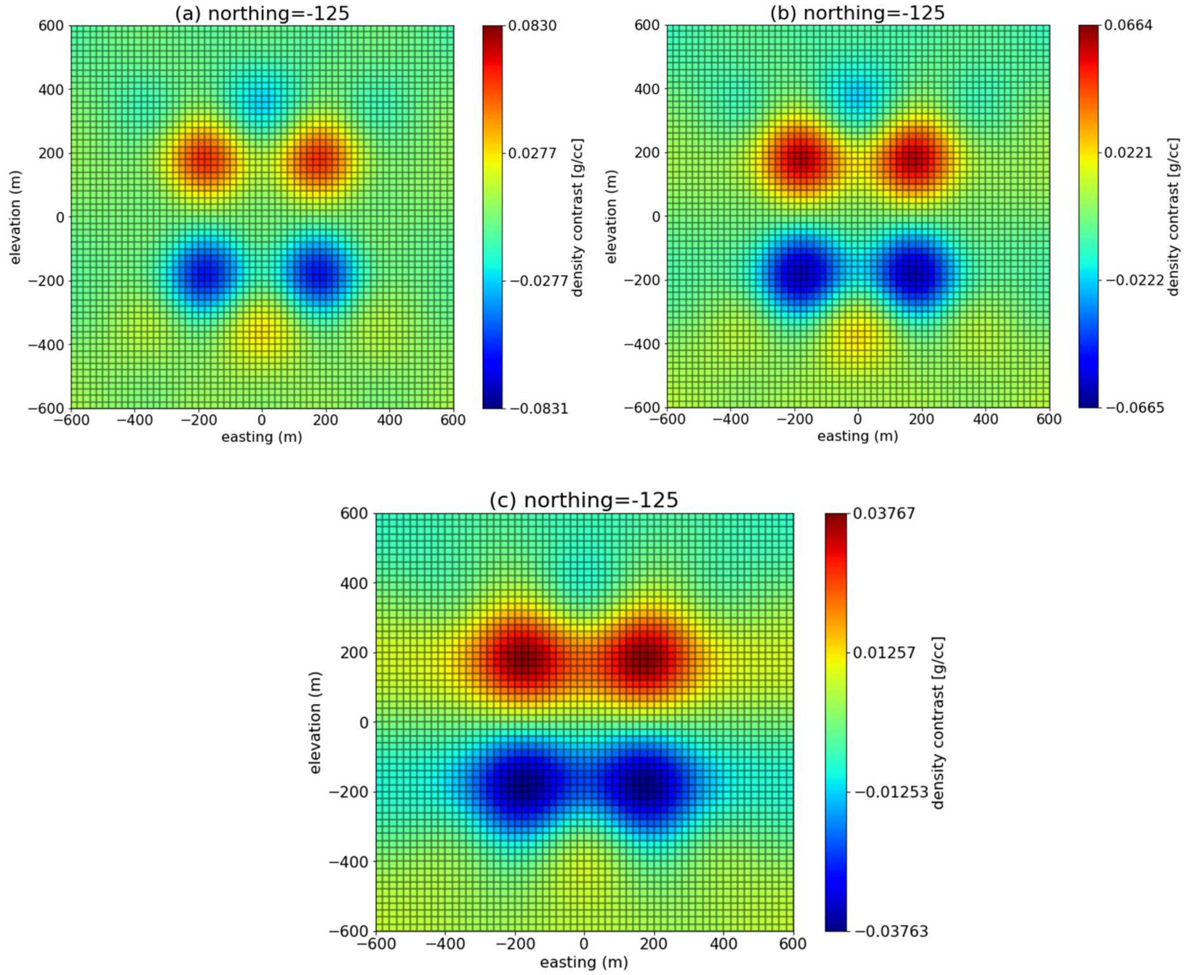

Figure 10: Plan view at -125 m of elevation for the inverted density model from Gzz component of gravity gradient. (a) lambda = 0, (b) Lambda = 0.1, (c) lambda = 1

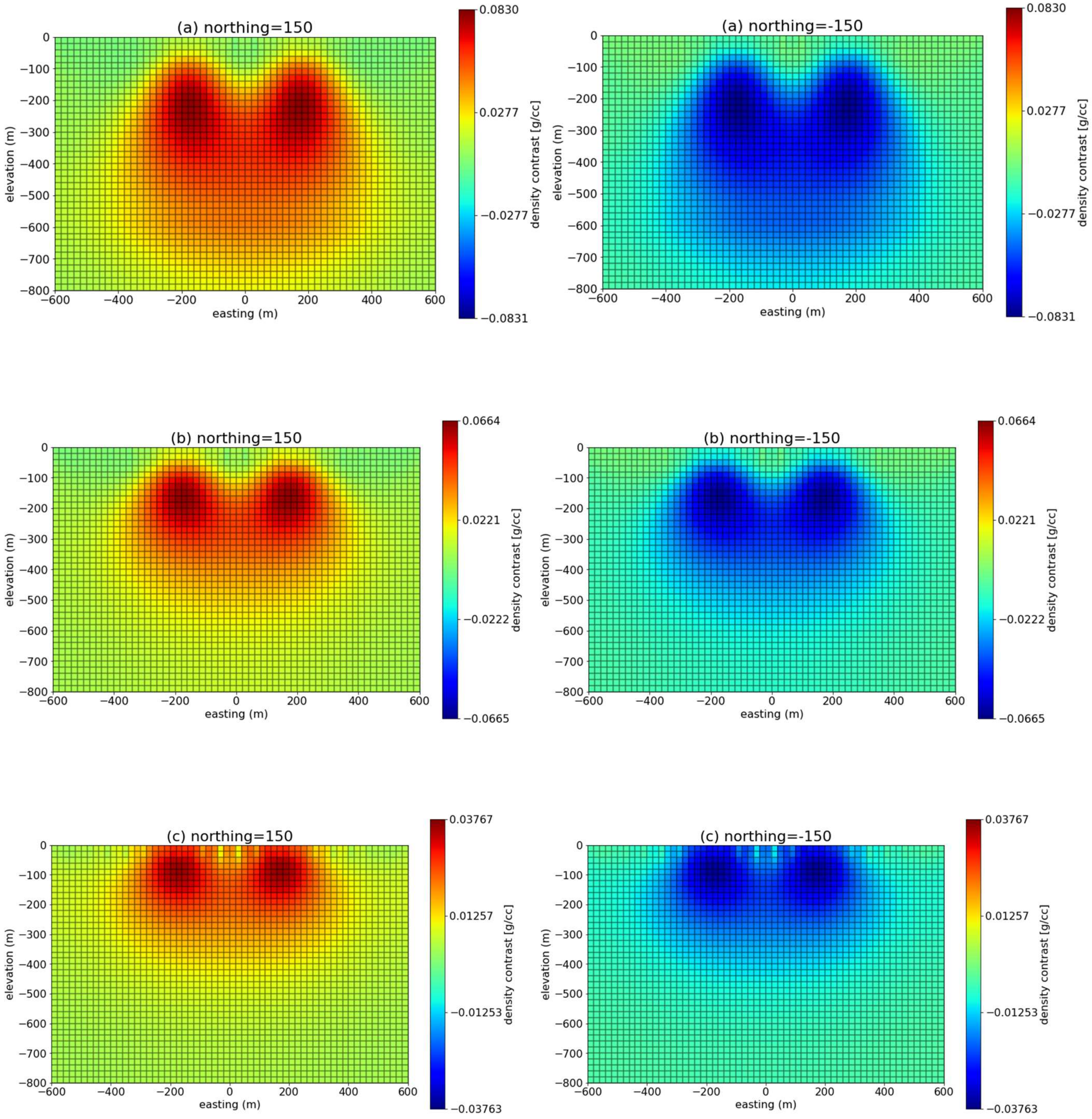

Figure 11: Vertical slice at northing -150 and 150 for the inverted density model from Gzz component inversion of gravity gradient. (a) lambda = 0, (b) lambda = 0.1, (c) lambda = 1

Magnetic Inversion

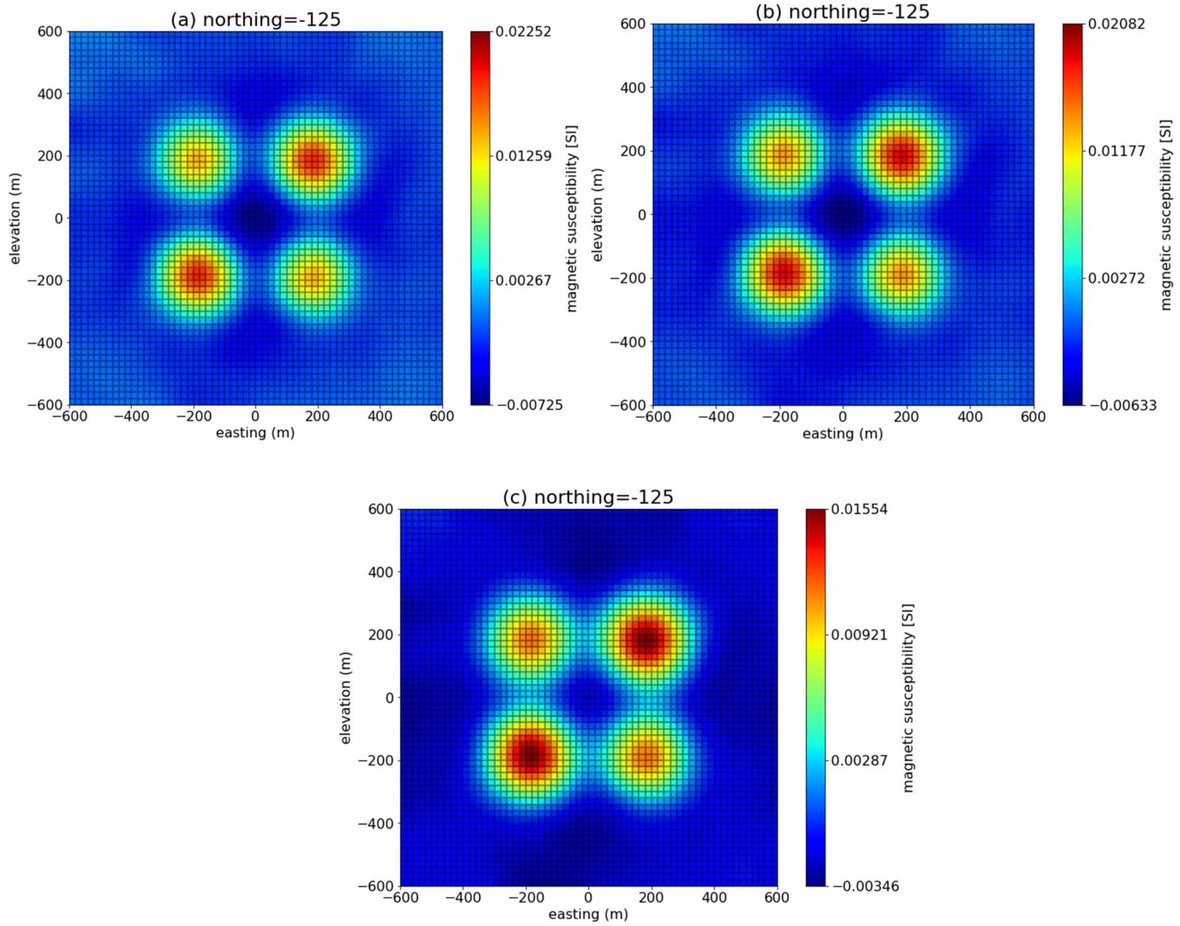

Figure 12: Plan view at -125 meters of elevation for the magnetic inversion. (a) lambda = 0, (b) lambda = 0.1, (c) lambda = 1

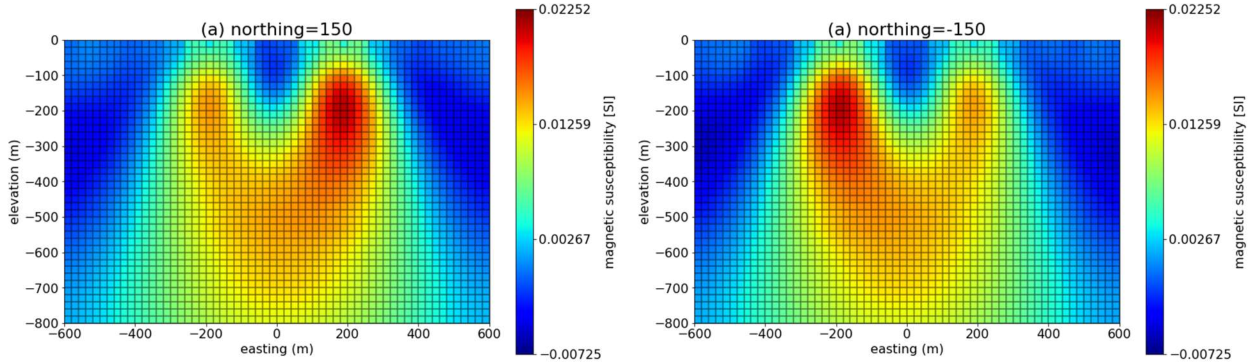

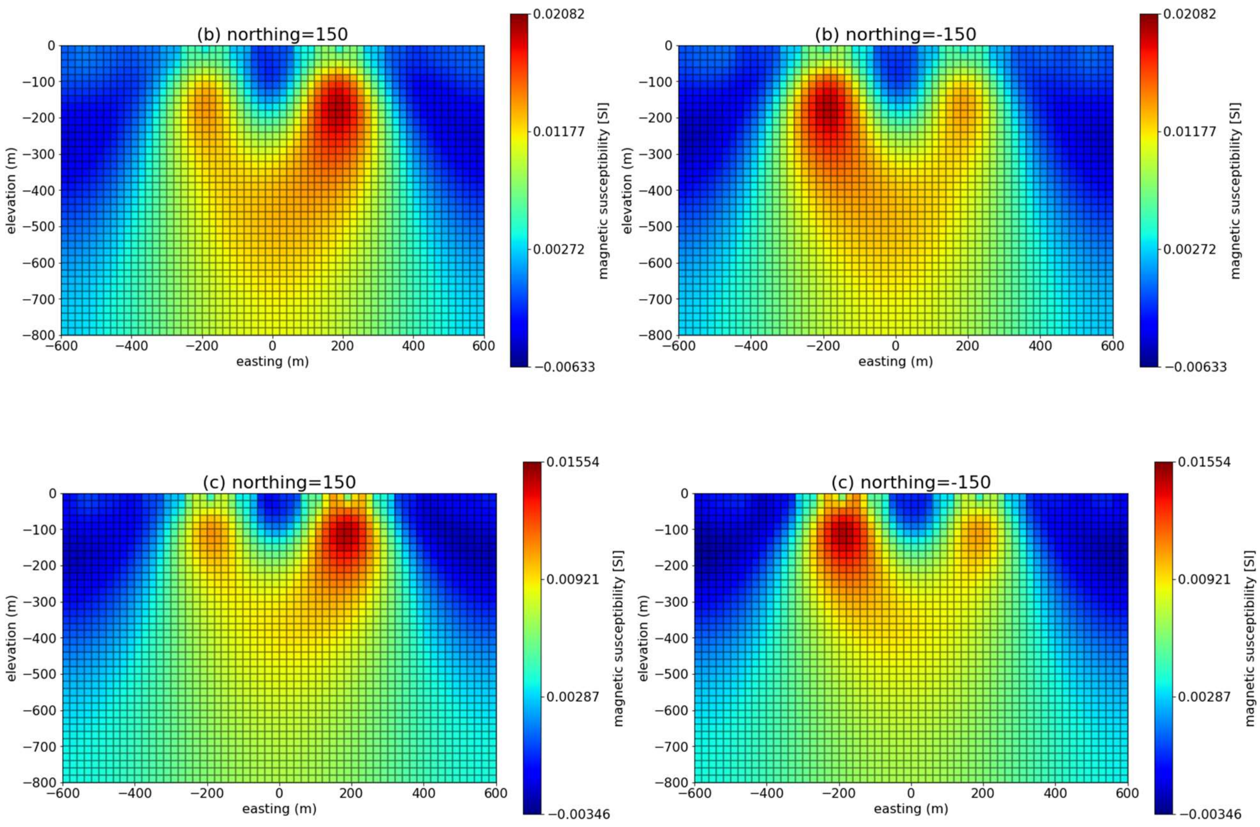

Figure 13: Vertical slice at northing -150 and 150 for the magnetic inversion (a) lambda = 0, (b) lambda = 0.1, (c) lambda = 1

During the testing of different λ values for JTV, an interesting pattern was noted on JTV convergence. The JTV functional is a measure of structural similarity so it should be minimized once the joint objective function is also minimized, such as when the inversion converges at a local minimum. However, I observed that joint inversion would have difficulties minimizing the JTV term unless a sufficiently high λ value was chosen. **Figure 14** is an example of JTV convergence at low λ values, where the JTV term did not minimize but instead increased during subsequent inversion iterations. This behavior would change after reaching a critical λ value as seen in **Figure 15** where the JTV term does minimize after subsequent inversion iterations. It's important to note that the critical λ value varied between different models and datasets, which means several inversions with different λ values must be run to empirically determine this critical value. Additionally, a troubling feature of the JTV coupling term was identified where JTV and the λ regularization parameter would influence the depth weighting of an inverted model. In all synthetic tests, the JTV coupling term would be orders of magnitude larger than terms such as the data misfit in the joint inversion objective function, such as in this synthetic study where the target data misfit was 1600 but the JTV term minimized at about 1.17e6. As the JTV term also acts as a regularization term, increasing the importance of the JTV term by increasing the λ parameter would influence the inverted results. At high λ values, the JTV term seems to counteract the effect of depth weighting and drags the inverted anomalous features upwards and closer the surface. This can be seen in **Figures 11c** and **13c** which contain models overweighted by JTV and are shallower than the true models.

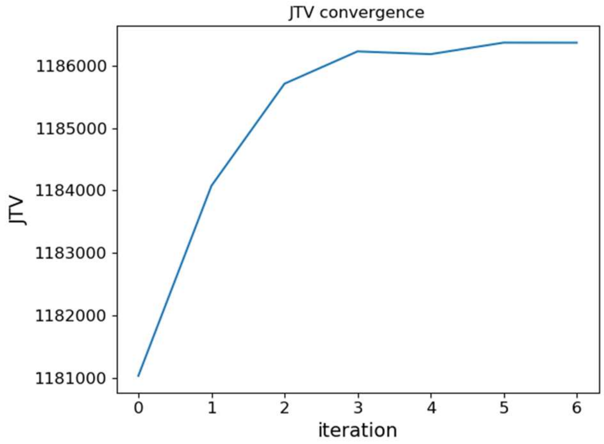

Figure 14: JTV convergence at λ=0.1

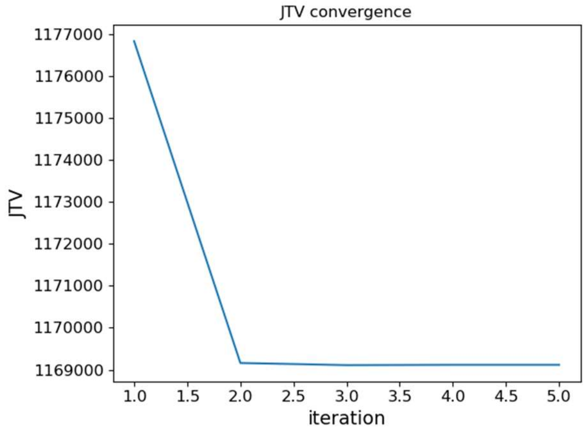

Figure 15: JTV convergence at λ=1 after a critical lambda value

To better observe the effects of JTV coupled joint inversion, crossplots of the inverted density and magnetic susceptibility values were made. These crossplots were compared to **Figure 16**, which shows the crossplot of the density and susceptibility values in the true model.

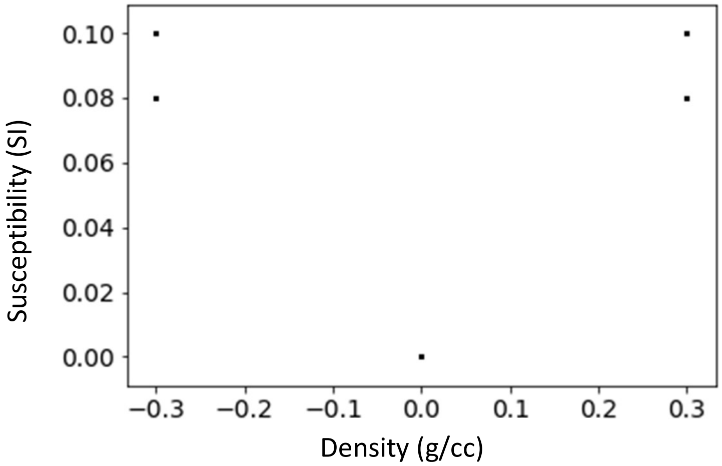

Figure 16: Crossplot of density and magnetic susceptibility values in the true model

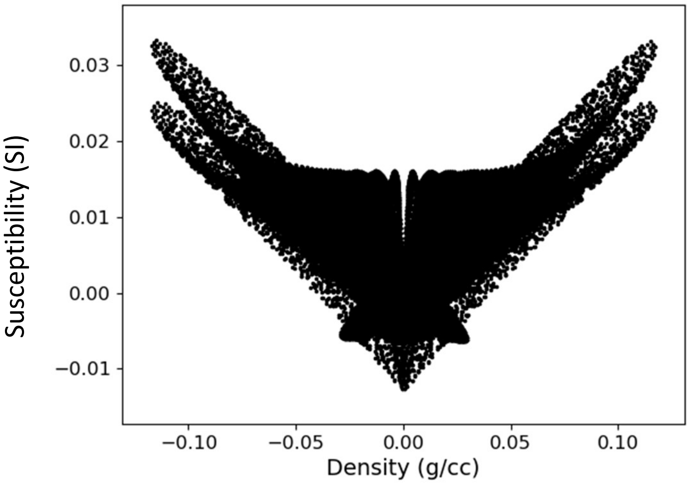

Figure 17: Crossplot of inverted density and magnetic susceptibility values when lambda = 0

Figure 17 shows the crossplot of the inverted property values when $\lambda = 0$ or when the data are separately inveted. Overall, **Figure 17** does have well defined clusters with the upper corners matching the pattern shown in **Figure 16**, although there is some extraneous clustering at the bottom of the figure. The same overall shape is retained in **Figure 18** which also shows a marginally clearer distinction between the clusters at the edge of the figure, while also eliminating the extra clusters present at the bottom of the previous figure. **Figure 19** resembles the previous figures and even shows better value clustering, despite λ negatively influencing the depth weighting of the JTV coupled inversion results. It appears that the shape of the crossplots is not greatly affected by overweighted JTV inversion results, which indicates crossplot analysis is not very beneficial when determining λ weighting.

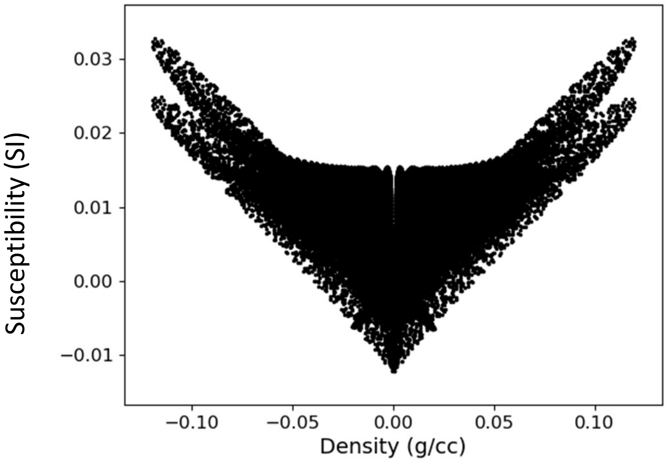

Figure 18: Crossplot of inverted density and magnetic susceptibility values when lambda = 0.1

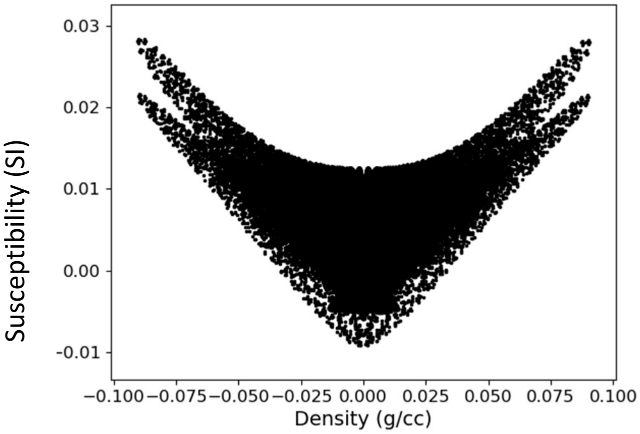

Figure 19: Crossplot of inverted density and magnetic susceptibility values when lambda = 1

Elk Creek Study

Field Data

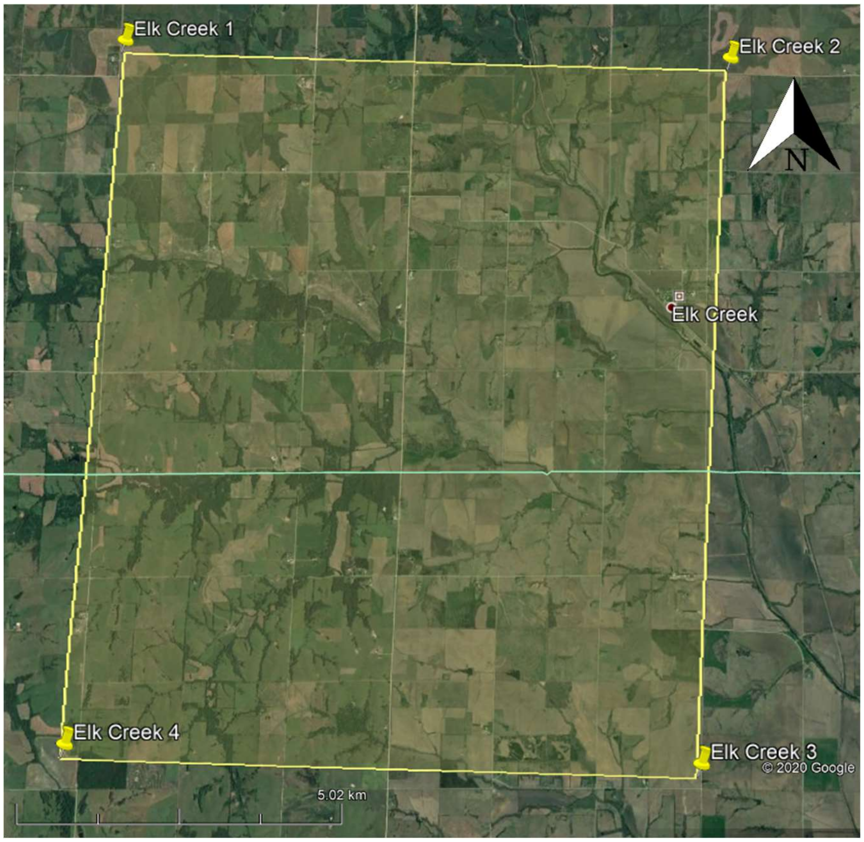

Figure 20: Survey area of Elk Creek, centered on 40º 16'N and 96º 11'W

The 2011 airborne survey of Elk Creek with the Falcon® AGG resulted in over 1176 km of line survey data collected in a region of about 110 km^2 (Fugro Airborne Surveys, 2011). The survey was flown at a nominal terrain clearance of about 100 m with a transverse line spacing of 100 m and tie line spacing of 2,750 m. The gravity gradient data were sampled at a rate of 8 Hz and the magnetic data were sampled at 10 Hz. The gravity gradiometry data provided by the USGS was already pre-processed with the G_{zz} component obtained through equivalent source and Fourier domain methods. Additionally, the provided data were already terrain corrected with a value of 2.67 g/cc. This is shown in **Figure 23**, which shows a large positive density anomaly in the middle of the survey area with a second positive anomaly in the southwest corner. However, the magnetic data required additional processing before it could be used for inversion. The magnetic data is shown in **Figure 21**, which includes visible short wavelength noise from cultural features such as bridges and barn. In addition, there is a regional magnetic trend running through the data that should be removed. **Figure 22** shows the residual magnetic data after trend removal, which retains cultural noise. While both figures show a large magnetic anomaly at the center of the survey area, there are significant changes to some of the anomalies present within the data maps after trend removal. This is particularly clear in the northwest corner of **Figure 22**, which records a negative magnetic anomaly compared to the same location in **Figure 21** which contains a positive magnetic field.

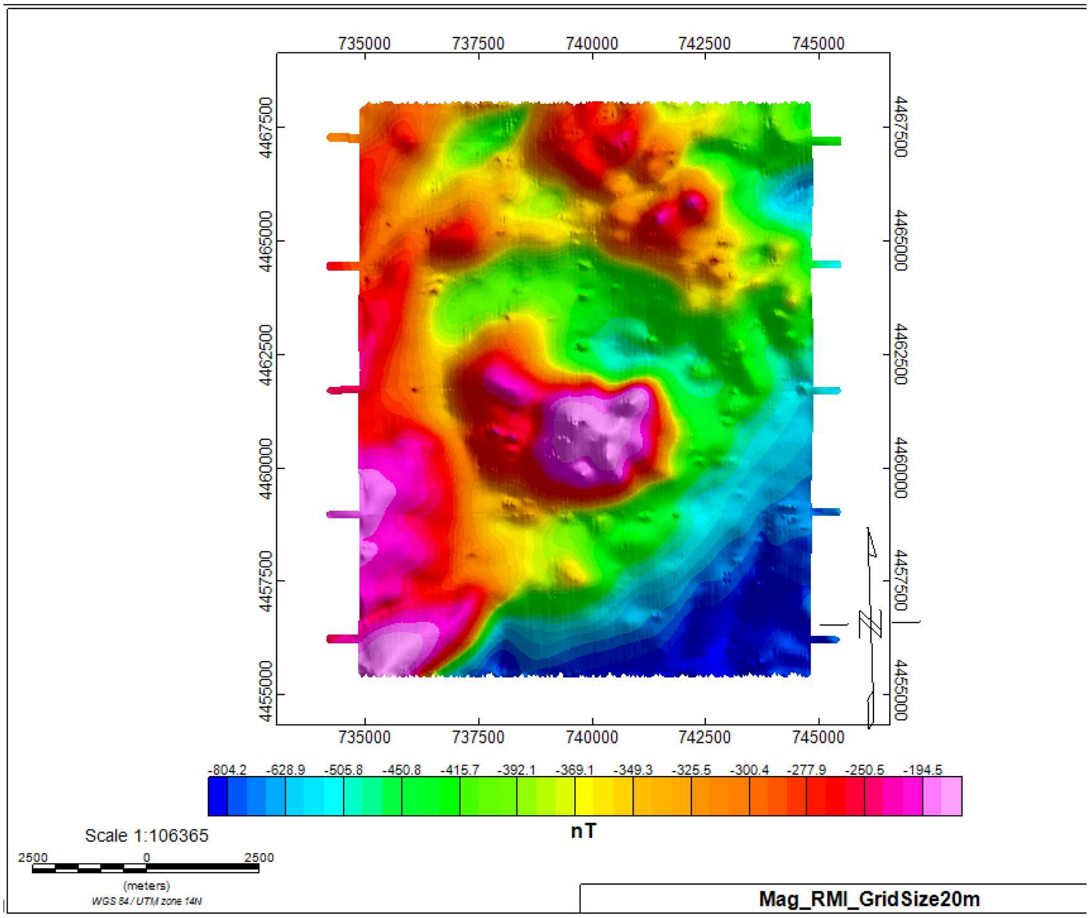

Figure 21: Total field anomaly at Elk Creek. Ambient field inclination and declination are I=68° and D=3°

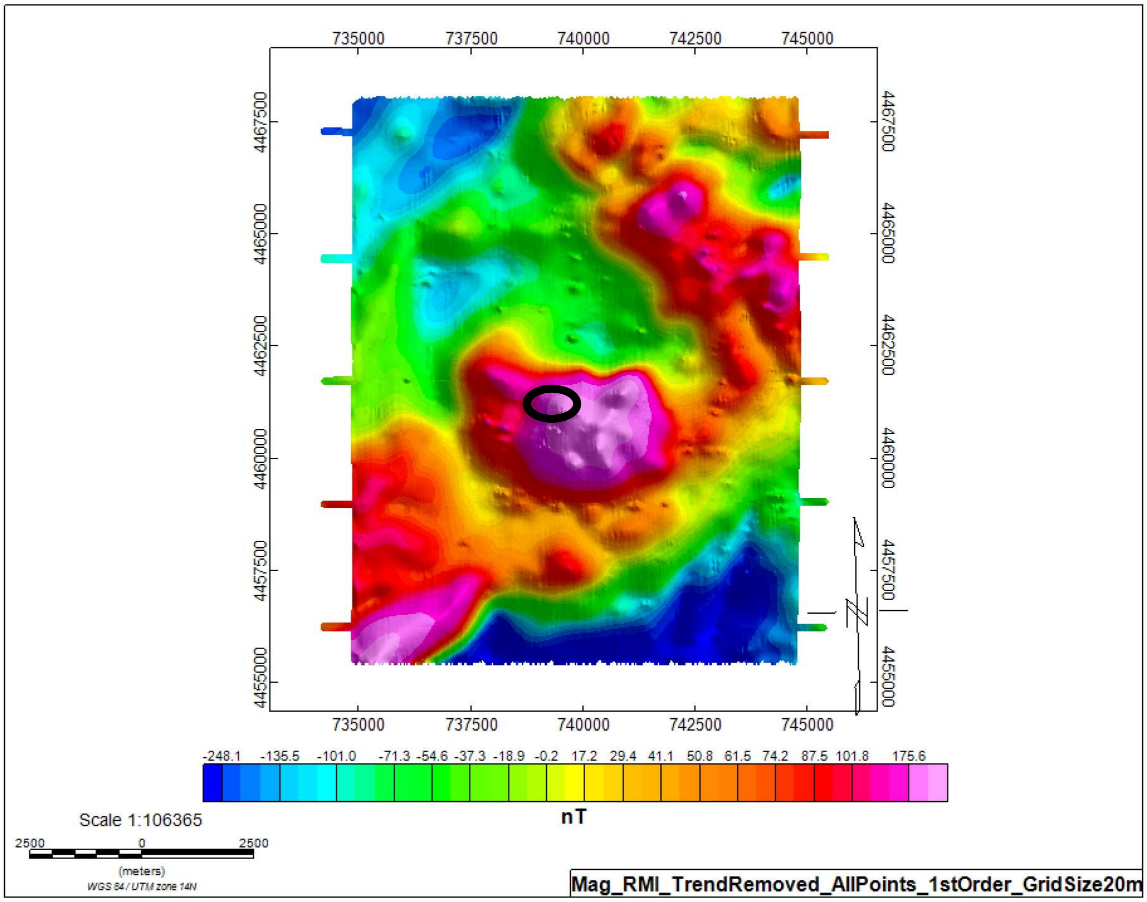

Figure 22: Residual magnetic data with trend removed by Geosoft Oasis Montaj. The black circle indicates the approximate location of the Niobium ore zone

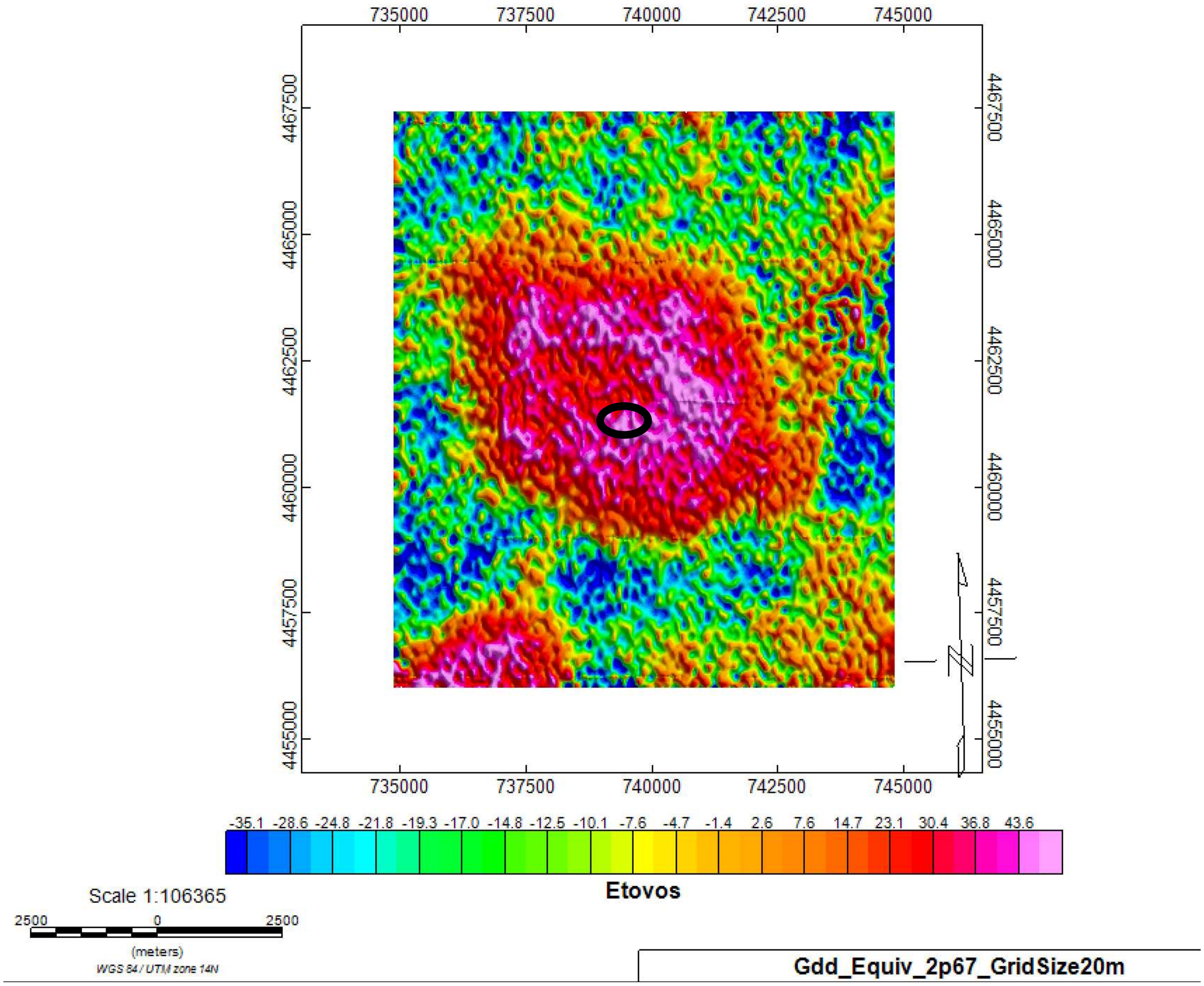

Figure 23: Equivalent source derived Gzz component of the gravity gradient, with terrain correction of 2.67 g/cc. The black circle indicates the approximate location of the Niobium ore zone

The size of the Elk Creek dataset was extremely large, with over 240,000 rows of data in categories including altimetry, gravity gradient component, magnetic field component, and terrain data. Down sampling or data decimation of the dataset was required in order to reduce the computational cost of the inversion. Two approaches to data decimation were considered with one method being simpler than the other. The simpler method involves uniformly decimating the data by a factor N so the remaining data are only the size of the original data set divided by N. The other method involved adaptive sampling of the dataset, with more data removed from quiet regions while preserving signal anomalies (Foks et al., 2014). For this project, the simpler method was chosen as adaptive sampling was unnecessary due to the large wavelength of the signals when compared to the sample size. The magnetic data were measured at a sample distance of about 4 m, while the smallest observable features were larger than 200 m. Due to this, the magnetic data were decimated by a factor of 10 which preserved all observable features. The average difference between the decimated data and the original dataset was only about 1 nT. This is much smaller than the noise level of 20 nT for the magnetic data. The gravity gradient data had a similar sampling rate and was also similarly decimated by a factor of 10. The resulting residuals measured only about 1 Eotvos, which is also smaller than the base noise level of 5 Eotvos.

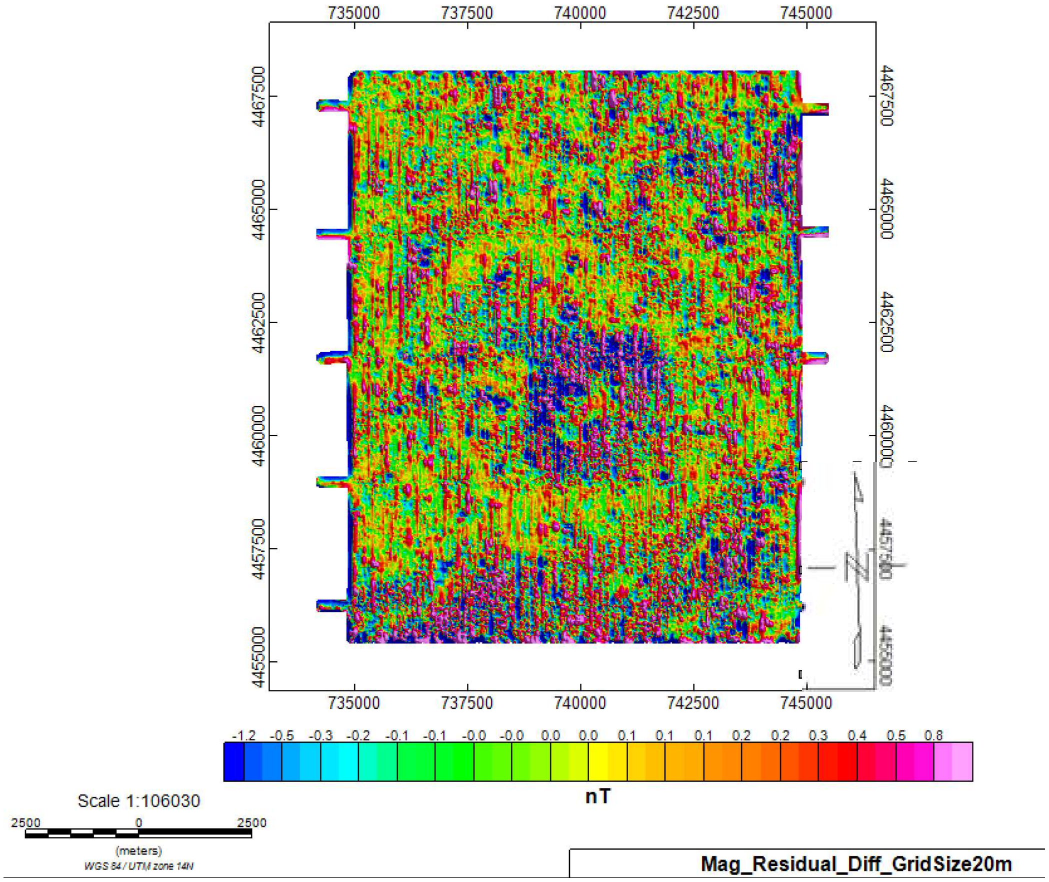

Figure 24: Difference after subtracting residual magnetic data with decimated residual magnetic data

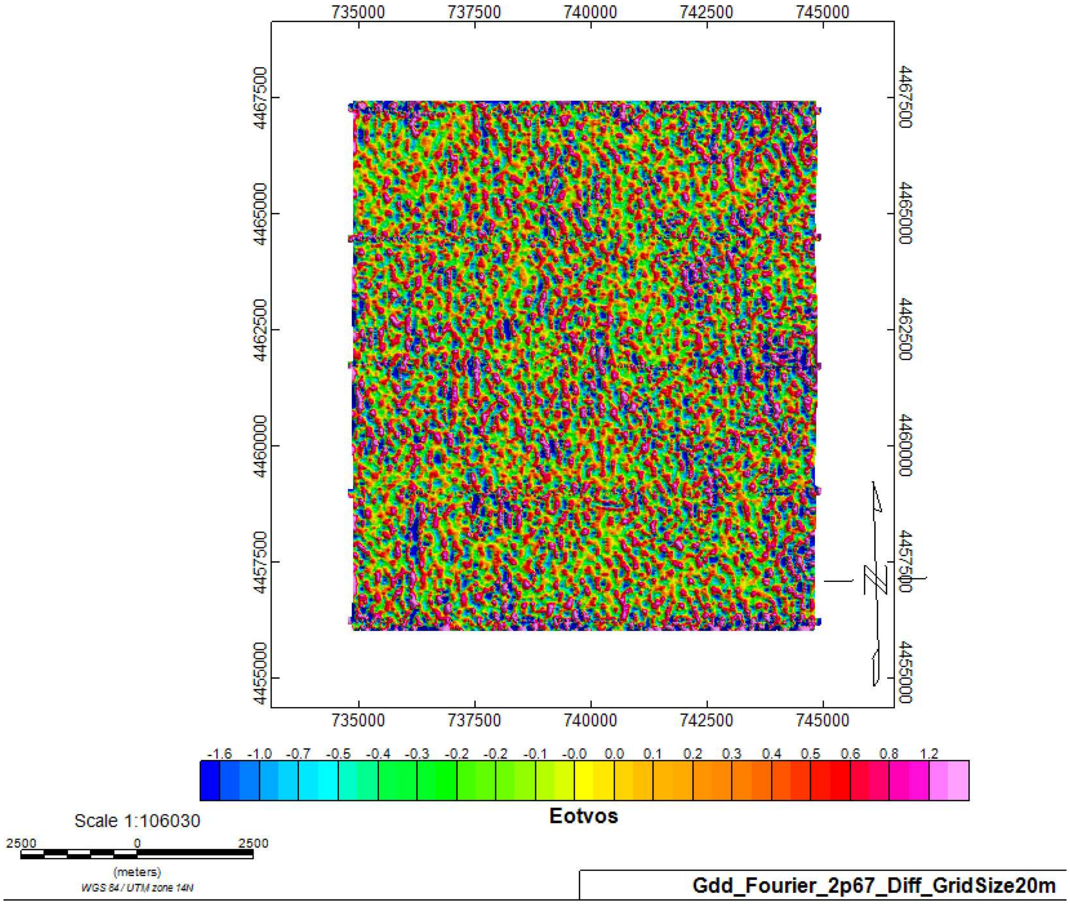

Figure 25: Difference after subtracting Gzz gravity gradient data with decimated Gzz gravity gradient data

Inversion

Interpretation of the airborne geophysical data collected over Elk Creek was performed through 3D inversions to construct 3D density and susceptibility models. The first step was to create a mesh that discretized the survey area. An optimal mesh should contain cells small enough to reproduce the smaller features within the dataset. However, the cells should not be too small; otherwise, an exceedingly large number of unknown parameters need to be inverted for. In the case of the Elk Creek data shown in **Figures 22** and **23**, the smallest meaningful features observed in the data maps were larger than 200 m, so a cell width of 250 m was chosen in order to balance computation cost and feature preservation. In order to cover the survey area which extended 10,000 m and 11,500 m along easting and northing, the created mesh extended 40 cells along easting and 46 cells along northing. In order to minimize edge effects during inversion, 3 padding cells adding up to 1,800 m was added to each edge of the mesh. Determining the number of cells needed to represent inversion depth was more difficult, and required testing of various mesh designs. Eventually, it was determined that 22 cells representing 5,500 m in depth and 6 padding cells extending an additional 3,000 m would be sufficient. Once the mesh was created, the surface topography of the Elk Creek region was also discretized based on a digital terrain model (DTM).

Separate Inversion

A few considerations were made regarding the separate inversion of the Elk Creek data. Borehole data for Elk Creek such as the ones used in Blessington (2014) and Drenth (2014) could have been used to constrain the inversion. However, borehole data were not made available for this study, and only reached maximum depths of about 1,000 m (SRK Consulting, 2015). In comparison, the inversion results show that main features at Elk Creek are located deeper than 1,000 m. It is currently unknown if incorporating borehole measurements would improve the inversion results, and should be fully investigated in the future. For these reasons, my research implemented a zero-initial model for separate inversion. The β weighting parameter used for the separate and later joint inversion was determined through cooling techniques where β started at a high value and was solved with the inverse problem at progressively smaller β values to produce a Tikhonov curve (Parker, 1994). This process ended once β reached a set tolerance value which in this case was 0.1. The inversion environment used the same regularized cell weights and Tikhonov inversion framework as the earlier synthetic study.

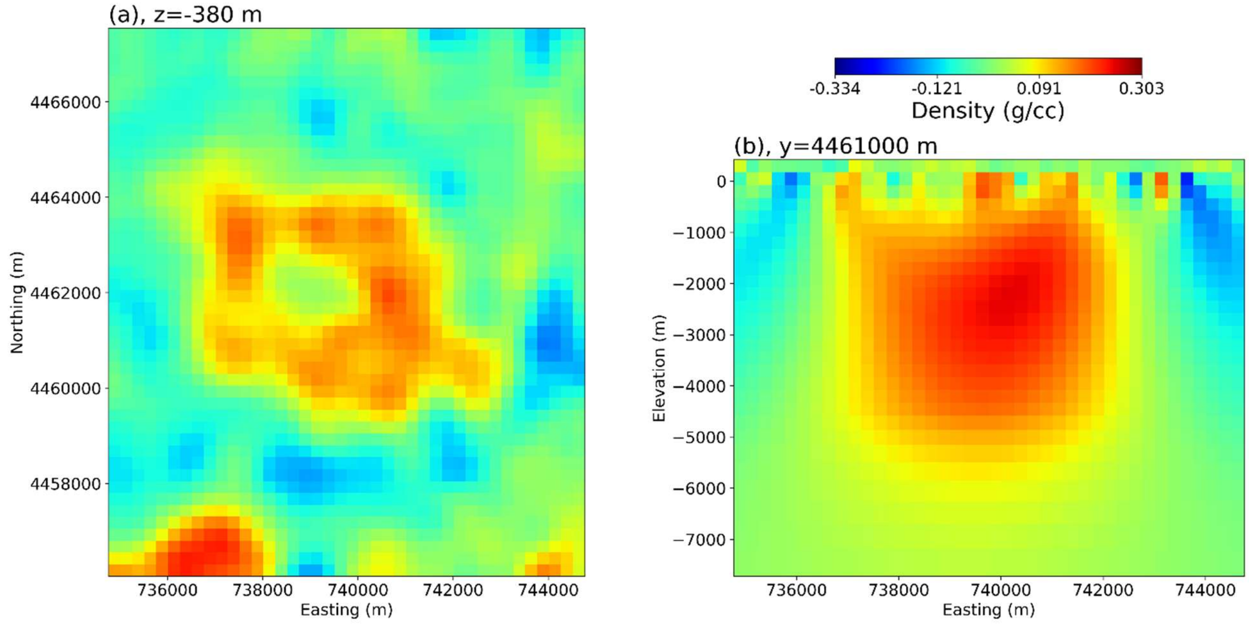

Figure 26: Density model recovered from Gzz component gravity gradient inversion. (a) is the horizontal cross-section obtained at elevation = -380 m while (b) is the vertical cross-section obtained at Northing = 4461000 m

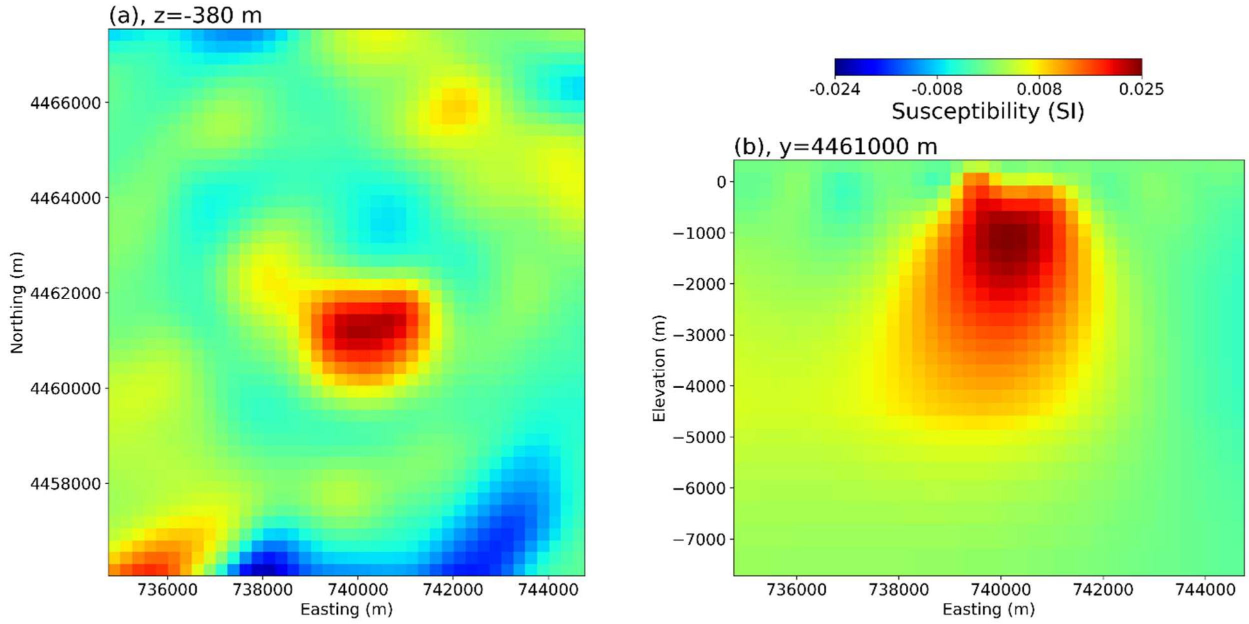

Figure 27: Susceptibility model recovered from TMI magnetic inversion. (a) is the horizontal cross-section obtained at elevation = -380 m while (b) is the vertical cross-section obtained at Northing = 4461000 m

The separate inversion results of the gravity gradient and magnetic data revealed the presence of a positive anomaly at depth near the center of the survey region in **Figures 26** and **27**. The positive density anomaly in **Figure 26a** forms a ring-like shape in the horizontal cross-section, with a zone of near zero density contrast values centered around higher density values. This shape is supported by the vertical cross-section of the density model, which shows the presence of lower density values at shallow depths, before converging into a larger body at deeper depths. Additionally, the inverted density model revealed that the densest part of the anomaly is located between 1-4 km at depth around 740 km Easting. In the inverted susceptibility model, the anomalous magnetic body is significantly smaller than the density anomaly in both cross-sections. **Figure 27b** model also reveals a highly magnetized region between 1-2 km at depth.

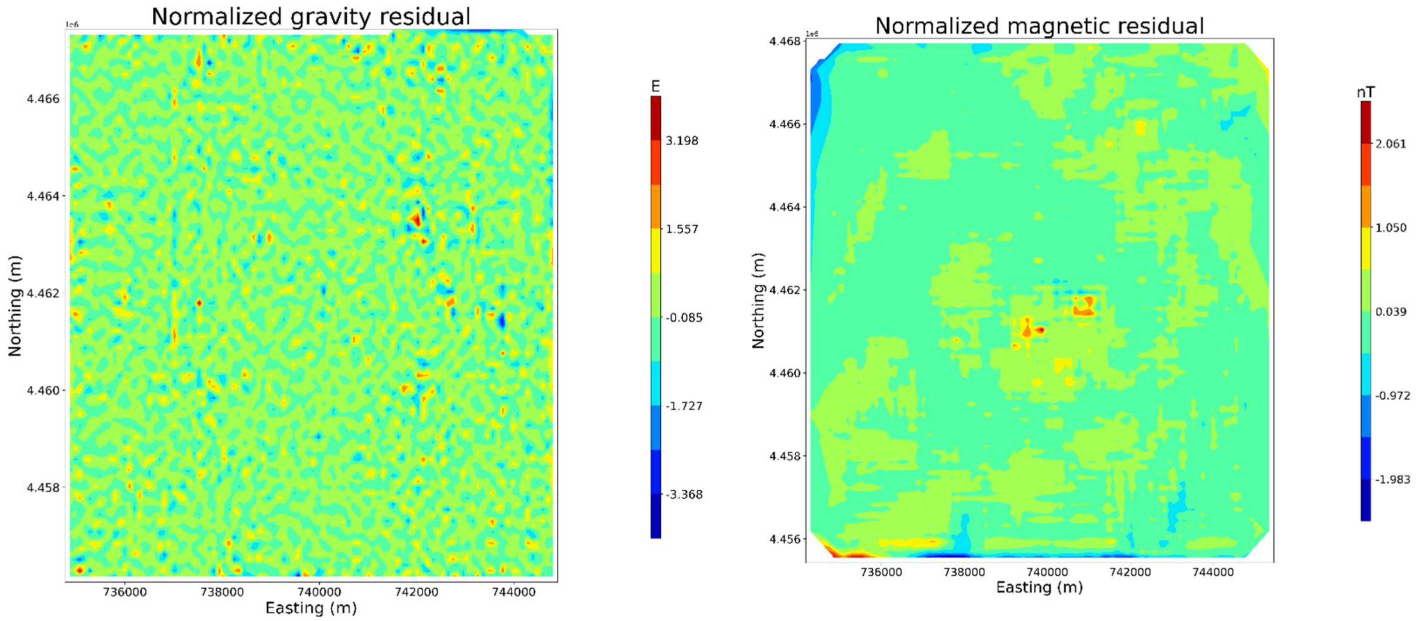

Figure 28: Normalized data residuals from the separate gravity gradient and magnetic inversion

A crossplot of the inverted density and susceptibility contrast values was created from the separate inversions, in order to analyze possible lithology groupings through clustered physical property values. A preliminary examination of **Figure 29** revealed six zones of strongly clustered values, which were circled in red ellipses. These zones were visually identified based on their unique shapes at the corners of the crossplot along with the density of the values at these locations. At this point, the identification of these clusters was somewhat arbitrary as it was done based primarily on visual observations. These preliminary differentiations would be refined later on during geology differentiation where the boundaries between each cluster would be quantitatively tested and compared to known geological information. However, even these preliminarily chosen clusters of correlated values still shared features with the inverted physical property models. For example, the highest inverted density values plotted in **Figure 29** only occur next to high positive susceptibility values. These observations correspond to the locations of the highest positive values in the inverted physical property models, as both the density and magnetic susceptibility models contain peak values at about 740,500 m easting and -2000 m elevation in **Figures 26b** and **27b**. Each zone of correlated density and susceptibility values likely indicates a unique lithologic unit (Li et al. 2019).

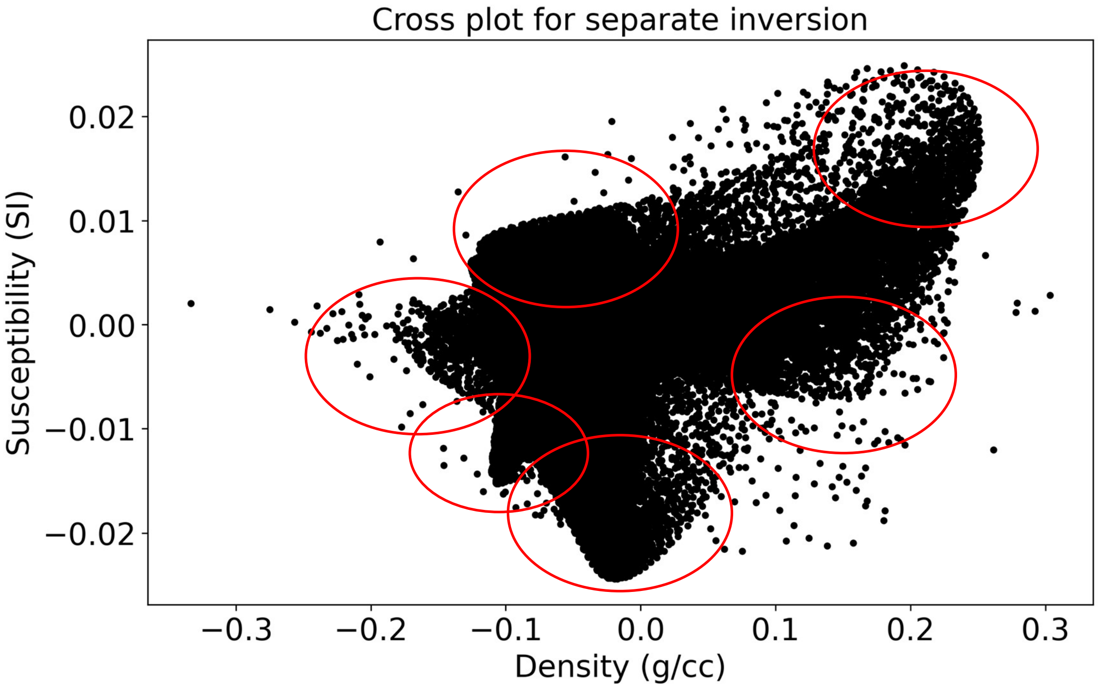

Figure 29: Crossplot of density and susceptibility contrast values from separate inversion of the Elk Creek dataset. The red ellipses indicate zones of clustered values

An important observation from the inverted susceptibility model and the crossplot above is the presence of negative susceptibility values. Negative inverted susceptibility values indicate the presence of magnetized rocks which point in the opposite direction of the inducing field, which in this case is the current location of the Earth's magnetic field. While negative magnetic susceptibility values naturally occur in diamagnetic materials such as quartz, this induced magnetization is extremely weak compared to remanent magnetization in ferromagnetic materials which can record the direction of a previous inducing field (Butler, 1992). The presence of iron-rich lithology at Elk Creek such as mafic rocks and magnetite-dolomite carbonatite implies the presence of remanent magnetization should be expected, which is reflected in the inverted results. However, no information is available on magnetic remanence at Elk Creek and some remanence in the magnetite-dolomite carbonatite or mafic rocks may align in the direction of the modern Earth's magnetic field (Drenth, 2014). Additionally, the igneous rocks within the Precambrian basement surrounding Elk Creek are associated with the Midcontinent Rift System which are well known to contain intense remanent magnetization (Hinze & Chandler, 2020).

Joint Total Variation Inversion

After completing the separate inversions, an attempt was made to jointly invert the Elk Creek data using JTV. In order to reduce computation cost, the density and magnetic susceptibility models produced by separate inversion were used as initial models for the joint inversion. In the process of performing joint inversion on real data, a severe problem with the JTV coupling term emerged. During earlier synthetic tests, a concerning pattern with using JTV was identified where the JTV coupling term would influence the depth weighting of an inverted model. When JTV was applied to the joint inversion of the Elk Creek data, the resulting inversion did not minimize the coupling term and significantly affected the depth weighting of the inverted models.

As stated previously, the minimization of the JTV coupling term is reliant on the λ regularization parameter. In order to represent the results from JTV joint inversion, **Figures 30** and **31** were produced from $\lambda = 0.02$, which did not minimize the JTV term but showed affected depth weightings when compared to the results from separate inversion. **Figure 30b** shows the dramatic influence of the JTV coupling term on the jointly inverted density model, where the depth extent of the positive anomaly is much shallower than in the single inversion. The density contrast values in **Figure 30b** were also significantly reduced compared to the separate inversion results, with a maximum value of 0.187 g/cc while the previous model had a maximum value of 0.303 g/cc. Additionally, many features of the jointly inverted density model have been smoothed out as shown in both cross-sections. Attempting to minimize the JTV coupling term with greater λ values would exacerbate the issues seen in the density model. The susceptibility model in comparison was much less affected by the JTV coupling term, with **Figures 27** and **31** appearing almost identical. The crossplot of the recovered density and susceptibility values from the joint total variation inversion is shown in **Figure 32**. The distribution of the inverted values (i.e., the black dots in the crossplot) is largely the same as in **Figure 29**. The results from the real data JTV inversion closely reflect the results from the preliminary study using synthetic data, with unstable depth recovery due to the influence of the weighting parameter λ on the JTV coupling term. Due to these results, I chose to implement cross-gradient joint inversion and use the inversion results for the subsequent work in geology differentiation.

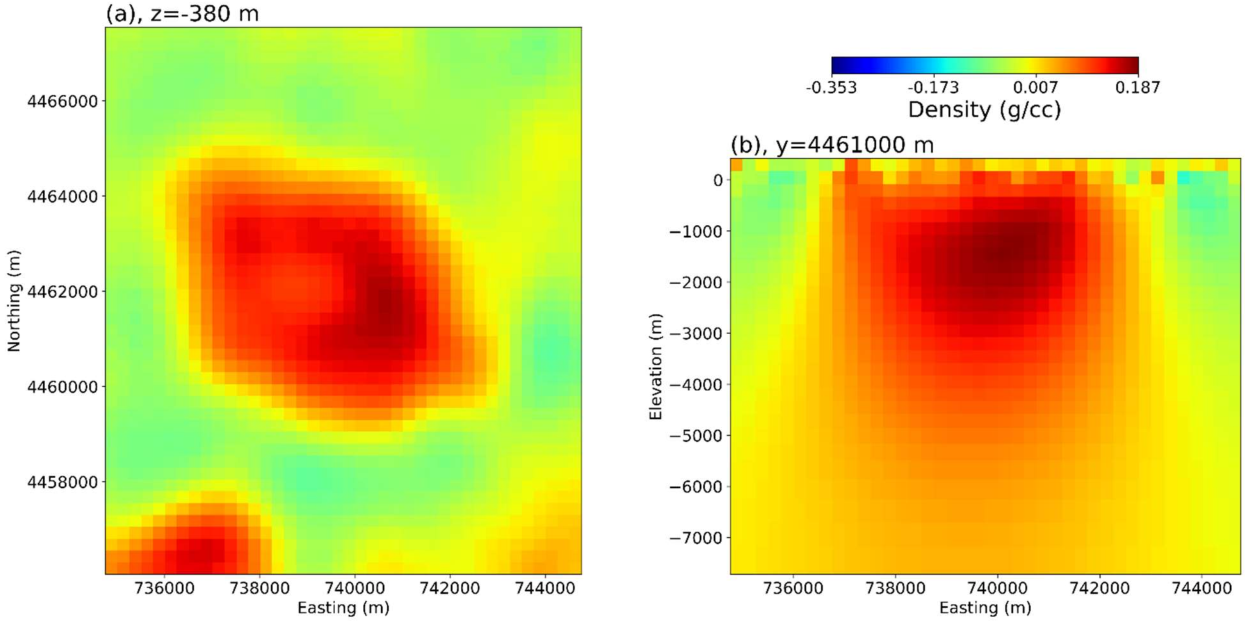

Figure 30: Joint total variation joint inversion results from Gzz component gravity gradient inversion. (a) is the horizontal cross-section obtained at elevation = -380 m while (b) is the vertical cross-section obtained at Northing = 4461000 m

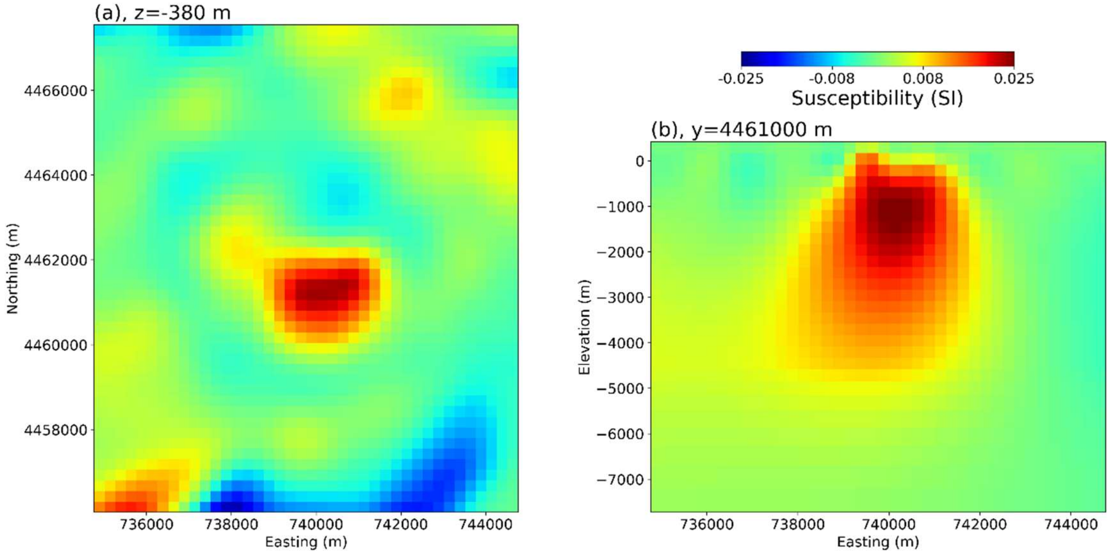

Figure 31: Joint total variation joint inversion results from TMI magnetic inversion. (a) is the horizontal cross-section obtained at elevation = -380 m while (b) is the vertical cross-section obtained at Northing = 4461000 m

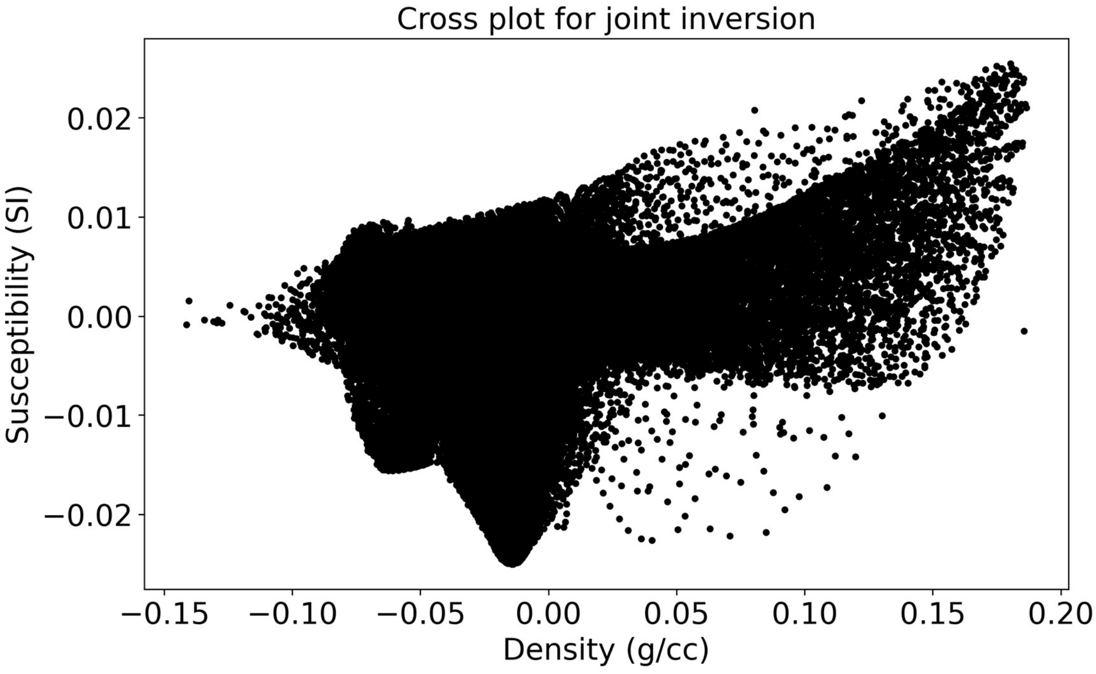

Figure 32: Crossplot of the joint total variation joint inversion

Joint Cross-Gradient Inversion

The rest of this study used the cross-gradient for 3D joint inversion of the Elk Creek dataset and for geology differentiation. Kim et al. (2020) implemented cross-gradient joint inversion in SimPEG, and

I used the same code for my work on Elk Creek. Therefore, switching to the cross-gradient in SimPEG was a relatively simple process, as the underlying inversion framework remained the same. The only difference in implementation was the code regarding the coupling term itself, which was swapped from JTV to the cross-gradient. As stated previously, the cross-gradient term is also associated with the weighting parameter λ which determines the influence of the coupling term on the final inverted models. However, it is important to note that the possible range of λ values for cross-gradient joint inversion differ greatly from JTV due to differences between the coupling terms. Another important note is that the cross-gradient term is non-convex, so local minima during inversion are possible. A variety of different λ values were tested, with the best inversion results from $\lambda = 1e18$.

The jointly inverted density and susceptibility models are shown in **Figure 33** and **34**. Comparing **Figure 26a** and **33a** reveals the joint inversion significantly enhanced the signature of negative anomalies surrounding the carbonatite complex. The cross-gradient joint inversion also increased the structural similarity between the density and magnetic susceptibility values. The region enclosed in the black oval in **Figures 33a** and **34a** shows significantly better structural similarity. The same improvement can also be seen at the top right of the positive anomaly in **Figure 33b**, which now better resembles **Figure 34b**.

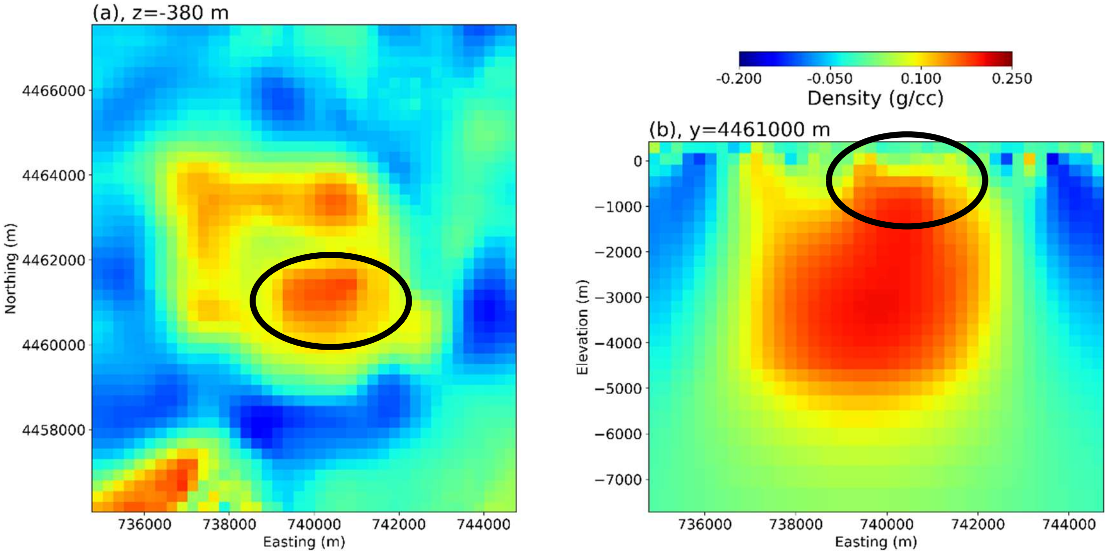

Figure 33: Cross-gradient joint inversion results from Gzz component gravity gradient inversion. (a) is the horizontal cross-section obtained at elevation = -380 m while (b) is the vertical cross-section obtained at Northing = 4461000 m. The black oval indicates regions of improved structural similarity

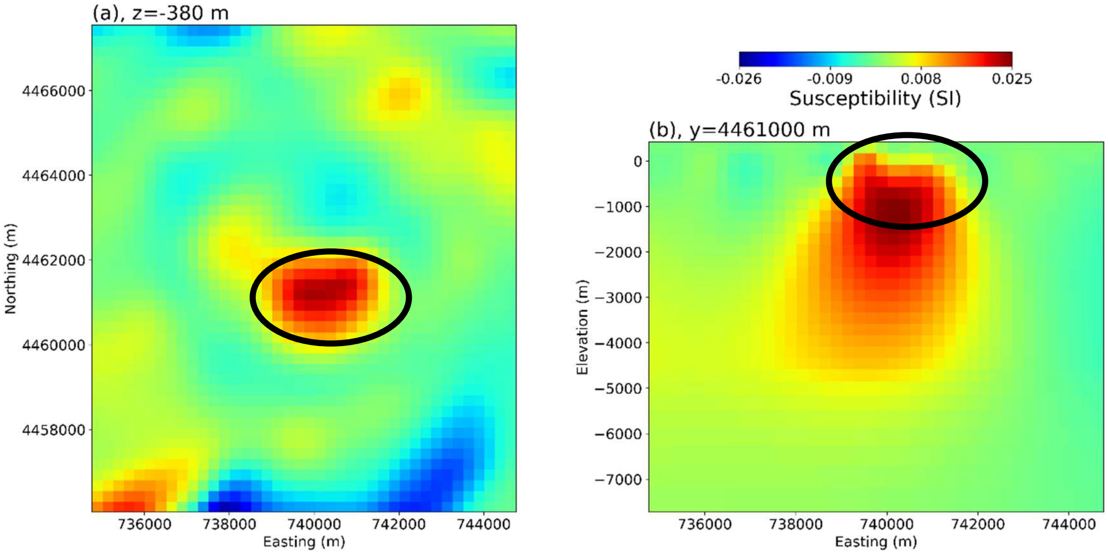

Figure 34: Cross-gradient joint inversion results from TMI magnetic inversion. (a) is the horizontal cross-section obtained at elevation = -380 m while (b) is the vertical cross-section obtained at Northing = 4461000 m. The black oval indicates regions of structural similarity improved structural similarity

After the cross-gradient joint inversion was completed, a crossplot of the density and susceptibility values was created (**Figure 35**). A visual comparison of this crossplot to **Figure 29** shows tighter value clustering within the areas enclosed within the red ellipses. The tighter clustering along with the reduction of dispersed and outlier values outside of identified clusters within **Figure 35** allow for clearer identification of the boundaries between nearby clusters. One example of this is in bottom region of the crossplot between -0.1 and 0.0 g/cc and -0.01 and -0.02 SI which is now clearly defined as two distinct clusters in **Figure 35**. The improved crossplot from cross-gradient joint inversion indicates that the cross-gradient term improved the overall structural similarity between both models, and more importantly, produced better defined grouping or clustering features that allow for easier and potentially more reliable work in the subsequent geology differentiation.

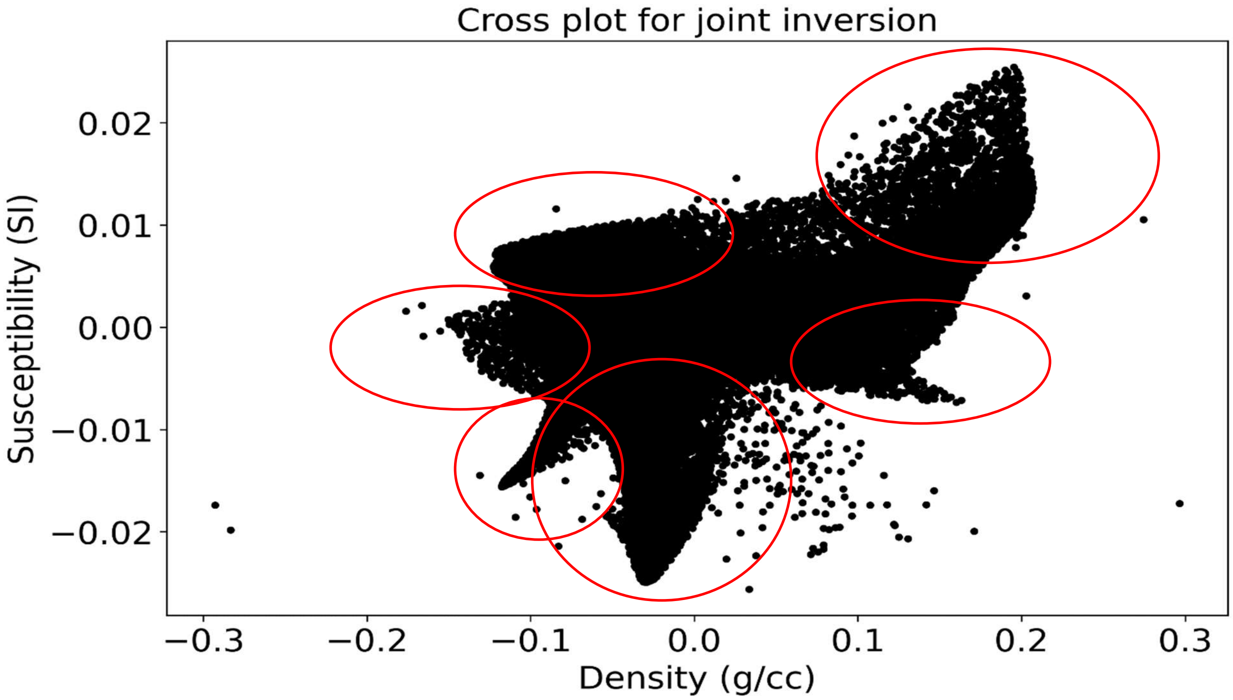

Figure 35: Crossplot of the recovered density and susceptibility values from the cross-gradient joint inversion. The red ellipses indicate zones of clustered values

Geology Differentiation

The goal of geology differentiation is the creation of a quasi-geology model representing the subsurface with classified lithologic units based on inverted physical property values and known geological observations. These geological observations include known geology, borehole data, physical property measurements, etc. For this study, these observations consisted mostly of physical properties recorded from core samples of Elk Creek in Drenth (2014) and geological analysis of core samples in

Blessington (2014). These geological observations were analyzed in order to find patterns within the physical property values which corresponded to distinct geological units.

From these previous observations, the lithology was grouped into six categories: (1) country rock, (2) undifferentiated carbonatites and syenite, (3) mafic rocks, (4), lamprophyre, (5) dolomite carbonatite breccias, (6) magnetite-dolomite carbonatite. These groupings are very similar to the ones described in Kass et al. (2015), although the lamprophyre was separated from the other mafic rocks and the dolomite carbonatite breccias were separated from the undifferentiated carbonatites. The lamprophyre was separated from the other mafic rocks as observations from Blessington (2014) noted the lamprophyre was not magnetized, which contrasts with the other mafic rocks which have high magnetic susceptibility when unaltered. Borehole logs and hand sample measurements of the magnetic susceptibility of the lamprophyre were not available for this study. Consequently, the lamprophyre was separated from the other mafic rocks out of precaution. However, physical property values of the dolomite carbonatite breccias at Elk Creek was recorded in Drenth (2014), with a wide range of possible magnetic susceptibility and density values. Additionally, dolomite carbonatite breccias at Elk Creek can occur as a transition boundary from magnetite-dolomite carbonatite (Blessington, 2014). In these transition zones, the matrix and clasts of the breccia may be composed of either magnetite-dolomite carbonatite or dolomite-carbonatite (Blessington, 2014). The density and magnetic susceptibility of the dolomite-carbonatite breccia will vary depending on the amount of contained magnetite-dolomite carbonatite, resulting in the separation of the dolomite carbonatite breccias from the undifferentiated carbonatites.

As a summary of the six groupings above, the following physical property patterns are expected at Elk Creek. The country rocks (1) are expected to be the least dense units at Elk Creek and on average moderately magnetized. The undifferentiated carbonatites and syenite (2) are denser than the country rocks and weakly magnetized. The undifferentiated mafic rocks (3) are expected to be slightly denser than the country rock but not as dense as the undifferentiated carbonatites with strong magnetization. The lamprophyre (4) in comparison should share similar densities to the other mafic rocks but have lower magnetization. The magnetite-dolomite carbonatite (5) is still expected to be the densest and most magnetized unit at Elk Creek, although the dolomite carbonatite breccias (6) can cover a wide range of possible density and magnetic susceptibility values in between the undifferentiated carbonatites and the magnetite-dolomite carbonatite. These groupings were used to create a theoretical crossplot of the lithology at Elk Creek (**Figure 36**).

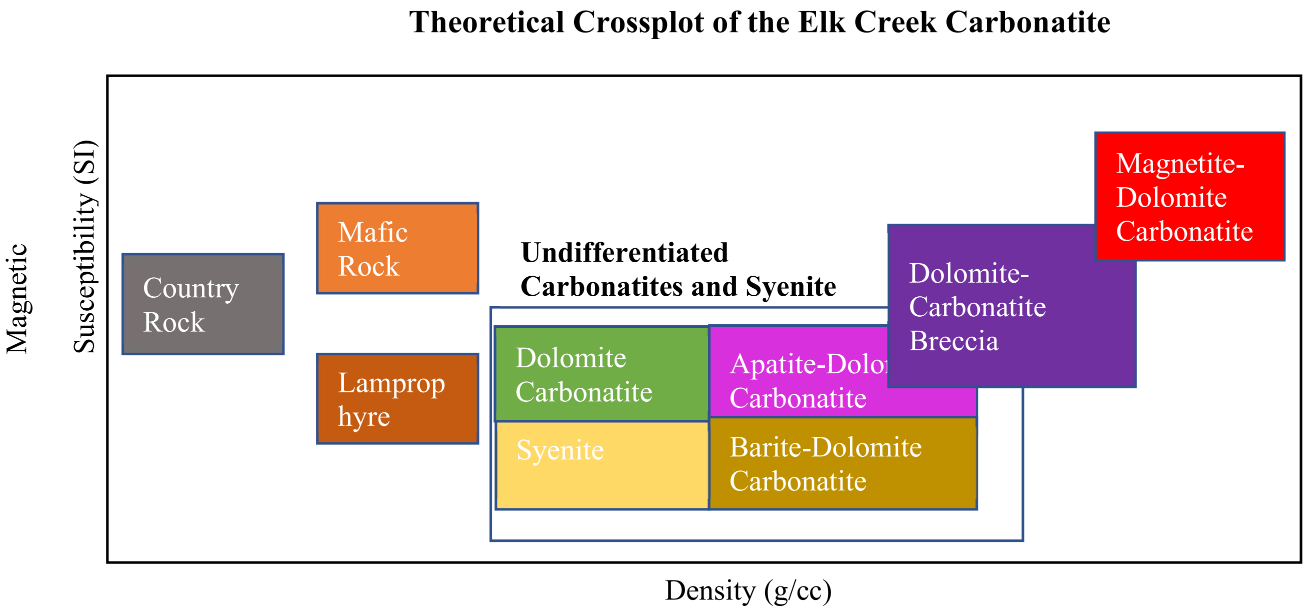

Figure 36: Theoretical crossplot of the lithologic units at shallow depths within the Elk Creek Carbonatite

It is important to note that the theoretical crossplot above used data from existing boreholes with most reaching less than 1,000 m in depth, while the inverted models produced in this thesis reach down to 7,000 m. Additionally, Drenth (2014) only provided data on the geologic units immediately within and surrounding the main carbonatite complex. Information about the lithological units deeper than 1,000 m along with borehole data from outside the main carbonatite deposit were not available. Another important note is that the direction of any remanent field is not noted in the theoretical crossplot, but is expected within the lithology at Elk Creek (Kass et al., 2015). Therefore, this theoretical crossplot should be primarily used as a guidance for subsequent classification of the inverted values within **Figure 35**. The final classification of the inverted values might look different than those in the theoretical crossplot.

After a thorough analysis of the known physical property patterns within the sampled regions of the Elk Creek carbonatite, this information was applied to the jointly inverted physical property models and crossplot to classify unique geologic units. For my study, a guiding principle was that the differentiated geology should match the inverted features present within the inverted density and susceptibility models. In order to do this, I first started with plotting the locations of clusters identified in **Figure 35** back into the same 3D spatial domain as the inverted models to observe the spatial extent of each individual cluster. The boundaries in between each cluster were determined through a long process of experimental testing. This involved plotting small groups of physical property values close to the outer edges of the individual crossplot clusters in the 3D spatial domain. These small boundary groups were assigned to a previously defined cluster after careful analysis of the spatial extent of these boundary groups and which clusters they matched better with. However, some coincident crossplot clusters also shared coincident boundaries in spatial domain leading to some degree of uncertainty regarding the boundaries of these groupings. A similar process was followed in identifying lithologic unit groupings of regions outside the clusters in **Figure 35**, where small groups of values were tested before expanding these groupings based on known patterns with the physical properties at Elk Creek and analysis of whether the grouped values were spatially correlated.

Figure 37 depicts the crossplot after all the inverted density and susceptibility values were differentiated as geologic units. The differentiation of the geologic units was based on the geological observations summarized in the theoretical crossplot. Not all of the identified units could be assigned the names of known lithology as there are still many uncertainties in regards to the geology at Elk Creek. Instead, the remaining geologic units were characterized according to correlations within the inverted physical properties. The following section lists the classified units at Elk Creek and explains the reasoning behind the classifications.

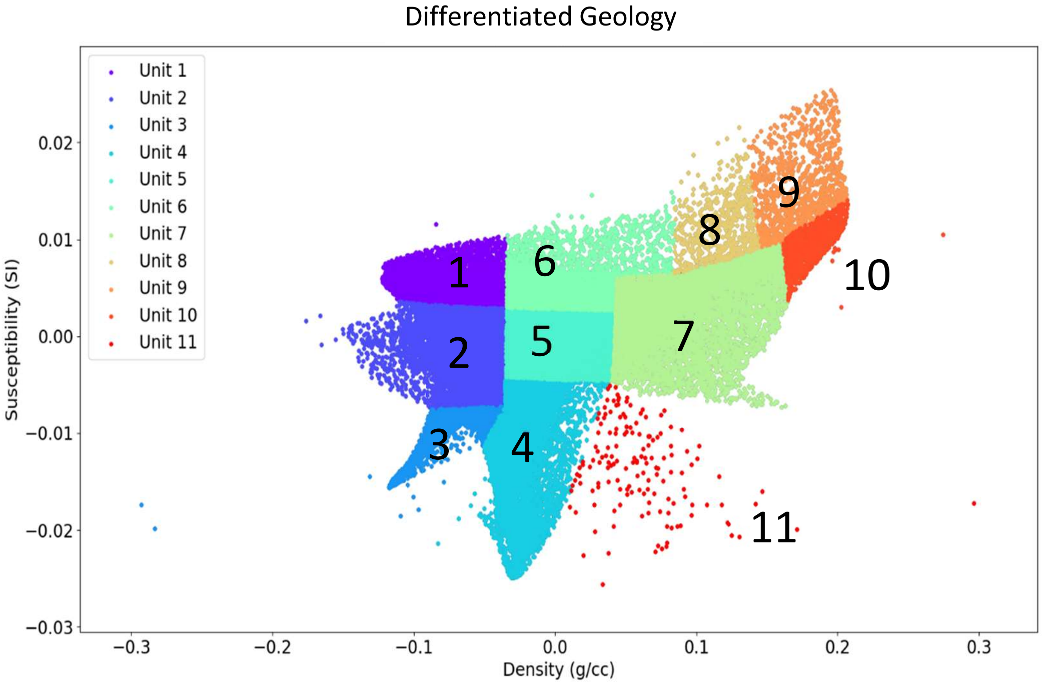

Figure 37: Crossplot with the 11 identified geologic units from geology differentiation. The units are all color coded with the legend on the top left. As many units could not be assigned names based on lithology, these units are instead referred to by number. The units which could be identified are units 5 (the country rock), 6 (mafic rock), 7 (undifferentiated carbonatites) and 8 (magnetite-dolomite carbonatite)

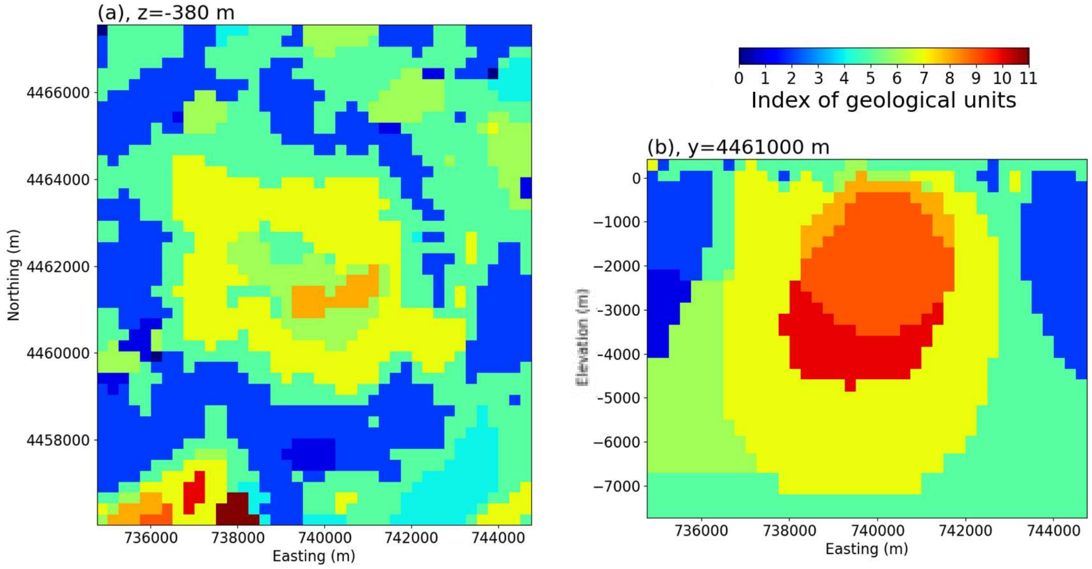

Figure 38: Cross-section of the 11 identified geologic units

<u>Units 1 and 2</u>

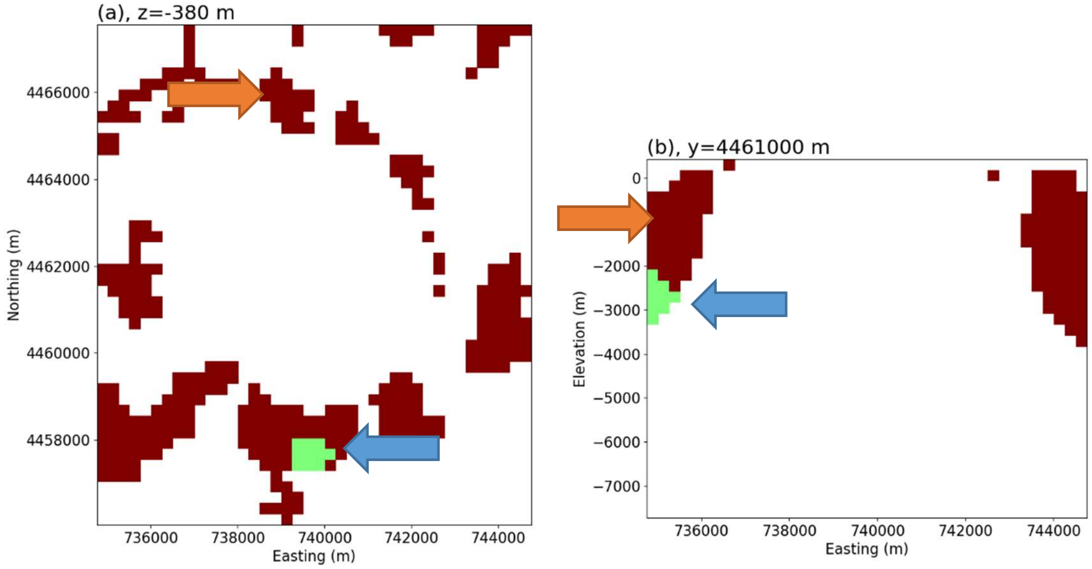

Figure 39: Cross-section view of units 1 and 2. (a) is the horizontal cross-section obtained at elevation = -380 m while (b) is the vertical cross-section obtained at Northing = 4461000 m. Unit 1 is green while unit 2 is red. The orange arrows indicate correlated features with the inverted density model while the blue arrows indicate correlated features with the inverted susceptibility model.

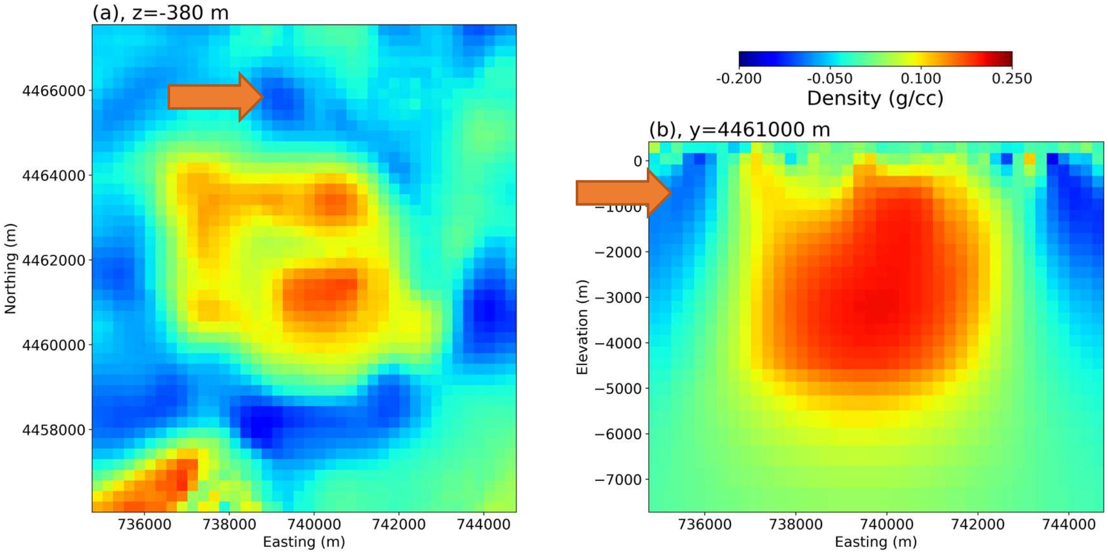

Figure 40: Jointly inverted density model. (a) is the horizontal cross-section obtained at elevation = -380 m while (b) is the vertical cross-section obtained at Northing = 4461000 m. The orange arrows indicate regions of low density associated with units 1 and 2

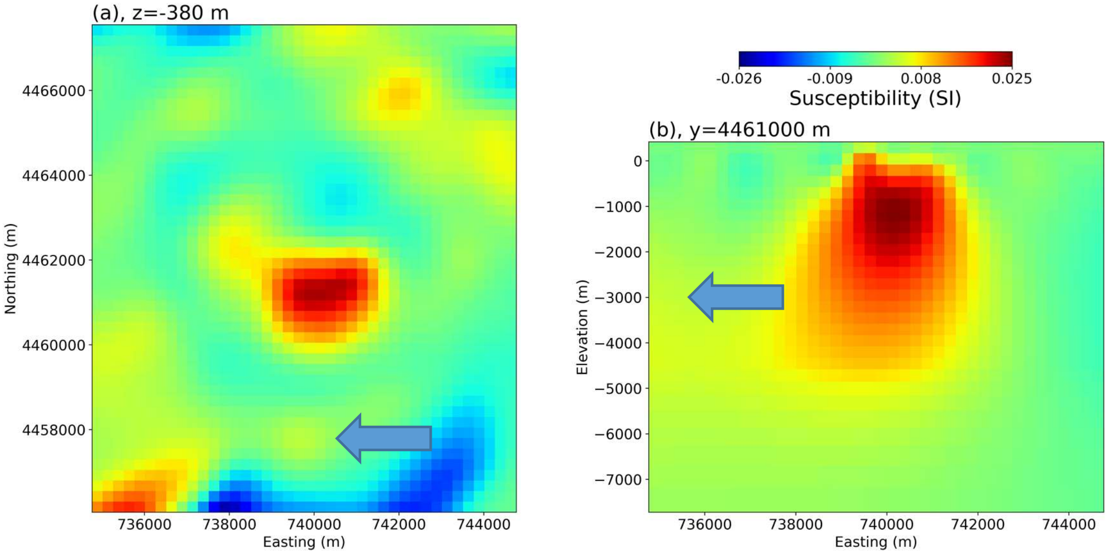

Figure 41:Jointly inverted susceptibility model. (a) is the horizontal cross-section obtained at elevation = -380 m while (b) is the vertical cross-section obtained at Northing = 4461000 m. The blue arrows indicate regions of positive susceptibility associated with unit 2

Units 1 and 2 are lithologic units that were grouped together based on sharing similar physical properties as seen in **Figure 37** and coincident boundaries as seen in **Figures 39** and **42**. Both of these units are defined by having a negative density contrast with the background country rock (**Figure 40**).

The two units were not classified as a single group, as unit 1 is significantly has positive susceptibility values while unit 2 has positive and negative susceptibility values that are closer to 0 (**Figure 41**). As stated previously, negative susceptibility indicates the presence of remanence within the lithology as the magnetic field does not align with the Earth's current magnetic field. When analyzing the spatial extent of this grouping, **Figure 42** shows that unit 2 overlays unit 1 and forms a ring-like pattern surrounding the ECCC. While unit 1 does not form a ring-like pattern around the ECCC, it does occur in multiple locations underneath unit 2. **Figure 40b** indicates these units occur mostly between the surface and 4,000 m in depth. These units do not lie within the boundaries of the ECCC, and are a part of the geologic background. It is unknown what lithology comprises this grouping as borehole data of this region were unavailable for this study. However, unit 1 and unit 2 may be a less dense portions of the Precambrian basement with a different composition than unit 5, with unit 1 being slightly more magnetized than the other basement units. The Precambrian basement is composed of a variety of different rocks including granite, diorites, schists, gneiss so it would not be surprising to find physical property contrasts within the basement rocks (Xu, 1996). This would also explain the remanence present within unit 2, as the Precambrian basement in Nevada is complex and known to contain remanence (Hinze & Chandler, 2020).

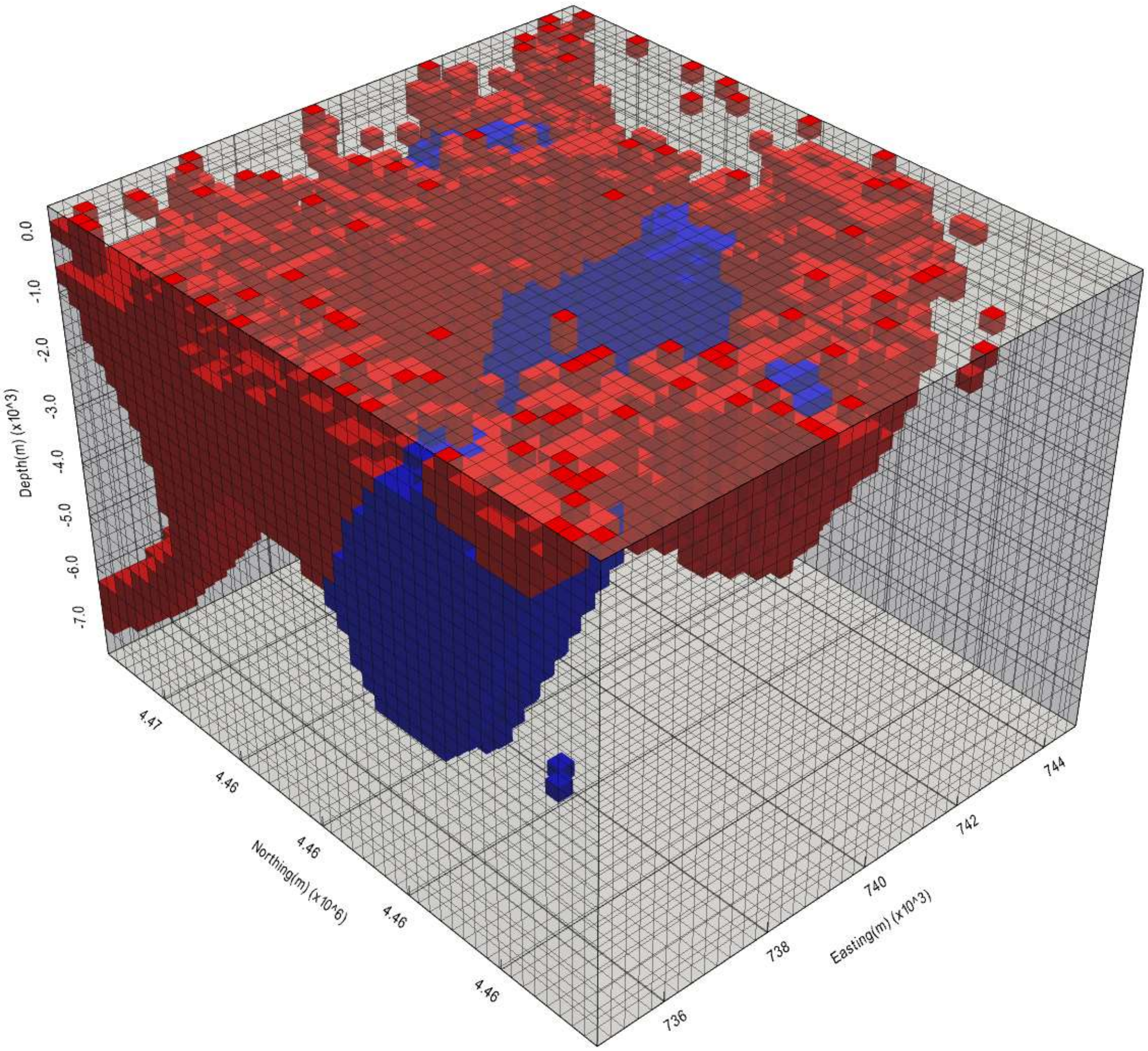

Figure 42: 3D view of units 1,2. Unit 1 is blue and unit 2 is red

Units 3 and 4

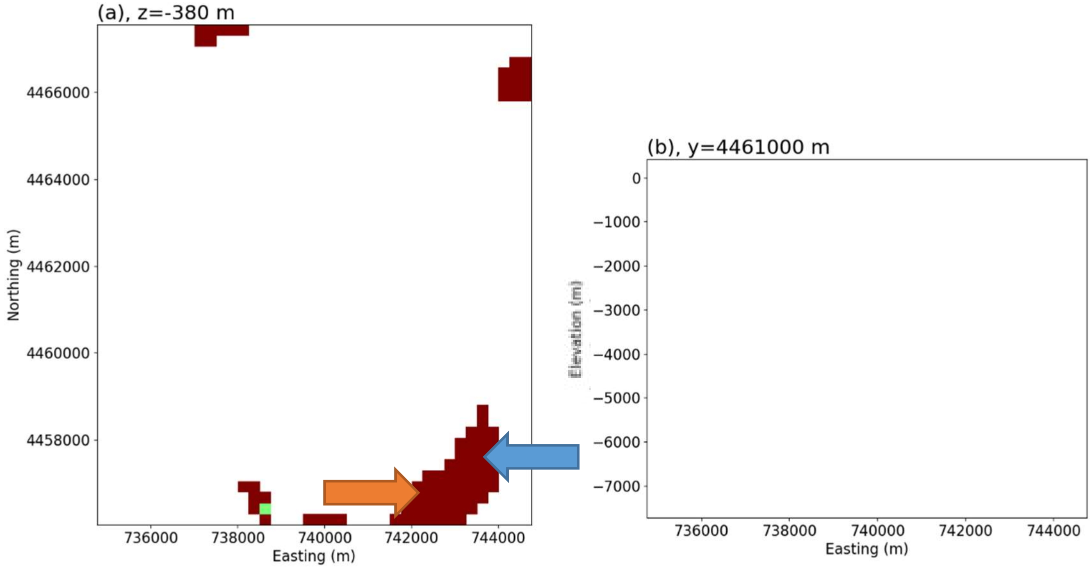

Figure 43: Cross-section view of units 3 and 4. (a) is the horizontal cross-section obtained at elevation = -380 m while (b) is the vertical cross-section obtained at Northing = 4461000 m. Unit 3 is green while unit 4 is red. The orange arrows indicate correlated features with the inverted density model while the blue arrows indicate correlated features with the inverted susceptibility model.

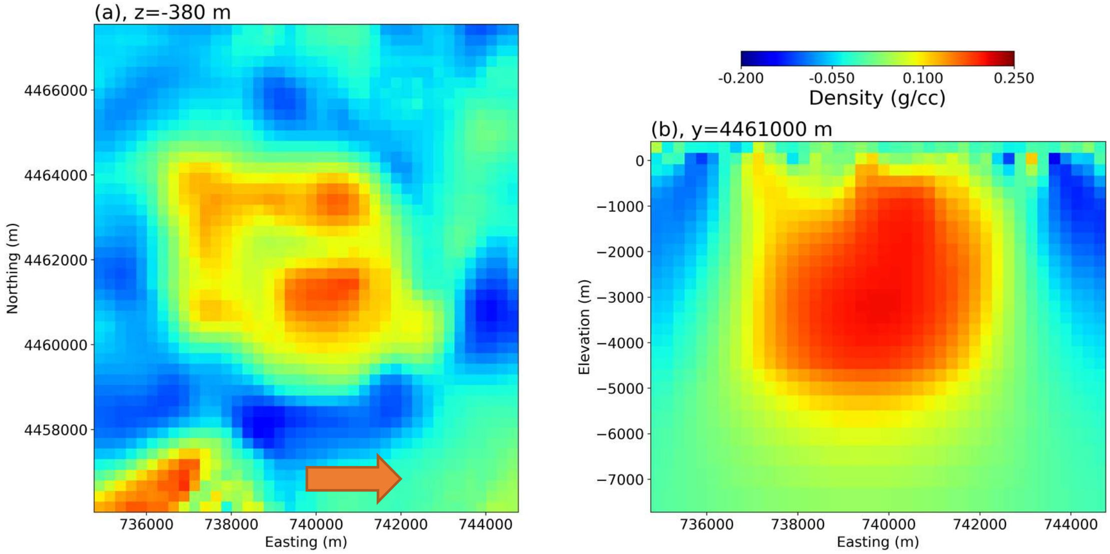

Figure 44: Jointly inverted density model. (a) is the horizontal cross-section obtained at elevation = -380 m while (b) is the vertical cross-section obtained at Northing = 4461000 m. The orange arrows indicate regions of near zero density associated with unit 4.

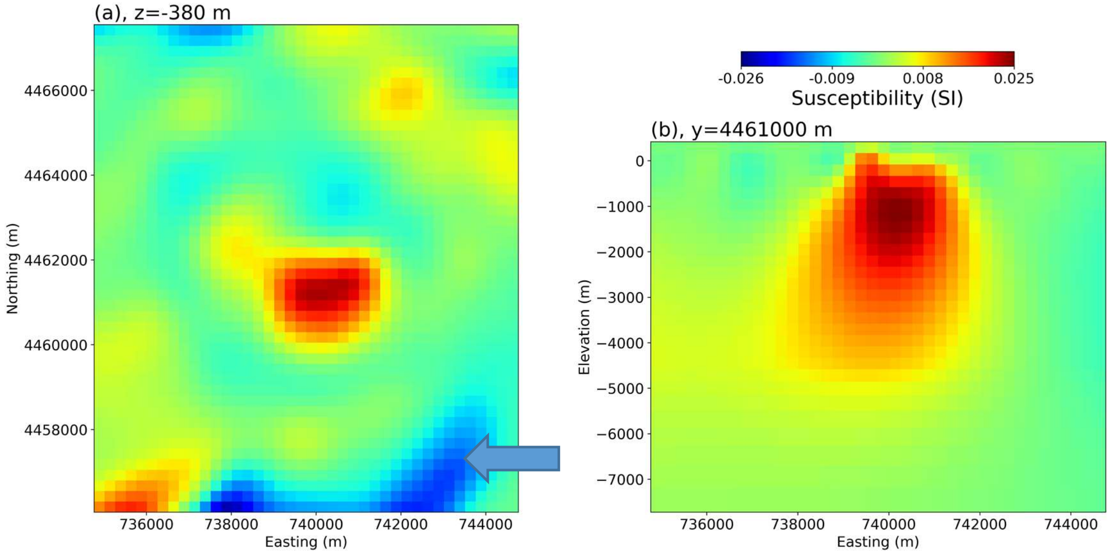

Figure 45: Jointly inverted susceptibility model. (a) is the horizontal cross-section obtained at elevation = -380 m while (b) is the vertical cross-section obtained at Northing = 4461000 m. The blue arrows indicate regions of negative susceptibility associated with unit 4

During preliminary visual observations of possible unit clustering the crossplot of jointly inverted physical property values, the clusters now identified as units 3 and 4 were easily identified by the strong inverted negative magnetic susceptibility values (**Figure 35**). Neither of these characterized units contain positive susceptibility values, indicating these units are dominated by remanent magnetization. These units are most likely mafic as mafic and ultramafic rocks frequently exhibit strong remanence (Clark, 1999). Upon comparing these unit groupings to the inverted physical property models, the spatial extent of unit 4 in **Figure 43** corresponded strongly with the negative susceptibility values in **Figure 45**. Unit 3 was barely captured in the horizontal cross-sections at 380 m in depth and was better characterized in **Figure 46**, which indicates that units 3 and 4 share coincident boundaries. **Figure 43** indicates the unit is at the edges of the survey area while **Figure 46** also indicates that these units occur mainly at the northwest and southeast ends of the survey area and extend from the surface to 7,000 m below sea level. These units are considered part of the geologic background for the purposes of this study as they lie outside the bounds of the carbonatite. I hypothesize units 3 and 4 are mafic portions of the Precambrian basement composed of rocks such as basalt, although additional borehole data are required to assign a lithology to these units.

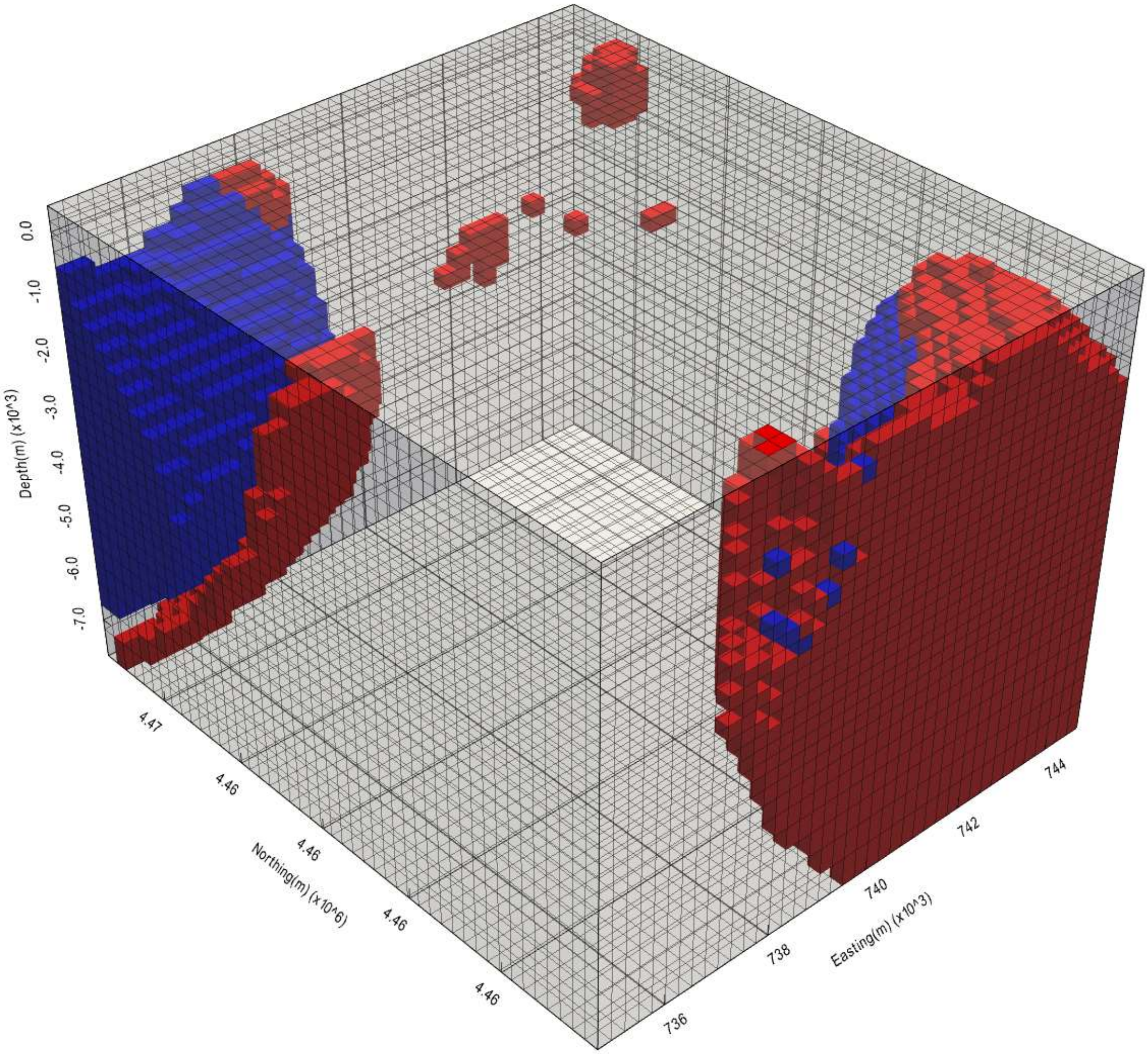

Figure 46: 3D view of units 3,4. Unit 3 is blue and unit 4 is red

Unit 5: Country Rock

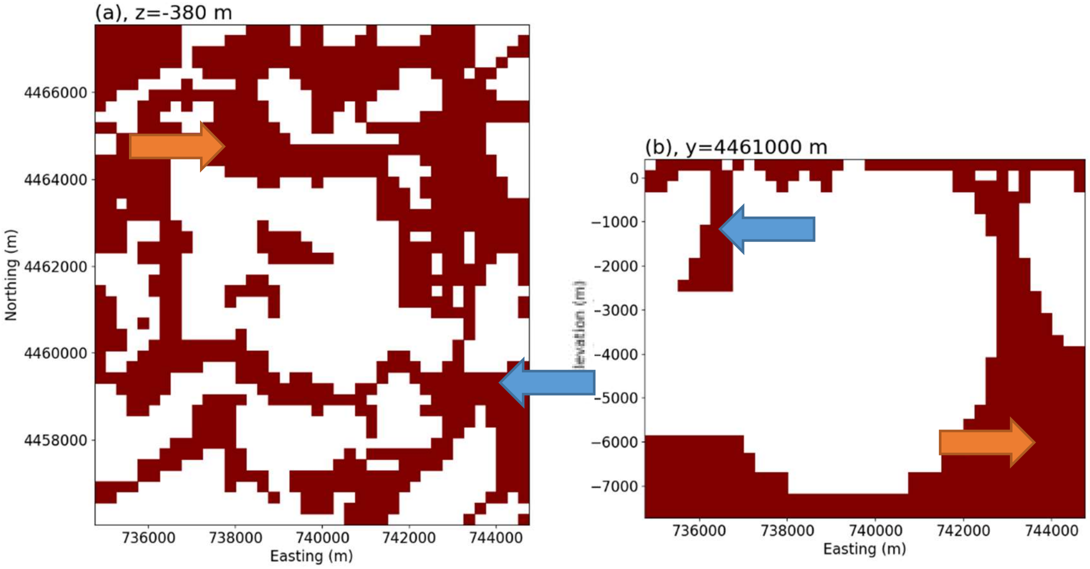

Figure 47: Cross-section view of unit 5. (a) is the horizontal cross-section obtained at elevation = -380 m while (b) is the vertical cross-section obtained at Northing = 4461000 m. Unit 5 is in red. The orange arrows indicate correlated features with the inverted density model while the blue arrows indicate correlated features with the inverted susceptibility model.

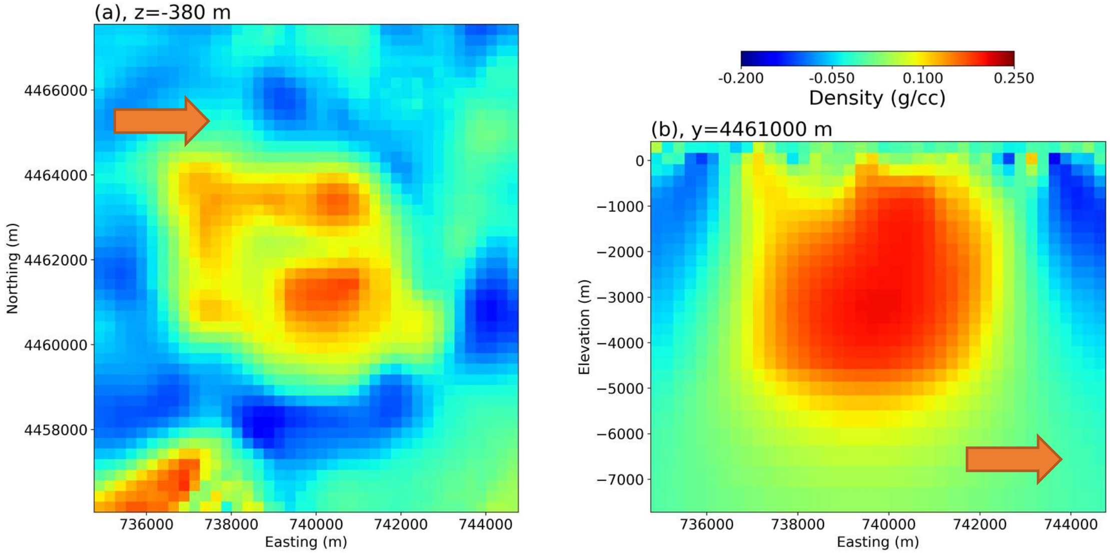

Figure 48: Jointly inverted density model. (a) is the horizontal cross-section obtained at elevation = -380 m while (b) is the vertical cross-section obtained at Northing = 4461000 m. The orange arrows indicate regions of near zero density associated with unit 5

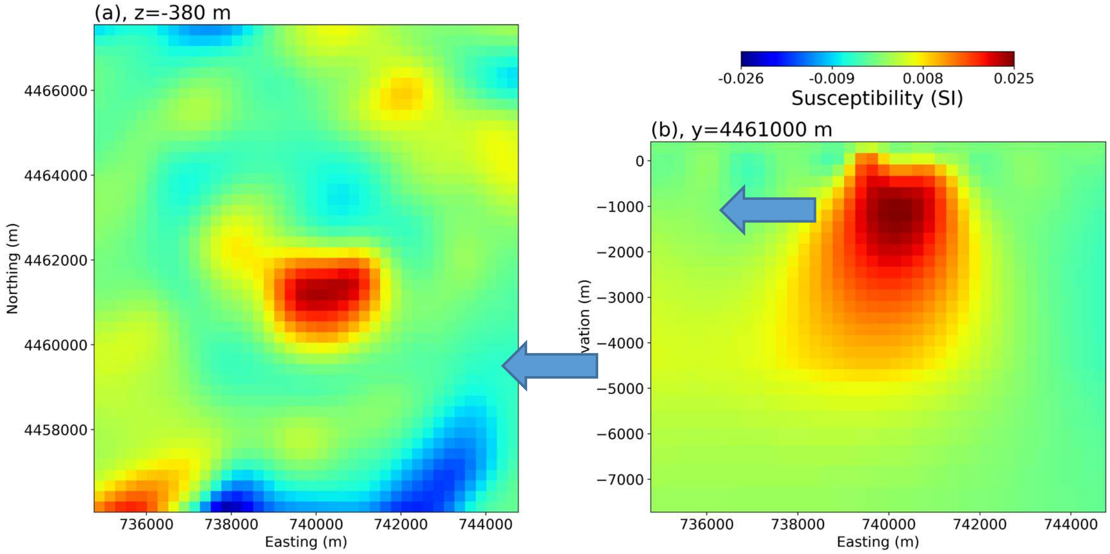

Figure 49: Jointly inverted susceptibility model. (a) is the horizontal cross-section obtained at elevation = -380 m while (b) is the vertical cross-section obtained at Northing = 4461000 m. The blue arrows indicate regions of near zero magnetic susceptibility associated with unit 5.

Unit 5 is classified as Precambrian gneissic country rock, as it is the largest unit within the survey area. As the background unit, the density and susceptibility contrast values are closest to 0, which is reflected upon comparing **Figure 47** to the inverted physical property models (**Figure 48** and **49**). This result does somewhat contrast with Drenth (2014) which depicts the average susceptibility of the basement rock as being higher than the carbonatites. This discrepancy is likely due to the diverse nature the Precambrian basement along with more magnetically susceptible portions of the basement being allocated to other units such as unit 1. **Figure 47b** shows that the unit encircles a region between 73600 and 742000 m easting, which encapsulate the estimated bounds of the carbonatite at this location. It also appears that this grouping captures the 200 m of Pennsylvanian sediment which overlays the ECCC and the survey area, as seen in **Figure 50**. This is understandable as the sedimentary overburden is expected to have near zero relative density and susceptibility values.

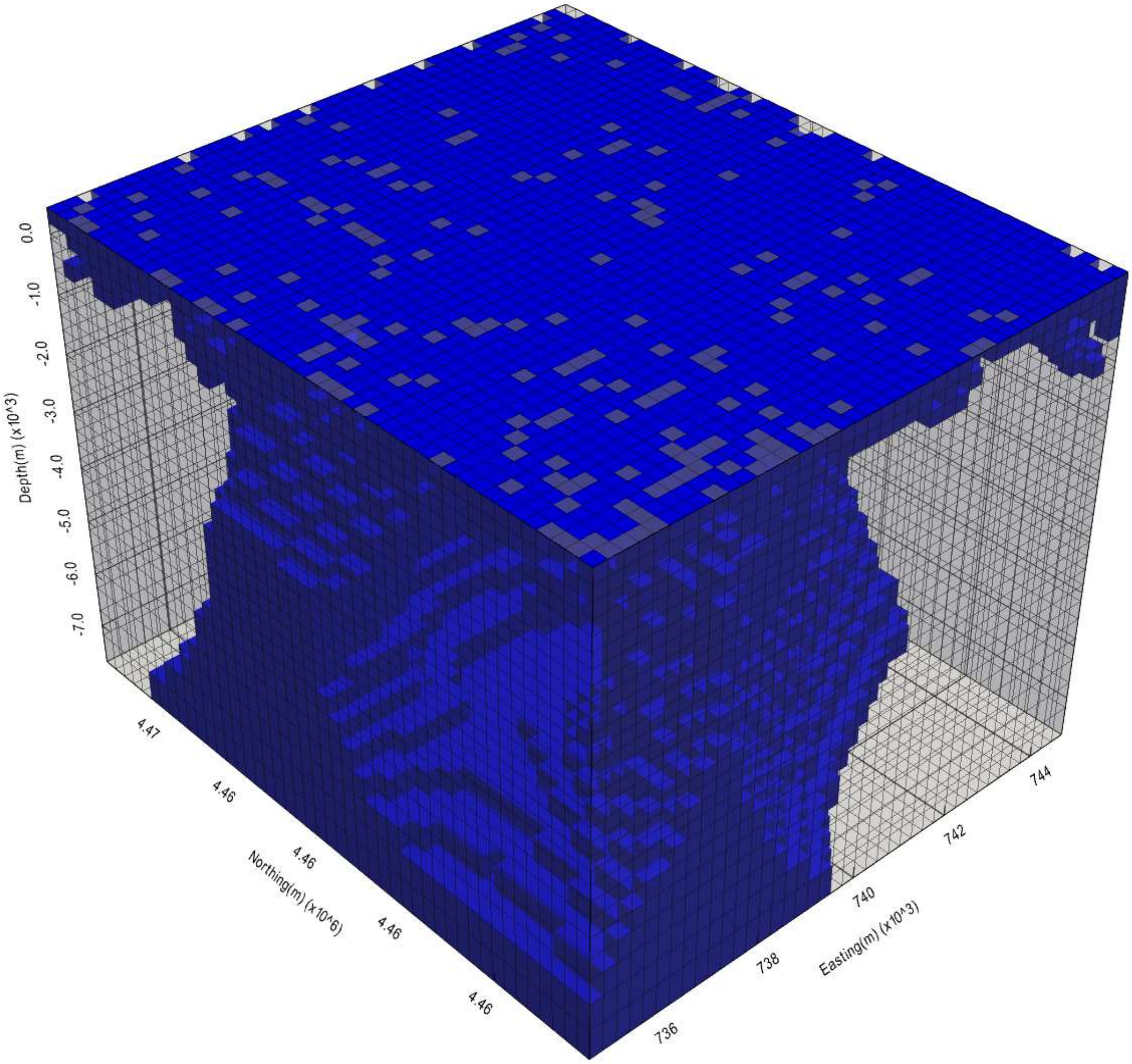

Figure 50: 3D view of unit 5 (country rock)

Unit 6: Mafic Rock

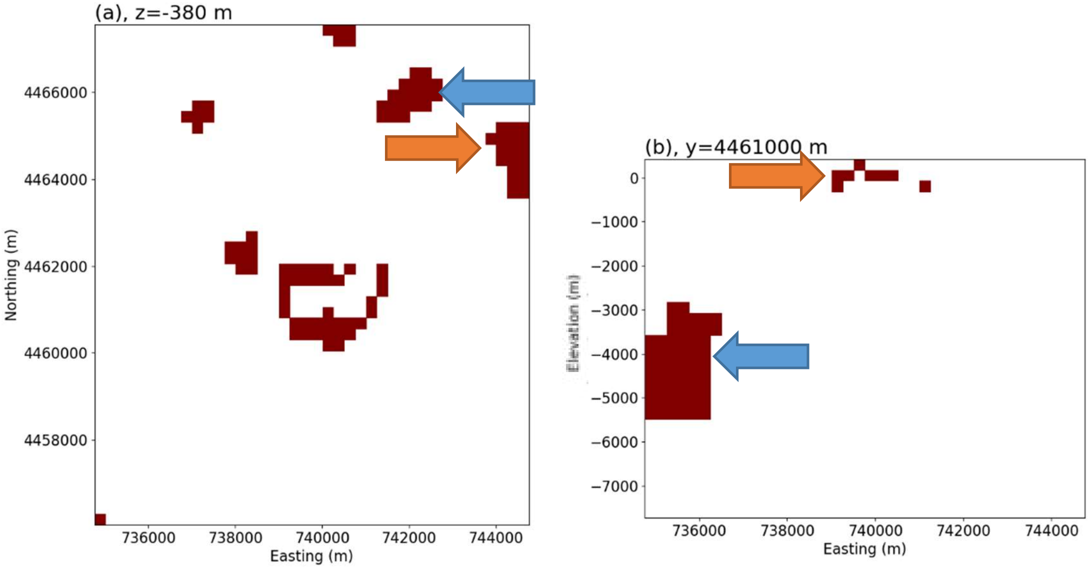

Figure 51: Cross-section view of unit 6. (a) is the horizontal cross-section obtained at elevation = -380m while (b) is the vertical cross-section obtained at Northing = 4461000 meters. Unit 6 is in red. The orange arrows indicate correlated features with the inverted density model while the blue arrows indicate correlated features with the inverted susceptibility model.

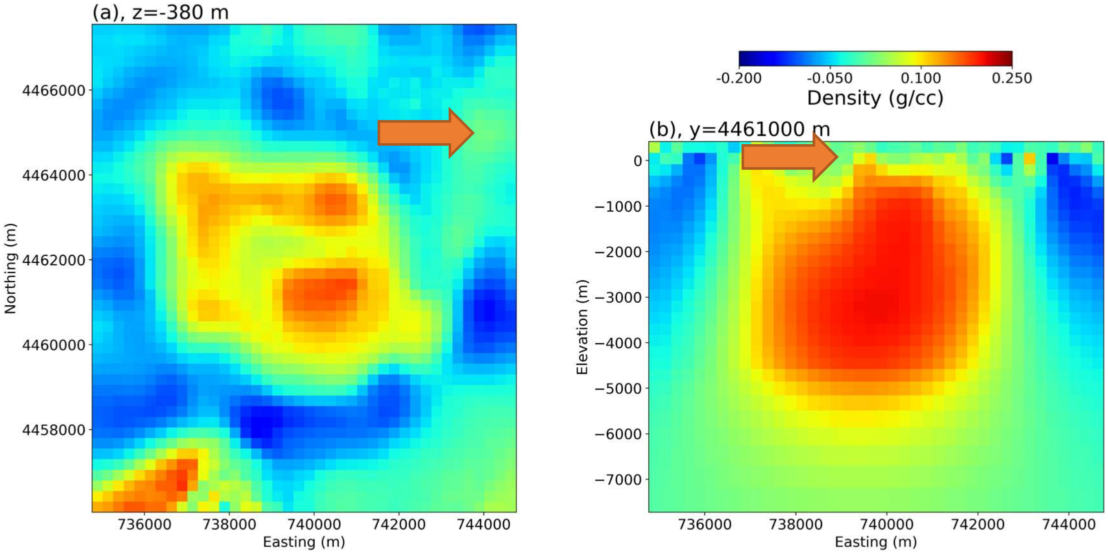

Figure 52: Jointly inverted density model. (a) is the horizontal cross-section obtained at elevation = -380 m while (b) is the vertical cross-section obtained at Northing = 4461000 m. The orange arrows indicate regions of near zero and slightly positive densities associated with unit 6.

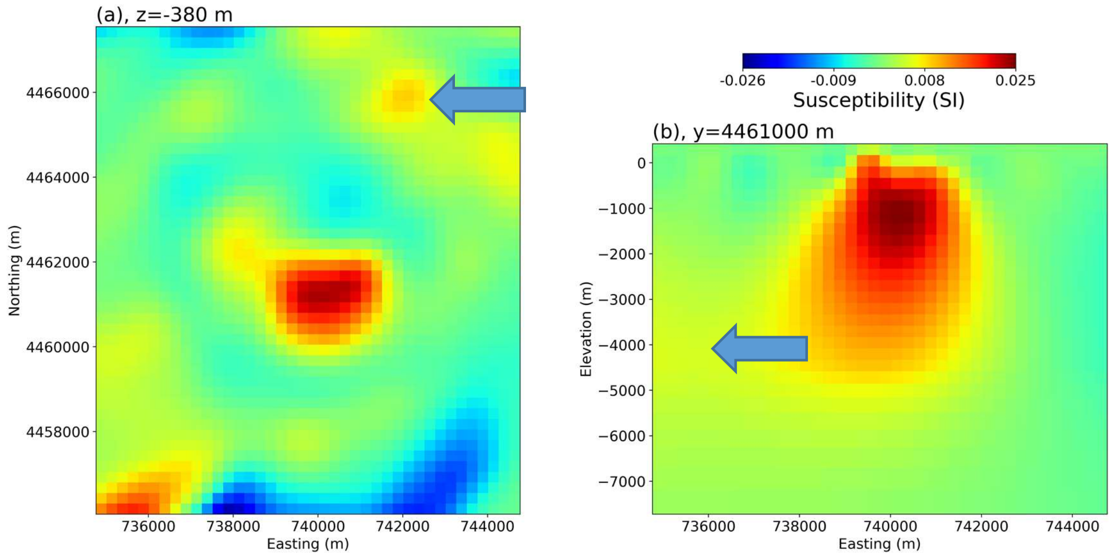

Figure 53: Jointly inverted susceptibility model. (a) is the horizontal cross-section obtained at elevation = -380 m while (b) is the vertical cross-section obtained at Northing = 4461000 m. The blue arrows indicate regions of positive magnetic susceptibility associated with unit 6.

Unit 6 is unit with high magnetic susceptibility values classified as mafic rocks in Drenth (2014). The unit is on average has high magnetic susceptibility, and shares similar densities to most of the country rock. This unit was not identified through clustered values in the jointly inverted physical property crossplot (**Figure 35**), so most of the classification of this unit was determined by visualizing the unit in 3D and inspecting its spatial correlation with the inverted physical property values as seen in **Figures 52** and **53**. The identification of the mafic units is easier to see with features present in the inverted susceptibility model, with the overall physical properties of the mafic unit matching the patterns described in Drenth (2014). The classification of mafic lamprophyre predicted in **Figure 36** could not be uniquely distinguished from the other mafic rocks. This is likely due to its low magnetic susceptibility and similar density to both the country rock and mafic rocks, meaning it may be contained within either classification. **Figure 54** reveals that the three bodies in the top right of **Figure 51a** are connected with one another and form a large body close to the central carbonatites, while there is a deeper portion of the unit in the southwest of the survey region. Kass et al. (2015) describes the southwest corner as belonging to the northeastern portion of the Nemaha Uplift.

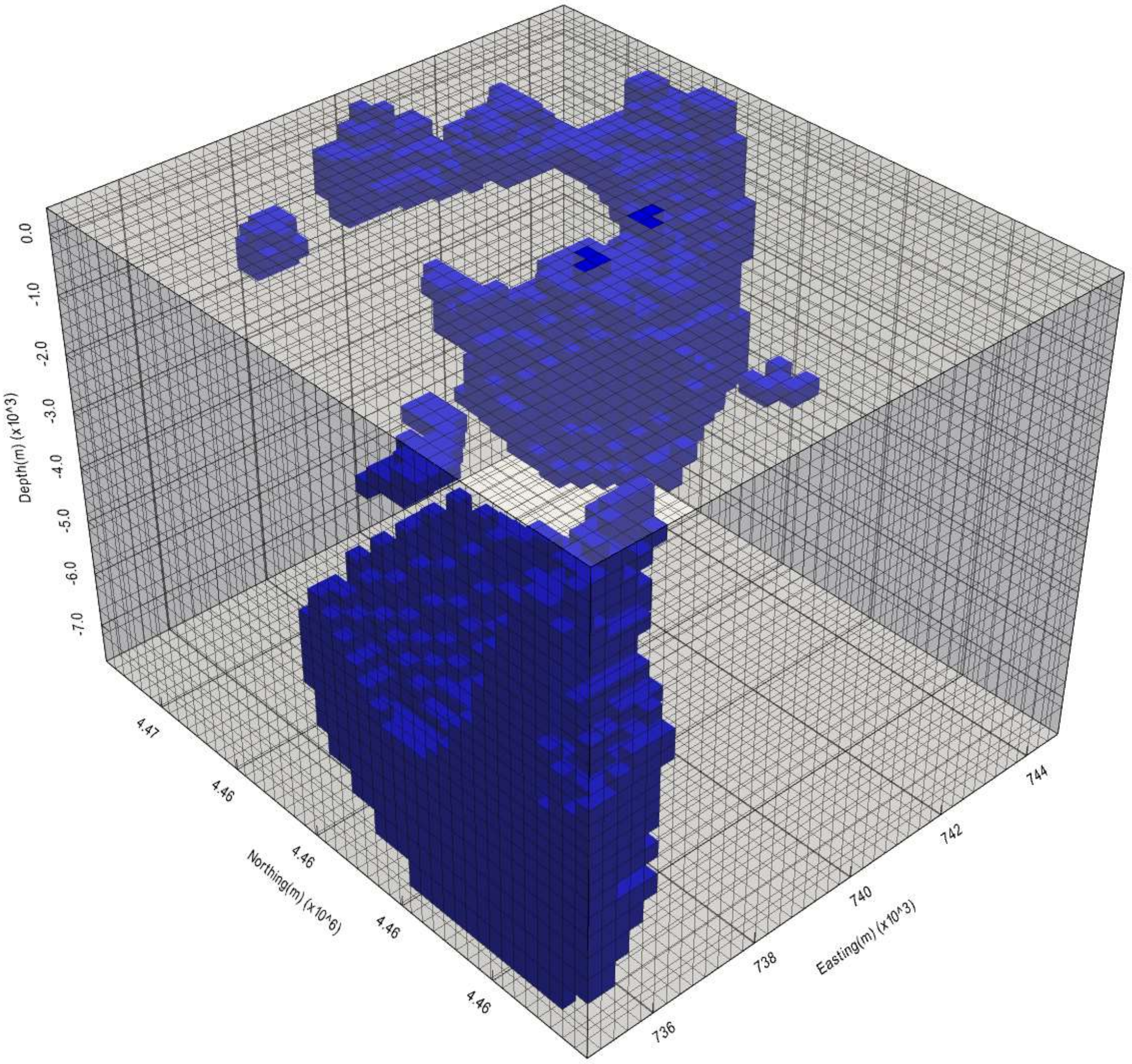

Figure 54: 3D view of unit 6 (mafic rock)

Unit 7: Undifferentiated Carbonatites

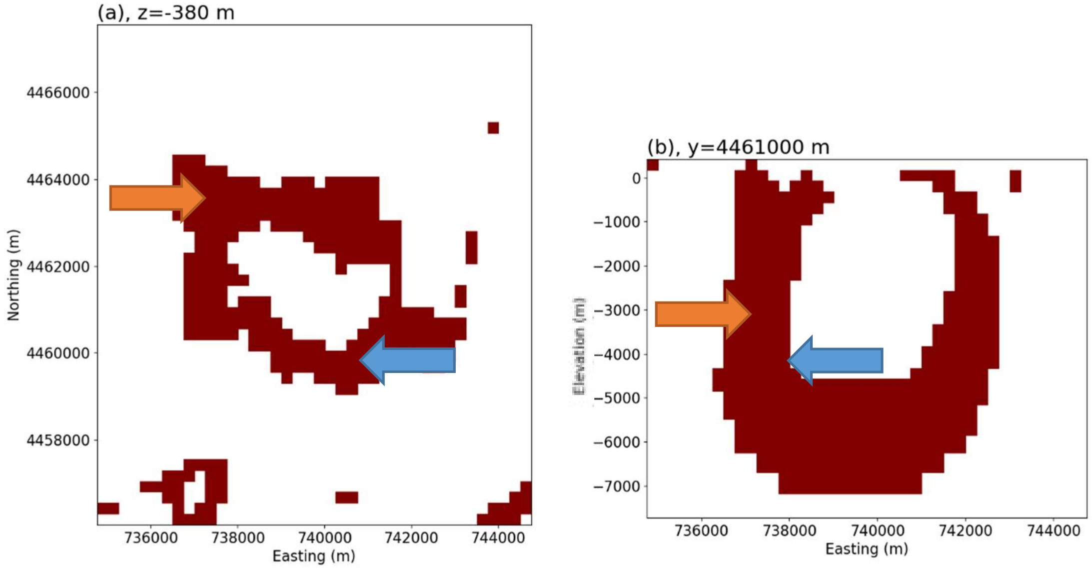

Figure 55: Cross-section view of unit 7. (a) is the horizontal cross-section obtained at elevation = -380 m while (b) is the vertical cross-section obtained at Northing = 4461000 m. Unit 7 is in red. The orange arrows indicate correlated features with the inverted density model while the blue arrows indicate correlated features with the inverted susceptibility model.

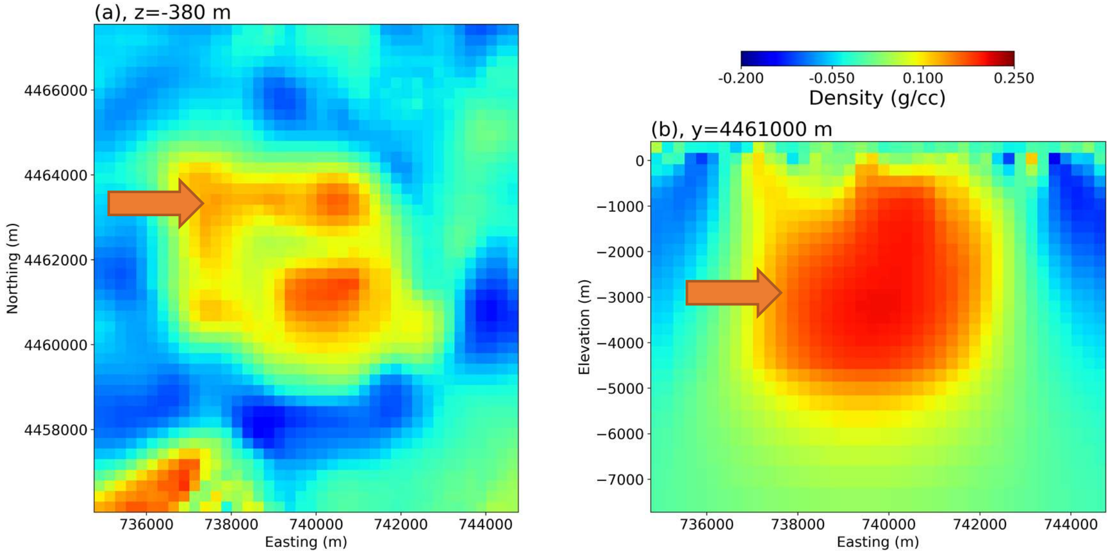

Figure 56: Jointly inverted density model. (a) is the horizontal cross-section obtained at elevation = -380 m while (b) is the vertical cross-section obtained at Northing = 4461000 m. The orange arrows indicate regions of positive densities associated with unit 7.

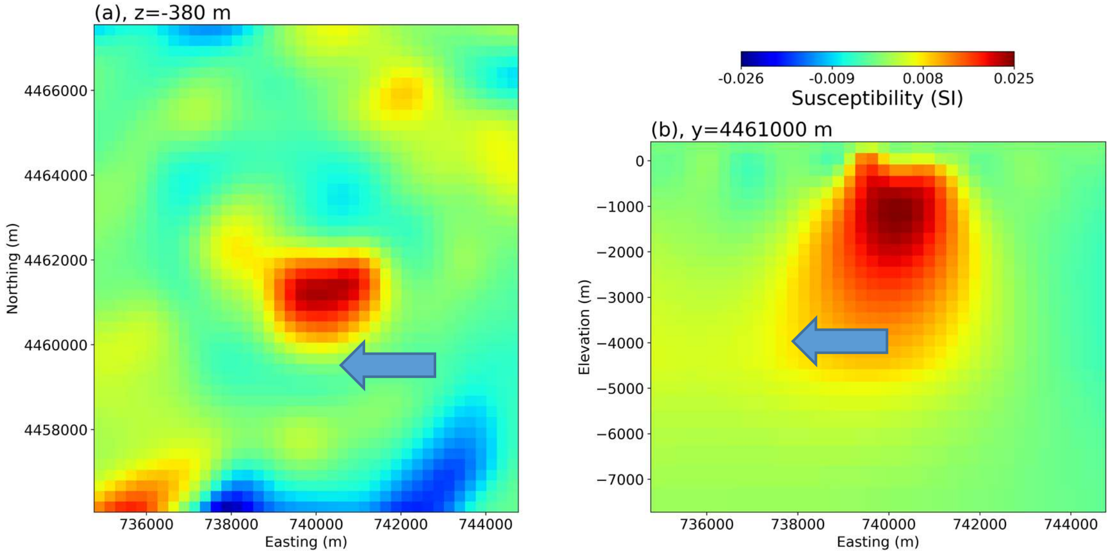

Figure 57: Jointly inverted susceptibility model. (a) is the horizontal cross-section obtained at elevation = -380 m while (b) is the vertical cross-section obtained at Northing = 4461000 m. The blue arrows indicate regions of near zero to slightly positive magnetic susceptibility associated with unit 7.

Most of the ECCC has been classified as undifferentiated carbonatites in unit 7. **Figure 56** shows relative density of this unit is denser than the background country rock but less dense than some of the other geologic units, which is expected based on the properties measured in Drenth (2014). However, the susceptibility values do not match the physical property relations recorded in Drenth (2014) as the undifferentiated carbonatites are more magnetized than the country rock in some locations as seen in **Figure 57**. The decision was made to retain the higher susceptibility values within unit 7 in order to capture regions such as the one indicated by the blue arrow in **Figure 57b**. If this region was not classified as part of unit 7, the spatial extent of the undifferentiated carbonatites would not be continuous and the inverted density values at the same location in **Figure 56b** indicated the presence of a continuous body.

An important note is that unit 7 contains negative susceptibility values which indicate the presence of remanence within the undifferentiated carbonatites, and also implies the other carbonatites at Elk Creek contain some degree of remanence. The ECCC formed around 0.55 Ga within the ancient continent of Laurentia which includes the modern continent of North America (Carlson & Treves, 2005, Torsvik et al., 2012). Torsvik et al. (2012) indicates that around this time, the Apparent Polar Wander

Path (APWP) for Laurentia placed the location of a paleopole next to the equator. The modern location of the Elk Creek carbonatite is at about 41 degrees N in latitude, indicating a roughly 41 degrees distance between a possible remanent field within the carbonatite and the modern inducing field. Although there is no information on the remanence at Elk Creek, the steep angle between a possible remanent field and the modern inducing field could result in magnetization opposite to the modern inducing field.

The boundaries of the central body depicted in **Figure 55a** matches well with the expected boundaries of the ECCC shown in **Figure 2**, with the empty region in the middle being composed mostly of the mafic rocks of unit 6 and the magnetite-dolomite carbonatite of unit 8. Drenth (2014) predicted that the carbonatite may be a crude funnel shape that tapered in depth due to a region of lower gravity at the center of the complex as seen in **Figure 26**. However, the spatial extent of the undifferentiated carbonatites as plotted in **Figure 58** shows that the ECCC does not taper in depth. This result is also supported by the inverted density model from Kass et al. (2015) which depicted the carbonatites as a roughly rectangular body down to about 3500 m in depth. However, this does not exclude the possibility that the shape of the ECCC in this study may be a consequence of isotropic smoothing from regularization. This means the possibility of a funnel shape as proposed in Drenth (2014) is not ruled out.

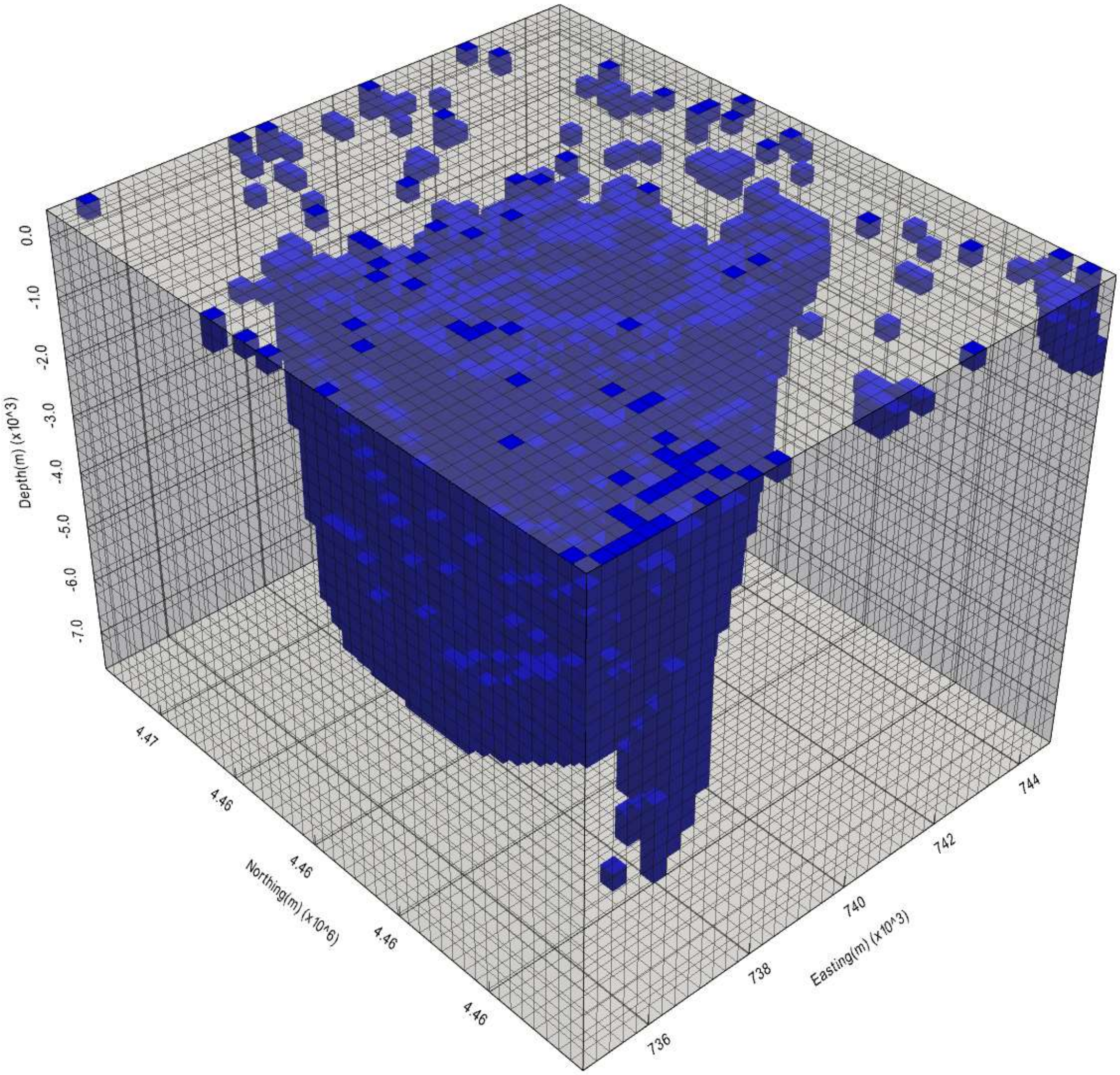

Figure 58: 3D view of unit 7 (undifferentiated carbonatites)

Original Target Unit Classification: Magnetite-Dolomite Carbonatite

In this study, the units now classified as units 8 and 9 were originally classified as a single target unit representing magnetite-dolomite carbonatite. From the physical properties measured in Drenth (2014), the initial assumption was that the densest and most magnetically susceptible values at Elk Creek should belong only to the magnetite-dolomite carbonatite based on geology intercepted by boreholes. This original classification within the crossplot of jointly inverted values is shown in **Figure 59**, with the resulting spatial domain cross-sections of this unit shown in **Figure 60**. The problem with this classification is that the volume of this unit as shown in **Figure 61** is larger than the estimated <2% volume of the magnetite-dolomite carbonatite in regards to the units within the ECCC from Drenth (2014). Additionally, none of the previous studies on the carbonatite such as SRK Consulting (2015) predicted this large of a volume for the magnetite-dolomite carbonatite. To stay consistent with previous studies, I divided this unit into two separate units as a conservative estimation of the volume of the magnetite-dolomite carbonatite. These two units are further explained below.

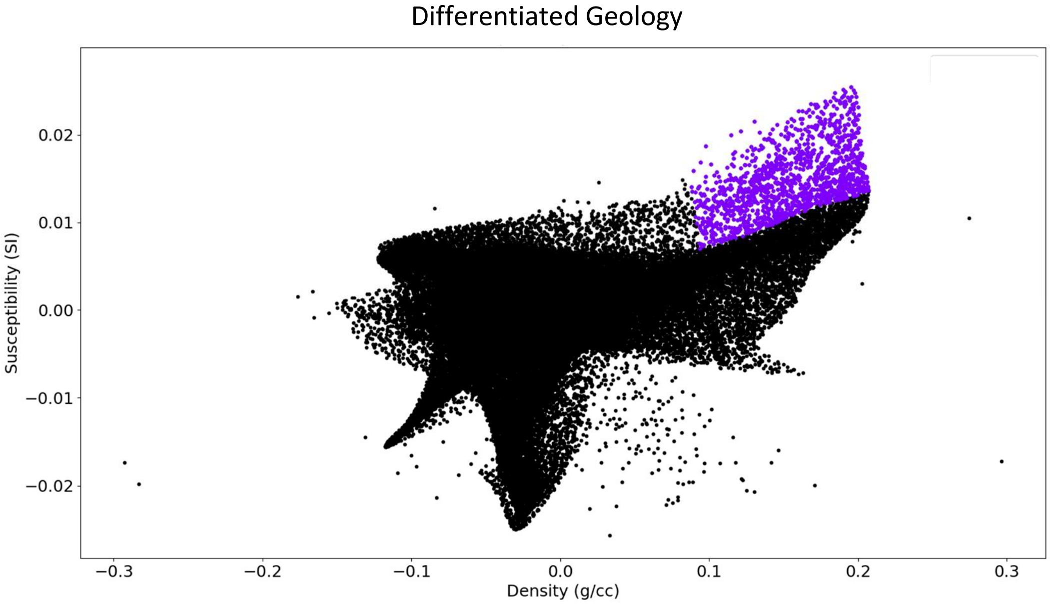

Figure 59: Crossplot showing the original differentiation of the magnetite-dolomite carbonatite at Elk Creek.

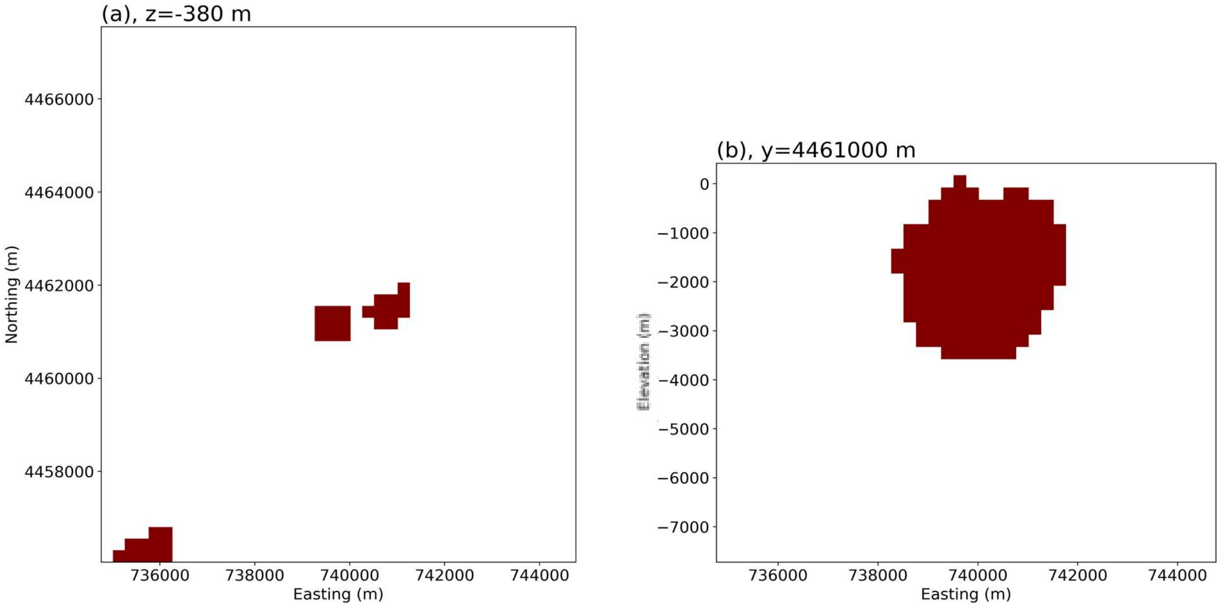

Figure 60: Cross-section view of the original classification for magnetite-dolomite carbonatite with the unit shown in red. (a) is the horizontal cross-section obtained at elevation = -380 m while (b) is the vertical cross-section obtained at Northing = 4461000 m.

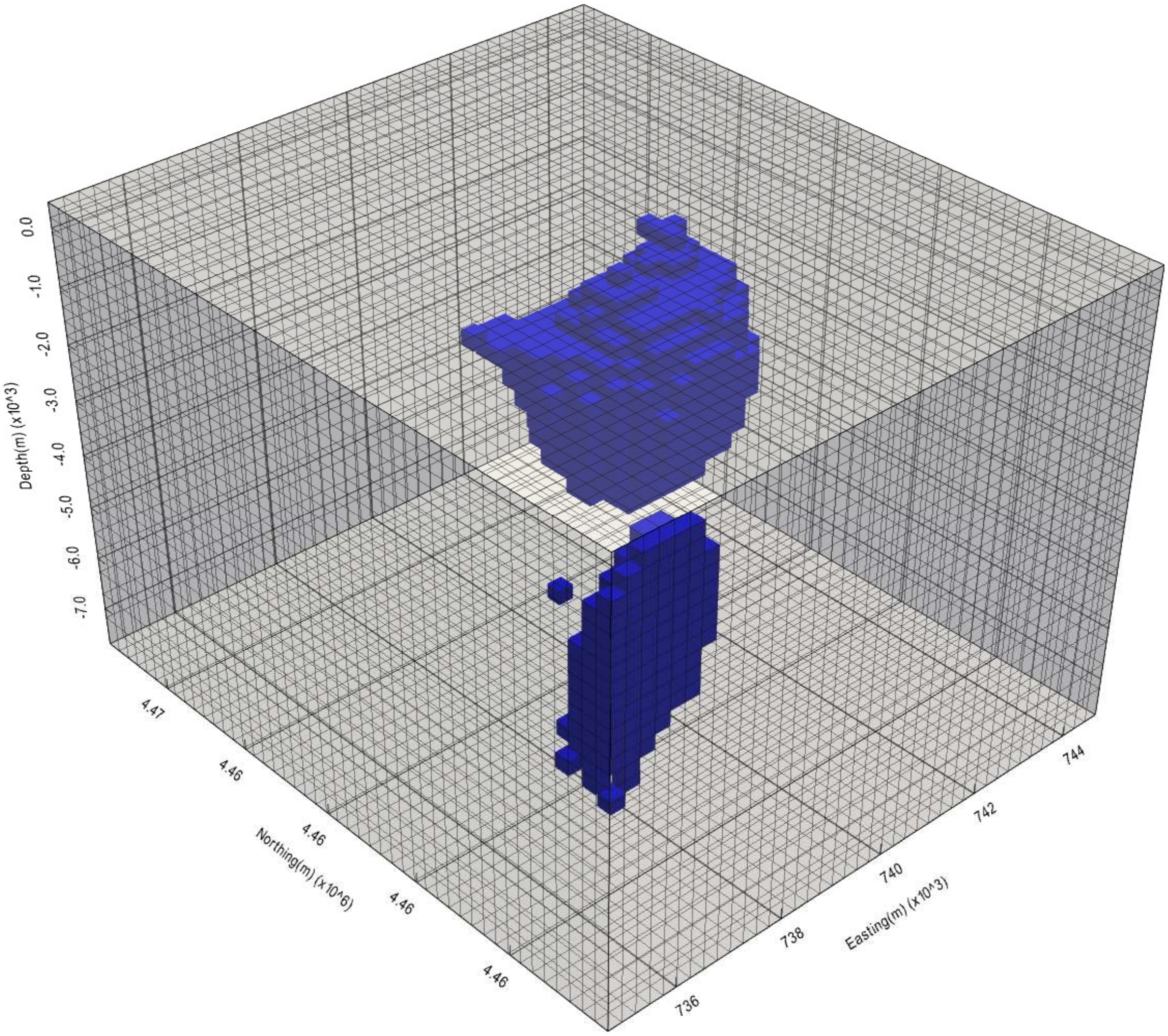

Figure 61:3D view of the original classification of the magnetite-dolomite carbonatite

Unit 8: Magnetite-Dolomite Carbonatite

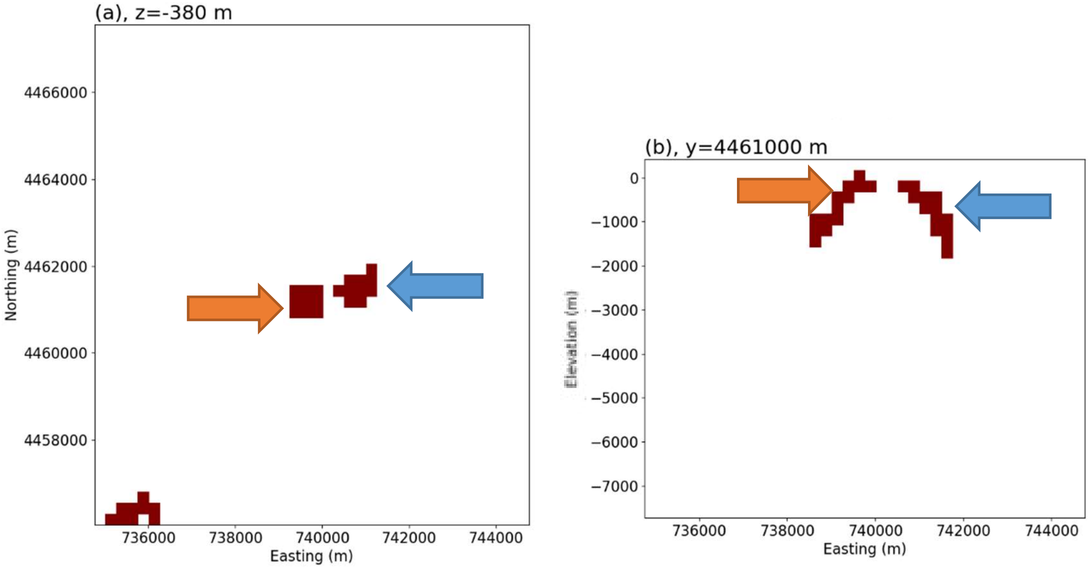

Figure 62: Cross-section view of unit 8. (a) is the horizontal cross-section obtained at elevation = -380 m while (b) is the vertical cross-section obtained at Northing = 4461000 m. Unit 8 is in red. The orange arrows indicate correlated features with the inverted density model while the blue arrows indicate correlated features with the inverted susceptibility model.

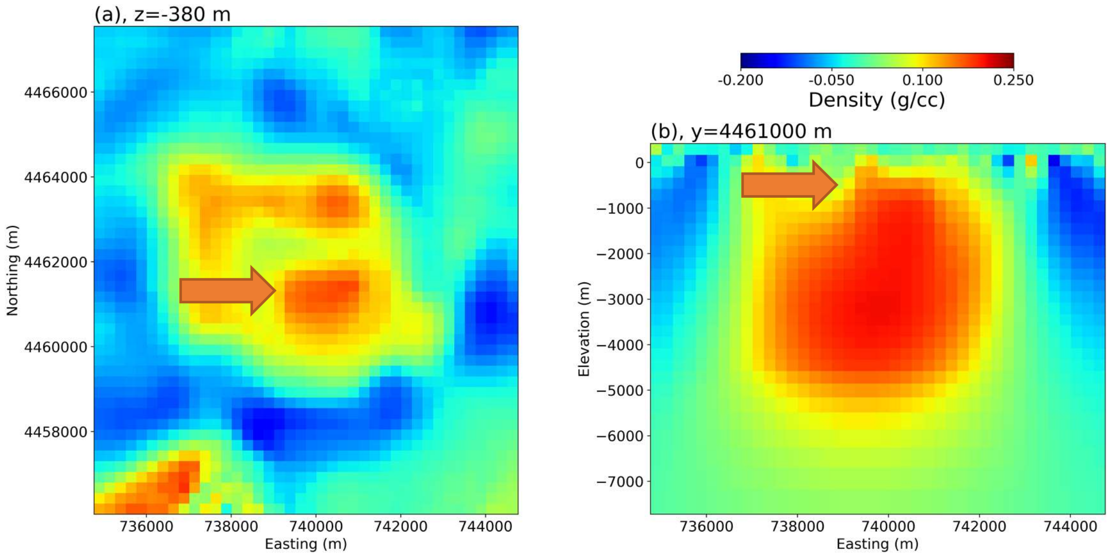

Figure 63: Jointly inverted density model. (a) is the horizontal cross-section obtained at elevation = -380 m while (b) is the vertical cross-section obtained at Northing = 4461000 m. The orange arrows indicate regions of positive densities associated with unit 8.

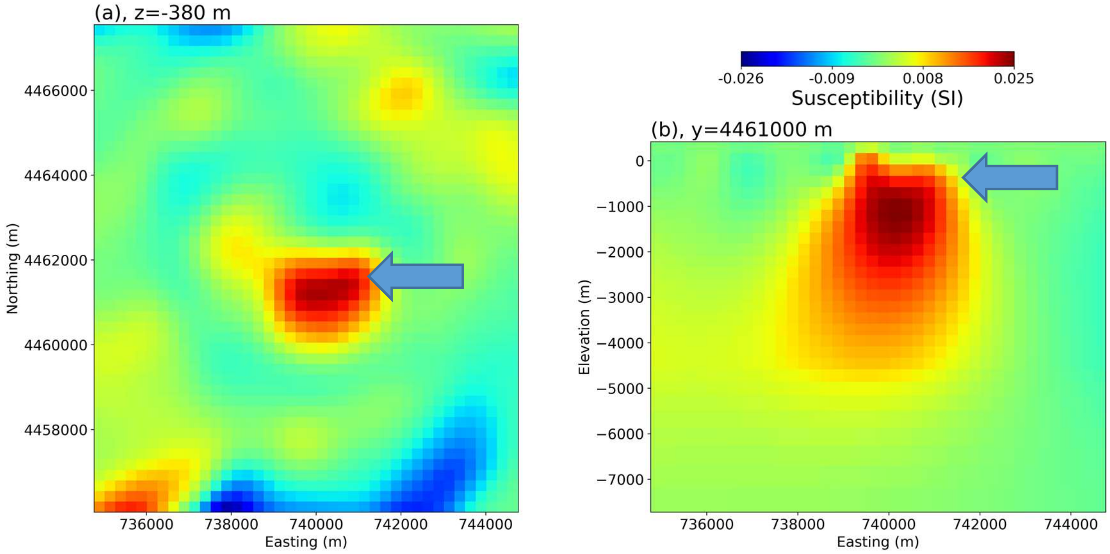

Figure 64: Figure 65: Jointly inverted susceptibility model. (a) is the horizontal cross-section obtained at elevation = -380 m while (b) is the vertical cross-section obtained at Northing = 4461000 m. The blue arrows indicate regions of positive susceptibilities associated with unit 8.

The modified characterization of the magnetite-dolomite carbonatite located within Elk Creek was classified as unit 8 in the geology differentiation. As stated previously, the original expectation for classifying the magnetite-dolomite carbonatite was that this lithologic unit would have the highest density and susceptibility values at Elk Creek. However, the location of the main niobium ore zone has been identified by previous work (i.e., Drenth, 2014; Blessington, 2014; SRK Consulting, 2015) and **Figure 38** reveals that the highest physical property values classified as unit 9 in **Figure 37** are located spatially below the known niobium ore zone. A large source of uncertainty in this classification is the distinction between the classified magnetite-dolomite carbonatite and unit 9, due to the lack of deep borehole data. This classification of the magnetite-dolomite carbonatite is made based on conservative estimations of the volume from existing shallow borehole data, although the volume may be far larger than previously expected. It is also likely that a significant portion of the magnetite rich dolomite-carbonatite breccia was also included in this classification, due to similar geophysical responses.

The known niobium ore zone is located at about 739,520 easting and 4,460,900 northing which matches the location of the square body in Figure 43a (SRK Consulting, 2015). Additionally, previous studies of the 2011 Falcon® AGG data indicated the presence of an anomaly with similar responses to the known ore zone about 1,200 m to the east (SRK Consulting, 2014). These observations were supported by the identification of the second body at the center of **Figure 62a**, which is shown to be a part of a continuous body with the niobium ore zone in **Figure 66**. A borehole block model was constructed by SRK Consulting (2015) which revealed that between an elevation of 150 to -600 m, the niobium ore zone is a relatively thin vertical feature. Drenth (2014) also predicted that the magnetite-dolomite carbonatite should extend below an elevation of -600 m down to -1,000 m. **Figure 62b** supports the results of these previous studies, and also suggests the main niobium ore zone dips west down below an elevation of -1,500 m. **Figure 65** also shows the presence of an anomaly in the southwest region of the survey area with very similar physical properties to the magnetite-dolomite carbonatite, corresponding to the northeastern portion of the Nemaha uplift (Kass et al., 2015).

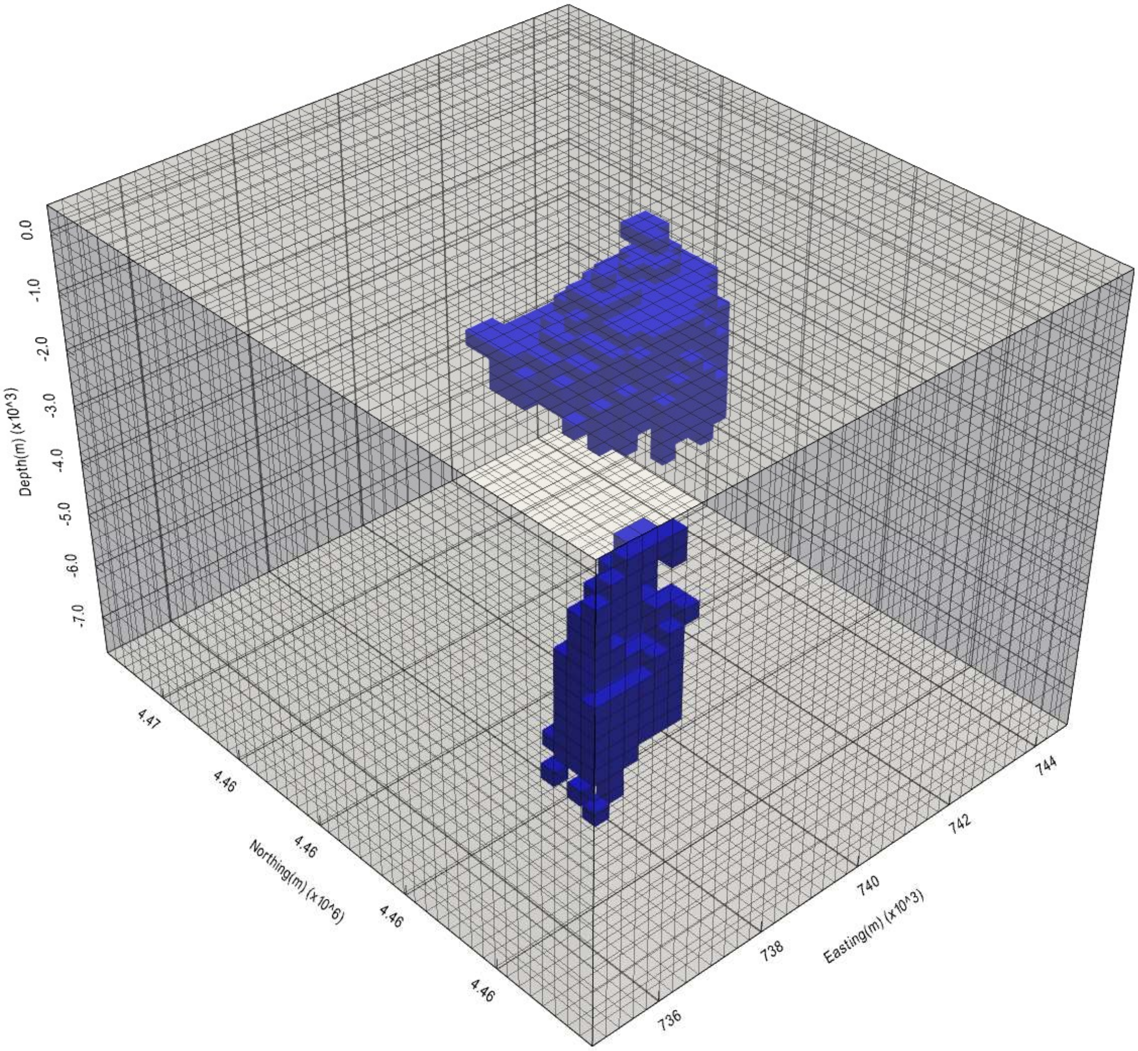

Figure 66: 3D view of unit 8 (magnetite-dolomite carbonatite)

Unit 9

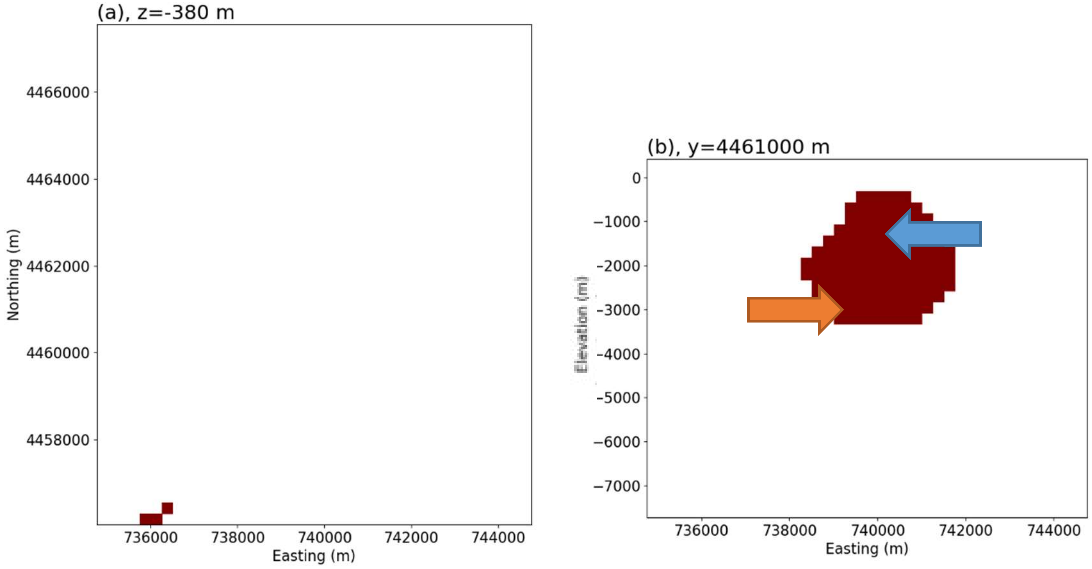

Figure 67: Cross-section view of unit 9. (a) is the horizontal cross-section obtained at height = -380m while (b) is the vertical cross-section obtained at Northing = 4461000 meters. Unit 9 is in red. The orange arrows indicate correlated features with the inverted density model while the blue arrows indicate correlated features with the inverted susceptibility model.

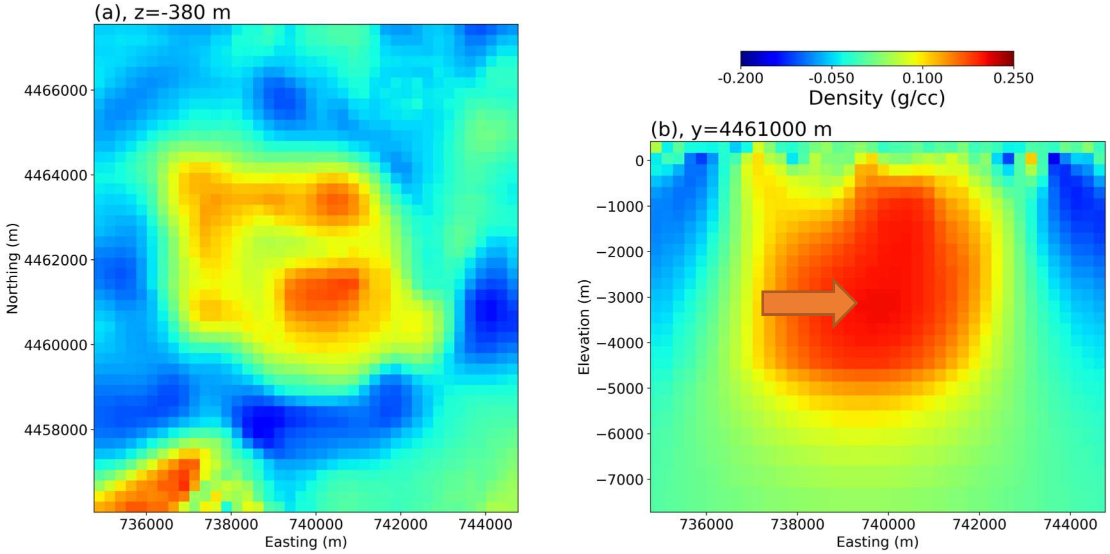

Figure 68: Jointly inverted density model. (a) is the horizontal cross-section obtained at elevation = -380 m while (b) is the vertical cross-section obtained at Northing = 4461000 m. The orange arrows indicate regions of positive densities associated with unit 9.

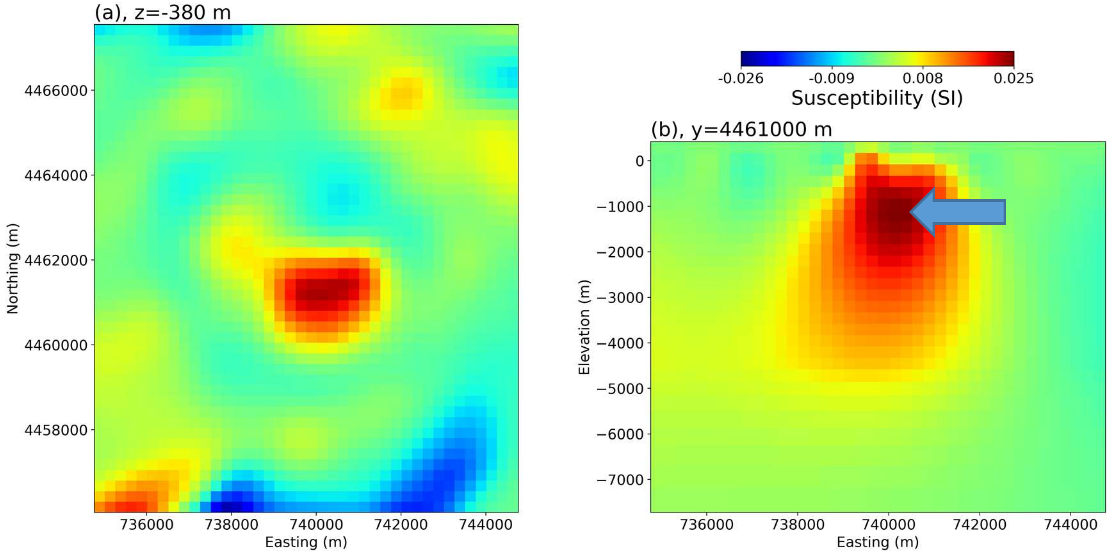

Figure 69: Jointly inverted susceptibility model. (a) is the horizontal cross-section obtained at elevation = -380 m while (b) is the vertical cross-section obtained at Northing = 4461000 m. The blue arrows indicate regions of positive susceptibility associated with unit 9.

As stated previously, the densest and most magnetically susceptible values in **Figure 37** were classified as unit 9 rather than as magnetite-dolomite carbonatite. This is shown in **Figures 68** and **69**, where the positive values at the center of both physical property models were incorporated into unit 9. This unit is surprisingly large in volume, and is located at the center of the ECCC (**Figure 70**). According to the physical properties analyzed in Drenth (2014), the densest and most magnetically susceptible unit should be classified as magnetite-dolomite carbonatite, however the majority of unit 9 lies below the deepest available borehole data. Additionally, the volume of unit 9 is larger than the predicted volume of magnetite-dolomite carbonatite in Drenth (2014). Due to the uncertainty regarding the bounds of the classified magnetite-dolomite carbonatite, it is likely that at least a portion of this unit is still magnetite-dolomite carbonatite. However, it is difficult to determine as to whether the rest of the unit is also magnetite-dolomite carbonatite or an unidentified carbonatite unit which has relatively higher density and magnetic susceptibility values.

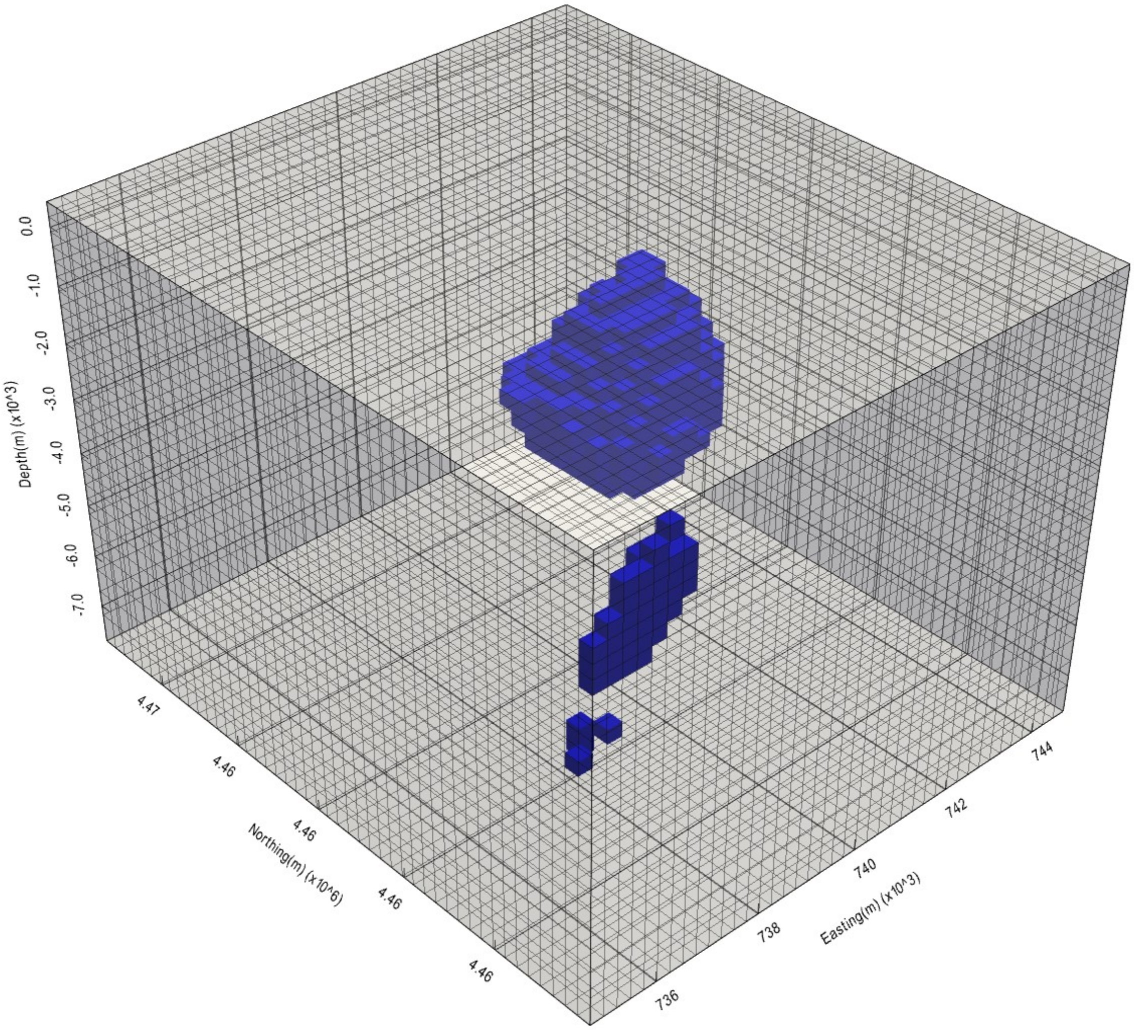

Figure 70: 3D view of unit 9

Unit 10

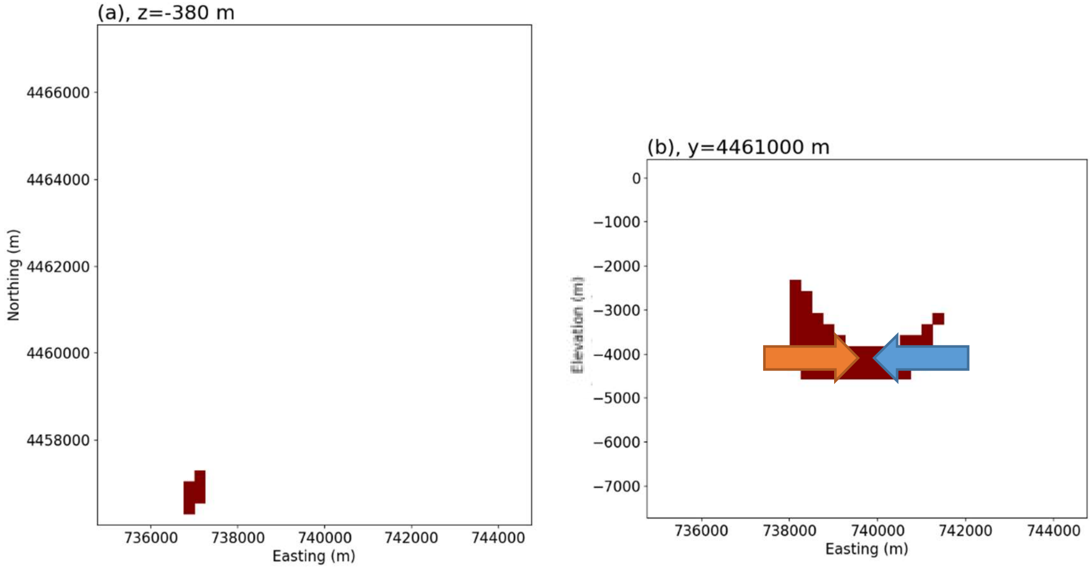

Figure 71: Cross-section view of unit 10. (a) is the horizontal cross-section obtained at elevation = -380 m while (b) is the vertical cross-section obtained at Northing = 4461000 m. Unit 10 is in red. The orange arrows indicate correlated features with the inverted density model while the blue arrows indicate correlated features with the inverted susceptibility model.

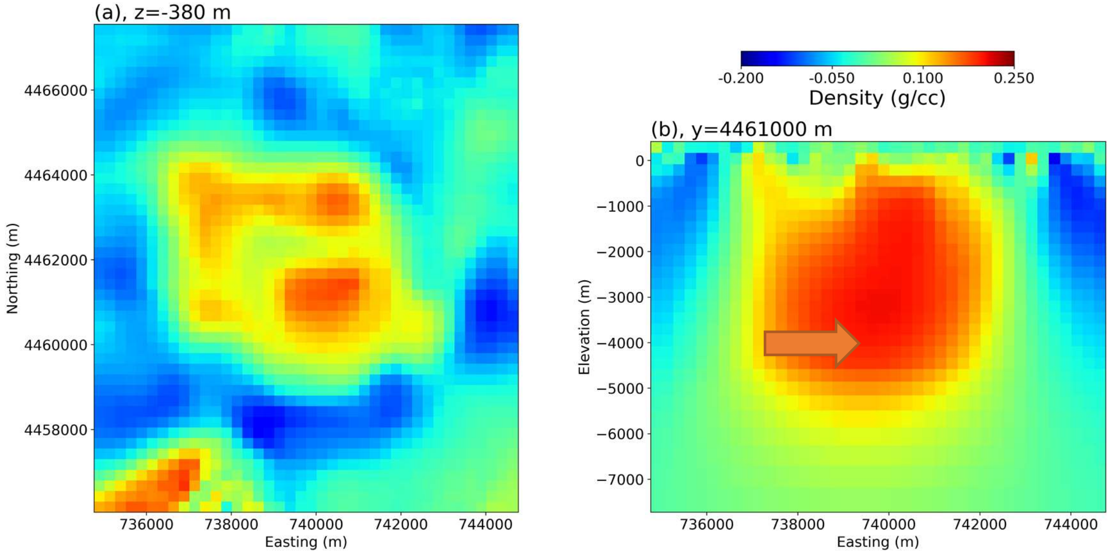

Figure 72: Jointly inverted density model. (a) is the horizontal cross-section obtained at elevation = -380 m while (b) is the vertical cross-section obtained at Northing = 4461000 m. The orange arrows indicate regions of positive densities associated with unit 10.

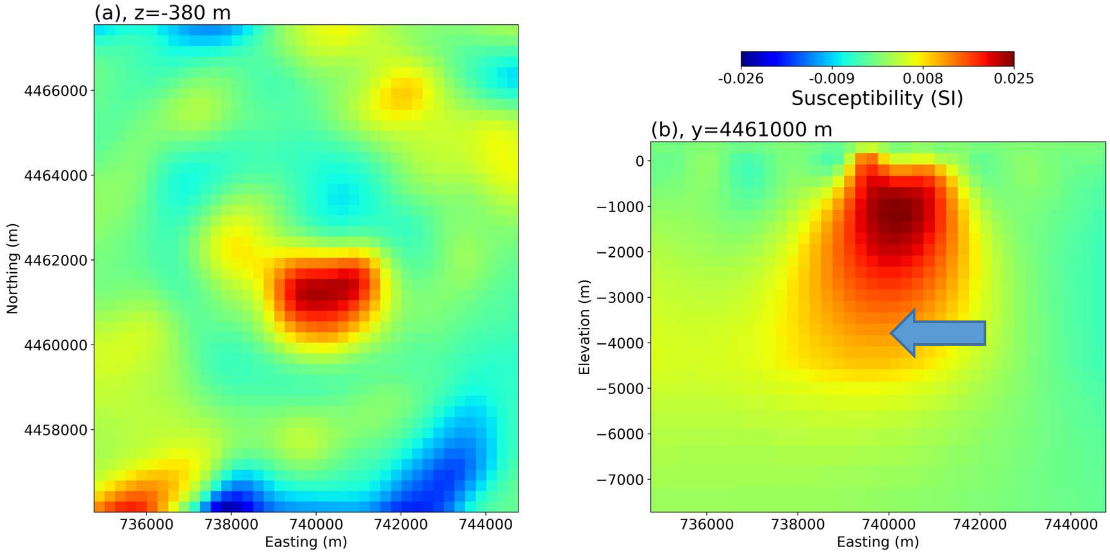

Figure 73: Jointly inverted susceptibility model. (a) is the horizontal cross-section obtained at elevation = -380 m while (b) is the vertical cross-section obtained at Northing = 4461000 m. The blue arrows indicate regions of positive susceptibilities associated with unit 10.

Unit 10 is another geologic unit located at the center of the ECC. It is classified based on high density contrast values and a dense clustering of values as seen in **Figure 37**. This unit on average contains lower magnetic susceptibility values than unit 9, but is characterized by positive magnetic susceptibilities. **Figure 38** shows that unit 10 underlies unit 9, and is encompassed by the undifferentiated carbonatites. Due to its location as a boundary unit separating unit 9 from the undifferentiated carbonatites, it is possible that unit 10 is an unidentified dense carbonatite or part of the many undifferentiated carbonatites within the ECCC. A large degree of uncertainty exists with this unit classification as no prior geological observations exist for this unit, and additional geophysics or petrophysics data are required to definitively differentiate this unit.

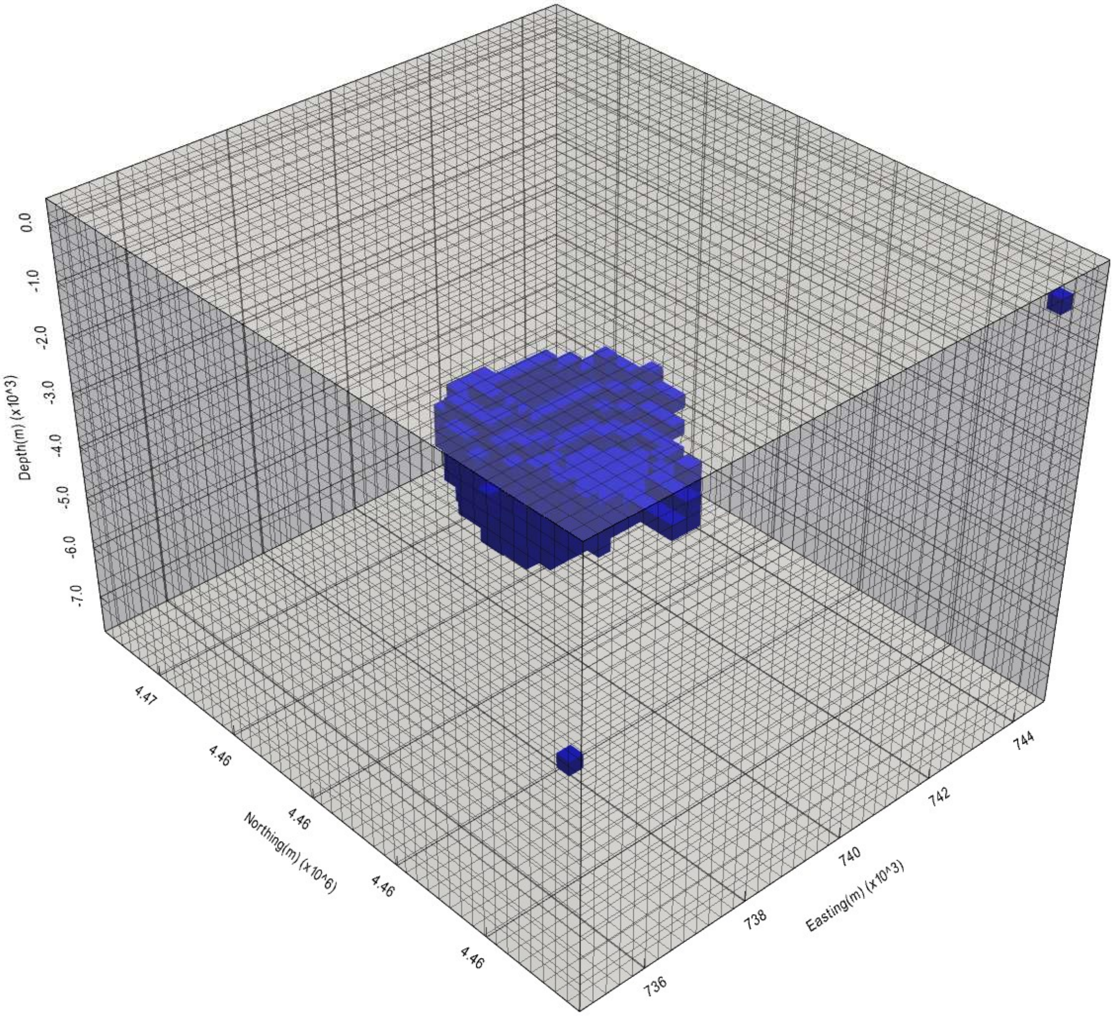

Figure 74: 3D view of unit 10

Unit 11

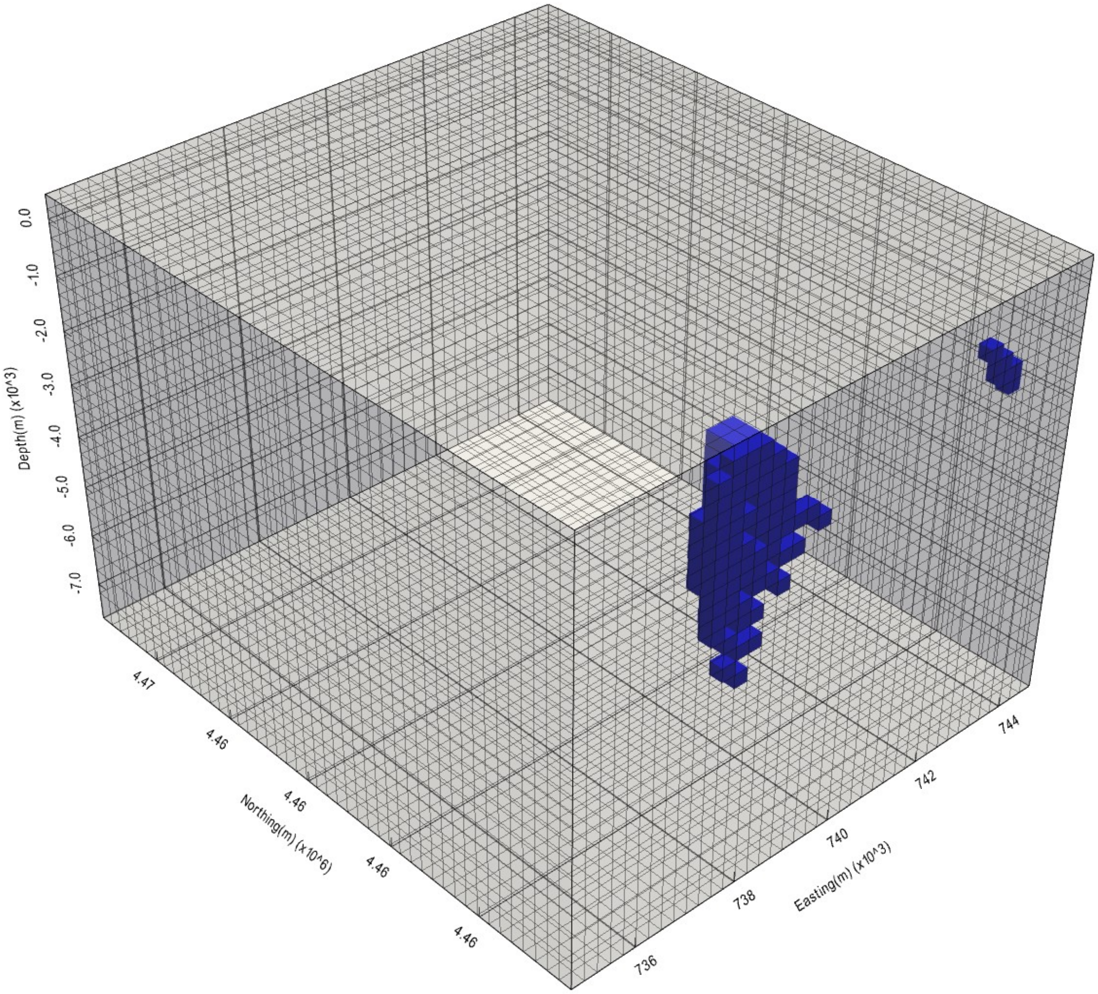

Figure 75: 3D view of unit 11

The crossplot grouping used to form unit 11 consists of a grouping of scattered values with high density but negative magnetic susceptibility as seen in **Figure 37**. Due to the dispersed nature of this unit, it is unclear as to whether this grouping was produced by non-random noise within the inversion or represents a real geologic unit. Some parts of this unit align with features that appear to have been created by the cross-gradient term during joint inversion. **Figure 75** depicts this unit only occurring at the lowest northing coordinates of the inverted model, and is fairly small in volume. If this unit does exist within the survey region, the strong remanence implied by the negative susceptibility values indicate that this unit is likely comprised of mafic or ultramafic rock.

Discussion

Originally, the only coupling term for joint inversion planned for this thesis was joint total variation, although the results of this study show the joint total variation coupling term is currently not recommended for the inversion of real datasets with a Gauss-Newton solution. Crestel (2017) implemented a primal-dual Newton method for JTV joint inversion, which may produce better results. JTV joint inversion was unsuccessful at inverting the Elk Creek data for a multitude of reasons. These included the JTV term not minimizing during joint inversion, negative impacts on the depth weighting of the recovered density model, and significant smoothing of the features present in the recovered density model. These results were unfortunate considering the optimistic results from synthetic studies into JTV joint inversion from previous studies including Haber & Gazit (2013) and Crestel (2017). One of the presumed benefits of the JTV coupling term with its ability to regularize inversion results turned out to be a major flaw with the method. The impact of the JTV term on the depth weighting of inverted models has not been noted in previous studies, and is an important lesson for future studies. The λ regularization parameter does not appear to be robust enough on its own to regularize the JTV term, and additional research into other methods of optimizing the JTV term is recommended. In its current state, results from the synthetic studies indicate that using the JTV joint inversion may be possible on small datasets, although regional studies on the scale of the Elk Creek data are currently infeasible. I believe this may be due to the size of the total variation term in large datasets, as larger datasets will include much larger variations between inverted models which the λ regularization parameter may not be able to handle.

A surprising find in this study is in regards to the second anomaly found in **Figure 44a** within the classified magnetite-dolomite carbonatite about 1,200m east of the niobium ore zone. The location of this anomaly coincides with the location of borehole EC-48, a drillhole reported by Molycorp workers to contain niobium pyrochlore with unique barium substitution in massive barite-dolomite carbonatite (Sherer, 1984). The presence of this unique form of pyrochlore mineralization creates two possibilities as to the identity of this second anomaly. The first is that the anomaly may be magnetite-dolomite carbonatite hosted beneath the previously explored barite-dolomite carbonatite. The second possibility is that the anomaly may be composed of barite-dolomite carbonatite with altered physical properties due to pyrochlore mineralization. Further study into this region is recommended, especially with the previous discovery of niobium mineralization within borehole logs.

Another surprise from this study was the classification of unit 9, which has the highest density and magnetic susceptibility at Elk Creek. Originally, the magnetite-dolomite carbonatite was expected to be the densest unit at Elk Creek based on results from Drenth (2014) and Kass et al. (2015). However, spatial testing of unit 9 during geology differentiation revealed it was far deeper in depth than the known magnetite-dolomite carbonatite and therefore any previously identified niobium, with unit 8 instead sharing similar spatial extents to the identified niobium ore zone. The volume of this unit is far larger than any previous prediction of magnetite-dolomite carbonatite from Drenth (2014) and SRK Consulting (2015), which is why the unit was conservatively not classified as magnetite-dolomite carbonatite. Portions of this unit may still be magnetite-dolomite carbonatite, as indicated by the alternate differentiations in **Figures 48** and **49**, as unit 8 and 9 do share coincident boundaries. Additional testing is highly recommended in order to determine the lithology of this large unit at the center of the Elk Creek carbonatite.

My study also revealed that the process of creating of a quasi-geology model is far more robust than previously expected, as a model of Elk Creek was created at the end of this study even in circumstances where much of the geology is hard to characterize. Unlike previous studies into geology differentiation such as Melo et al. (2017) which had well defined geologic units, multiple units in this study did not have relevant borehole data or other geological information. Despite these challenges, quantitative groupings of the geologic units based on physical property values and spatial correlations could still be successfully created. This is largely due to the application of joint inversion to the Elk Creek data, which produced crossplots which had better value clustering than crossplots produced by separate inversions. While there are significant uncertainties with some of the geologic units in the final quasi-geology model, the model can still serve as a guide for future studies into the deeper geology of the Elk Creek region.

Conclusion

The capabilities of the emerging procedure of geological differentiation in gleaning new insights from geophysical inversions was tested with this study on the Elk Creek carbonatite. Despite the challenging geology and lack of prior geological observations in many locations, I successfully managed to produce a quasi-geology model describing the geologic units within the ECCC. The creation of the quasi-geology model of Elk Creek was greatly benefited by the implementation of joint inversion. The cross-gradient coupling term for joint inversion produced inverted physical property models with better structural coupling than separate inversion. Additionally, the crossplots of the physical property values of the jointly inverted models showed much better clustering results of different lithologic units than in the separate inversion. This highlights the benefit of implementing joint inversion for geology differentiation, as the identification of clusters within the crossplot is extremely important.

This study also showed that even in regions of poorly defined geology, crossplot clustering from joint inversion and spatial analysis of the physical properties still allows for the classification of various geologic units. My work was able to recover the four lithologic groupings described in Kass et al. (2015), along with additional lithologic units which were not previously described, such as units 1-4 which were less dense than the undifferentiated carbonatites. However, some units which were originally expected to be differentiable were not characterized as individual units. This includes the lamprophyres, which could not be distinguished from the country/mafic rocks and the dolomite-carbonatite breccias which could not be distinguished from the other carbonatites.

An important discovery within this study was the identification of additional magnetite-dolomite carbonatite within the Elk Creek carbonatite. The classification of unit 8 within the quasi-geology model clearly identified the existing niobium ore zone (SRK Consulting, 2015) and also indicated the presence of an additional ore zone about 1,200 m to the east. A surprising result from this study was the identification of a large volume of high density and susceptibility contrast at the center of the ECCC. The similar properties of this volume to identified magnetite-dolomite carbonatite could indicate a much larger target zone than established in previous studies.

Bibliography

Bennington, N.L., Zhang, H., Thurber, C.H., Bedrosian, P.A., 2014, Joint inversion of seismic and magnetotelluric data in the Parkfield region of California using the normalized cross-gradient constraint.

Blakely R.J., 1996, Potential theory in gravity and magnetic applications, Cambridge University Press. Cambridge, UK.

Blessington, M. J., 2014, A niobium deposit hosted by a magnetite-dolomite carbonatite, Elk Creek Carbonatite Complex, Nebraska, USA.

Butler R.F., 1992, Paleomagnetism: magnetic domains to geologic terranes, Blackwell Scientific Publications.

Campbell, E., 2017, Sulfur isotope variations in the Elk Creek Carbonatite Complex, southeastern Nebraska, USA.

Carlson, M., and Treves, S., 2005, The Elk Creek Carbonatite, southeast Nebraska–an overview, *Natural Resources Research*, v. 14, p. 39-45.

Clark, D.A., 1999, Magnetic petrology of igneous intrusions: Implications for exploration and magnetic interpretation, *Exploration Geophysics*, v. 30, p. 5–26.

Cockett R., Kang S., Heagy L.J., Pidlisecky A., and Oldenburg D., 2015, SimPEG: An open source framework for simulation and gradient based parameter estimation in geophysical applications, *Computers & Geosciences*, v. 85(A), p. 142-154.

Colombo, D., and Stefano M. D., 2007, Geophysical modeling via simultaneous joint inversion of seismic, gravity, and electromagnetic data: Application to prestack depth imaging, *The Leading Edge*, v. (26), p. 326-331

Crestel B., 2017, Advanced techniques for multi-source, multi-parameter and multi-physics inverse problems.

Dampney, C.N.G, 1969, The equivalent source technique, *Geophysics*, v. 34(1), p. 39-53.

Drenth, B.J., 2014, Geophysical expression of a buried niobium and rare earth element deposit: The Elk Creek Carbonatite, Nebraska, USA, *Interpretation*, v. 2(4), p. SJ169-SJ179.

Exec. Order No. 13817, 82 Fed. Reg. 60835

Final list of critical minerals 2018, 2018, 83 Fed. Reg. 23295

Fregoso, E., Gallardo, L.A., 2009, Cross-gradients joint 3D inversion with applications to gravity and magnetic data, *Geophysics*, v. 74, p. L31-42

Foks, N.L., Krahenbuhl, R., and Li, Y., 2014, Adaptive sampling of potential-field data: A direct approach to compressive inversion, *Geophysics*, v. 79(1), p. IM1–IM9.

Fugro Airborne Surveys., 2011, Falcon™ airborne gravity gradiometer survey for Quantum Rare Earth Developments Corp. processing report.

Gallardo, L.A., and Meju, M.A., 2003, Characterization of heterogeneous near-surface materials by joint 2D inversion of DC resistivity and seismic data, *Geophysical Research Letters*, v. 30(13), p. 1658–1664.

Gallardo, L.A., and Meju, M.A., 2007, Joint two-dimensional cross-gradient imaging of magnetotelluric and seismic traveltime data for structural and lithological classification, *Geophys. J. Int.*, v. 169(3)

Gallardo, L.A., and Meju, M.A., 2011, Structure-coupled multiphysics imaging in geophysical sciences, *Rev. Geophys.*, v. 49

Gardner, G.H.F., Gardner L.W., and Gregory, A.R., 1974, Formation velocity and density -- the diagnostic basics for stratigraphic traps. *Geophysics*, v.39, p. 770–780.

Grant, F.S., and West, G.E., 1965, Interpretation theory in applied geophysics. McGraw-Hill, New York.

Habashy, T.M., and Abubakar, A., 2004, A general framework for constraint minimization for the inversion of electromagnetic measurements, *Prog. Electromagn. Res.*

Haber, E., and Oldenburg, D., 1997, Joint inversion a structural approach, *Inverse Prob*., v. 13, p. 63–67.

Haber, E., and Gazit M.H., 2013, Model fusion and joint inversion, *Surv Geophys*, v. 34, p. 675-695.

Heiland, C.A., 1968, Geophysical exploration, Hafner Publishing Co., New York.

Hinze, W.J., Von Frese, R.R.B., and Saad, A.H., 2013, Gravity and magnetic exploration, Cambridge University Press. Cambridge, UK.

Hinze, W.J., and Chandler, V.W., 2020, Reviewing the configuration and extent of the Midcontinental rift system, *Precambrian Research*, v. 342

Kass, M.A., Drenth, B.J., Foks L., and Capriotti J., 2015, Quantitative geophysical interpretation of gravity gradient and magnetic data over a buried carbonatite: The Elk Creek deposit, Nebraska, USA.

Kim, J.D., Jiajia, S., Melo, A.T., Khan, S.D., 2020, Regional scale mineralization exploration through joint inversion and geology differentiation based on muti-physics geoscientific data.

Li, Y., and Krahenbuhl, R., (2015). Gravity and magnetic methods in mineral and oil & gas exploration and production. European Association of Geoscientists & Engineers (EAGE). p. 10-18.

Li, Y., Melo A., Martinez, C., and Sun, J., 2019, Geology differentiation: A new frontier in quantitative geophysical interpretation in mineral exploration, *The Leading Edge*, v. 38(1), p. 60-66.

Li, Y., Oldenburg D.W., 1996, 3-D inversion of magnetic data, *Geophysics*, v. 61(2), p. 394-408.

Li, Y., Oldenburg D.W., 1998, Separation of regional and residual magnetic field data, *Geophysics*, v. 63(2), p. 431-439.

Li, Y., Oldenburg D.W., 2000, Joint inversion of surface and three-component borehole magnetic data, *Geophysics*, v. 65(2), p. 540-552.

Martinez, C., and Y. Li, 2015, Lithologic characterization using airborne gravity gradient and aeromagnetic data for mineral exploration: a case study in the Quadrilátero Ferrífero, Brazil, *Interpretation*, v.3(2), p. SL1–SL13.

Melo, A. T., Sun, J., and Li, Y., 2017, Geophysical inversions applied to 3D geology characterization of an iron oxide copper-gold deposit in Brazil, *Geophysics*, v.82(5), p. K1–K13

Menke, W., 1984, Geophysical data analysis: Discrete inverse theory, Elsevier.

Mickus, K. L., and Hinojosa, J. H., 2001, The complete gravity gradient tensor derived from the vertical component of gravity: A Fourier transform technique, *Journal of Applied Geophysics*, v. 46(3), p. 159-174.

Mitchell, R. 2014, Primary and secondary niobium mineral deposits associated with carbonatites, *Ore Geology Reviews*, v. 64, p. 626-641.

Moorkamp, M., Jones, A., Fishwick, S., 2010, Joint inversion of receiver functions, surface wave dispersion, and magnetotelluric data, *J. Geophys. Res. Solid Earth,* v. 115

Moorkamp, M., Lelièvre P.G., Linde N., and Khan A., 2016. Integrated imaging of the Earth: Theory and applications, Hoboken, NJ, John Wiley.

Ojakangas, R., Morey, G., and Green, J., 2001, The Mesoproterozoic midcontinent rift system, Lake Superior region, USA, *Sedimentary Geology*, v. 141, p. 421-442.

Oldenburg D., and Li Y., 2005, Inversion for applied geophysics: A tutorial, *Near-Surface Geophysics.*

Paoletti, V., Fedi, M., Italiano, F., Florio, G., and Ialongo, S., 2016, Inversion of gravity gradient tensor data: does it provide better resolution?, *Geophysical Journal International*, v. 205(1), p. 192–202.

Papp, J.F., 2013, Niobium (columbium): U.S. Geological Survey mineral commodity summaries 2013, p. 110–111.

Pilkington, M., 2014, Analysis of gravity gradiometry inverse problems using optimal design measures, *Geophysics*, v. 77(2), p. G25-G31.

Rudin, L., Osher, S., and Fatemi, E., 1992, Nonlinear total variation based noise removal algorithms, *Physica D.*, v. 60(1-4), p. 259–268.

Schulz, K.J., Piatak, N.M., and Papp, J.F., 2017, Niobium and tantalum, chap. M *of* Schulz, K.J., DeYoung, J.H., Jr., Seal, R.R., II, and Bradley, D.C., eds., Critical mineral resources of the United States—economic and environmental geology and prospects for future supply: U.S. Geological Survey Professional Paper 1802, p. M1–M34.

Sherer, R.L., 1984, Geology of Drill Hole EC-48, Elk Creek, Nebraska, Molycorp Internal Report.

Shi, Z., Hobbs, R.W., Moorkamp, M., Tian, G., Jiang, L., 2017, 3-D cross-gradient joint inversion of seismic refraction and DC resistivity data, *Journal of Applied Geophysics*, v. 141, p. 54-67

Sims, P., and Petermar, Z., 1986, Early Proterozoic Central Plains orogen: a major buried structure in the north-central United States, *Geology*, v. 14, p. 488-491.

SRK Consulting, 2015, NI 43-101 Technical report updated mineral resource estimate Elk Creek Niobium Project Nebraska.

Sullivan, C. B., and Kaszynski A. A., 2019, PyVista: 3D plotting and mesh analysis through a streamlined interface for the Visualization Toolkit (VTK), *Journal of Open Source Software*, v. 4(37), p. 1450.

Telford, W.M., Geldart, L.P. and Sheriff, R.E., 1990, Applied geophysics, 2nd Edition, Cambridge University Press, Cambridge, UK.

Tetra Tech, 2012. Report to: Quantum Rare Earth Developments Corp, Elk Creek Nb Project, Nebraska, US, resource estimate update, document no. 1291370100-REP-R0001-02.

Tikhonov, A. N., and Arsenin, V.Y., 1977, Solutions of ill posed problems, W. H. Winston and Sons.

Torsvik, T.H., Van der Voo, R., Preeden, U., Niocaill, C.M., Steinberger, B., Doubrovine, P.V., van Hinsbergen, D.J.J., Domeier M., Gaina, C., Tohver, E., Meert, J.G., McCausland, P.J.A., Cocks, L.R.M., 2012, Phanerozoic polar wander, paleography and dynamics, *Earth-Science Reviews*, v. 144, p. 325-368

USGS: U.S. Geological Survey. 2020, Niobium (columbium) and tantalum statistics and information.

https://pubs.usgs.gov/periodicals/mcs2020/mcs2020-niobium.pdf, accessed December 2020.

Xu, A., 1996, Mineralogy, petrology, geochemistry and origin of the Elk Creek carbonatite, Nebraska.

Zhdanov, M.S., 2002, Geophysical inverse theory and regularization problems, Elsevier.

Zhdanov, M.S., Ellis, R., Mukherjee, S., 2004, Three-dimensional regularized focusing inversion of gravity gradient tensor component data, *Geophysics*, v. 69(4), p. 925–937.

Zhadanov, M.S., 2012, Gribenko, A., Wilson, G., 2012, Generalized joint inversion of multimodal geophysical data using Gramian constraints: Three-dimensional joint inversion. *Geophysical Research Letters,* v.39(9)